DOT/FAA/TC-16/27

Federal Aviation Administration
William J. Hughes Technical Center
Aviation Research Division
Atlantic City International Airport
New Jersey 08405

Nonlinear Imaging for Enhanced Ultrasonic Assessment of Diffusion-Bonded Engine Components

May 2017

Final Report

U.S. Department of Transportation
Federal Aviation Administration

NOTICE

Technical Report Documentation Page

1. Report No.	2. Government Accession No.	3. Recipient's Catalog No.
DOT/FAA/TC-16/27		

4. Title and Subtitle	5. Report Date
NONLINEAR IMAGING FOR ENHANCED ULTRASONIC ASSESSMENT OF DIFFUSION-BONDED ENGINE COMPONENTS	May 2017
	6. Performing Organization Code

7. Author(s)	8. Performing Organization Report No.
Peter B. Nagy,[1] Ziyin Zhang,[1] Waled T. Hassan[2]	

9. Performing Organization Name and Address	10. Work Unit No. (TRAIS)
[1]University of Cincinnati 2600 Clifton Avenue Cincinnati, OH 45220 [2]Rolls-Royce Corporation 546 South Meridian Street Indianapolis, IN 46225	11. Contract or Grant No.

12. Sponsoring Agency Name and Address	13. Type of Report and Period Covered
Federal Aviation Administration Engine and Propeller Directorate 12 New England Executive Park Burlington, MA 01803	Final Report
	14. Sponsoring Agency Code ANE-111

15. Supplementary Notes

The FAA William J. Hughes Technical Center Aviation Research Division CORs were Dave Galella and Cu Nguyen (retired).

16. Abstract

Ultrasonic non-collinear shear wave mixing has the potential for assessing otherwise hidden imperfections in diffusion-bonded engine components. Generally, both bulk nonlinearity from the neighboring host and interface nonlinearity contribute to the measured signal. Analytical, numerical, and experimental efforts showed that interface imperfections produce the same level of nonlinearity in both reflection and transmission modes, but reflection measurements are more selective to interface imperfections than transmission ones. In this study, an integrated nonlinear inspection system was designed, built, and validated by a series of tests. With hardware and software improvements, increased ultrasonic power, and implementation of a novel four-way polarity flipping technique, the signal-to-noise ratio of the nonlinear inspection system was significantly increased. The new system is capable of detecting nonlinear reflection from Ti-6Al-4V and IN718 diffusion bonds. The obtained results show that, in high-quality diffusion bonds, reflection measurements with coherent averaging are the most suitable option for bond quality assessment. The upgraded nonlinear inspection system is sufficiently robust and compact for future use by engine manufacturers in feasibility studies aimed at better quality assurance, strength assessment, and service-life prediction.

17. Key Words	18. Distribution Statement
Nondestructive evaluation, Nonlinear ultrasonics, Interface imperfection, Engine alloys, Diffusion bonding, Cross-boundary grain growth	This document is available to the U.S. public through the National Technical Information Service (NTIS), Springfield, Virginia 22161. This document is also available from the Federal Aviation Administration William J. Hughes Technical Center at actlibrary.tc.faa.gov.

19. Security Classif. (of this report)	20. Security Classif. (of this page)	21. No. of Pages	22. Price
Unclassified	Unclassified	78	

ACKNOWLEDGEMENTS

This work was supported by the FAA under contract DTFACT-13-C-0024. High-quality diffusion-bonded Ti-6Al-4V and IN718 specimens were provided by Vacuum Process Engineering, Inc. Machining and metallurgical characterization services were provided by Metcut Research, Inc. The authors would like to express their appreciation to Senior Research Associate Curtis Fox of the University of Cincinnati for his invaluable contributions to hardware and software development.

TABLE OF CONTENTS

LIST OF FIGURES

LIST OF TABLES

LIST OF ACRONYMS

ADC	Analog-to-digital converter
AFG	Arbitrary function generator
BPF	Band pass filter
CBGG	Cross-boundary grain growth
CS	Crushing strain
DAC	Digital-to-analog converter
DOF	Degree of freedom
FE	Finite element
FFT	Fast Fourier transform
GPIB	General Purpose Interface Bus
NDE	Nondestructive evaluation
PCI	Peripheral component interconnect
RRC	Rolls-Royce Corp
SNR	Signal-to-noise ratio
VPE	Vacuum Process Engineering, Inc.

EXECUTIVE SUMMARY

The primary objectives of this project were:

1. To study the unique capabilities of nonlinear ultrasonic C-scan imaging relative to conventional linear ultrasonics operating at similar depth and lateral resolutions.
2. To further develop these capabilities for the detection of hidden interface imperfections in diffusion-bonded titanium and nickel alloy components.
3. To develop a novel nonlinear inspection system and integrate it into a compact computer-controlled nondestructive evaluation (NDE) tool that will be available for engine manufacturers in future feasibility studies.
4. To test and validate the enhanced capabilities of the new nonlinear inspection system on a representative set of controlled diffusion-bonded engine alloy specimens provided by the industrial partner Rolls-Royce Corp®.

To address these objectives, the project was divided into two main parts:

1. Nonlinear ultrasonic C-scan imaging system development:

    a. Task 1.1–Nonlinear imaging system design
    b. Task 1.2–Software development and testing
    c. Task 1.3–Hardware development and testing
    d. Task 1.4–System validation

2. Diffusion-bond inspection:

    a. Task 2.1–Destructive testing of Ti-6Al-4V and IN718 diffusion-bonded specimens
    b. Task 2.2–Nondestructive testing of the same specimens using the upgraded nonlinear inspection system
    c. Task 2.3–Data analysis and evaluation

Part 1 of the project was aimed at system development. Task 1.1 laid the foundations for optimal system design. In this effort, the nonlinear interaction of shear incident waves with imperfect interfaces was studied by analytical and numerical means. The results showed that imperfect interfaces generated the same amount of nonlinearity in the reflection and transmission fields. Detecting the weaker nonlinear reflection from the interface was shown to be a better option for assessing bond quality than the stronger transmitted nonlinear reflection because reflection measurements efficiently suppress the spurious bulk nonlinearity of the surrounding host material.

Tasks 1.2 and 1.3 focused on developing the software and hardware components, respectively, of the new nonlinear inspection system. The operation of the new NDE system is based on non-collinear shear wave missing and it is capable of measuring both the transmitted and reflected nonlinear signatures of imperfect interfaces. Despite its considerable complexity, the new integrated inspection system is relatively compact and robust. Most importantly, it offers significantly improved signal-to-noise ratio and lateral resolution and can be used for

backreflection/backscattering measurements in true one-sided mode of operation. Task 1.4 completed Part 1 by testing and validating the developed measurement procedure, including automated transducer alignment, data acquisition, signal conditioning, image processing, and feature extraction.

Part 2 of the project was aimed at performing destructive testing on Ti-6Al-4V and IN718 diffusion-bonded specimens. Task 2.1 used destructive metallurgic examination to characterize two batches of diffusion-bonded Ti-6Al-4V specimens. The first batch consisted of nine low- to medium-quality bonds with cross-boundary grain growth (CBGG) levels between 6.6% and 86%. The second batch consisted of six high-quality specimens of essentially perfect 100% CBGG. Metallurgical evaluation of eight diffusion-bonded IN718 specimens revealed that, with one notable exception, all of them experienced severe grain growth during bonding and became unsuitable for both linear and nonlinear ultrasonic inspection. Because no alternative processing method could be identified for producing high-quality diffusion bonds in IN718 engine alloy before the end of this project, validation of the nonlinear ultrasonic inspection method on nickel-based superalloys will have to be performed in a follow-up study.

In Task 2.2, nonlinear reflection C-scan images of Ti-6Al-4V diffusion-bonded specimens and one IN718 diffusion-bonded specimen were obtained using the new nonlinear inspection system. In Task 2.3, the collected data were analyzed and both coherent and incoherent averaging methods were tested to optimize the quantitative assessment of diffusion-bonded interfaces. The results revealed that, for specimens with medium to high bond qualities of approximately 70%, CBGG incoherent averaging was sufficient to distinguish between different bond qualities, whereas for specimens with very high bond qualities of approximately 100%, CBGG coherent averaging that helps suppress the nonlinear grain noise from the host material appears to be a better option for bond characterization.

Neither linear nor nonlinear inspection alone is entirely sufficient to cover the wide range of diffusion-bond quality encountered in engine components; therefore, the developed system is capable of working in both inspection modes. In general, the nonlinearity of the interface imperfection reaches a peak during the transition from poorly bonded specimens to perfectly bonded specimens, which can be exploited to significantly extend the range of conventional linear ultrasonic inspection techniques. The developed nonlinear inspection system is sufficiently robust and compact for future use by engine manufacturers in feasibility studies aimed at better quality assurance, strength assessment, and service-life prediction.

1. INTRODUCTION

Diffusion bonding is a solid-state welding method capable of joining similar and dissimilar metals while ensuring that the joint exhibits sufficiently high strength and temperature stability. It has significant advantages over other welding methods because it introduces very little plastic deformation and residual stress in the material, and there is essentially no contamination from the bonding process. Therefore, diffusion bonding is widely used in the aerospace industry to deal with joining problems that are difficult or impossible to solve by other welding methods. However, subtle imperfections in diffusion bonds that might remain hidden from conventional nondestructive evaluation (NDE) methods can greatly reduce the service life of fracture-critical components. Numerous studies have investigated the physical characteristics of imperfect interfaces [1–5]. In particular, Ohsumi et al. showed that less than a 5%–10% lack of bond in diffusion-bonded Ti-6Al-4V engine components can result in dramatic reduction in some of the dynamic strength-related properties, especially in crack resistance and impact damage tolerance [1]. Partially bonded imperfect interfaces behave much like tight kissing bonds. Though a poorly bonded interface can be detected by conventional linear ultrasonic inspection methods, a better diffusion-bonded interface behaves more like a tight kissing bond, which exhibits very low linear ultrasonic contrast (i.e., low reflection and high transmission) [6]. When assessing diffusion bonds between dissimilar metals, linear ultrasonic inspection has an inherently limited detection threshold because of the acoustic impedance mismatch between the two materials, and weak imperfections might remain hidden below this threshold. Even when detecting the bond between similar metals, strong incoherent scattering from the microstructure of the host material can hide weak interface imperfections. As a result, the sensitivity of linear ultrasonic inspection methods quickly drops as bond quality increases, and it becomes impossible to distinguish various bond qualities exhibiting significantly different strength parameters [7–9].

Previous studies have shown that an unbonded interface cannot support tension and, therefore, opens up during the tensile phase of acoustic vibration. Periodic opening and closing of the interface distorts the impinging harmonic acoustic wave and, therefore, becomes the source of nonlinearity. This specific characteristic of a partially closed imperfect interface provides a unique opportunity for assessing bond quality by detecting the acoustic nonlinearity it generates during ultrasonic inspection [10–14]. Among all the nonlinear ultrasonic NDE techniques, one method, namely the nonlinear shear wave mixing technique, is promising in detecting the excess nonlinearity caused by a diffusion-bonded interface. This method mixes two shear waves at the interface and, under certain conditions, a third longitudinal wave is generated with frequency and wave vector equal to the sum of those of the two primary shear waves [15–18]. By analyzing the strength of the mixed longitudinal wave, the excess nonlinearity of the interface can be characterized. When using this technique to produce nonlinear C-scan images of the inspected specimens, the two transmitting transducers can be arranged on top of the specimen and the receiving transducer can be placed beneath the specimen to detect the transmitted nonlinear signal. Another arrangement, which is more suitable for scanning purposes, is placing the receiving transducer on the same side of the specimen with the two transmitting transducers and detecting the back-wall reflection of the generated nonlinear signal. Preliminary results based on this non-collinear shear wave mixing technique showed that when compared to conventional linear inspection, which is capable of detecting only gross bond imperfections, nonlinear inspection can characterize even the highest level of bond quality in the transition region from

medium to the best. Neither linear nor nonlinear inspection alone is capable of distinguishing diffusion-bond qualities over the whole range of importance in NDE. However, by combining the two techniques, inspection can be expanded over a wider range of bond quality.

Shear wave mixing was first introduced to assess the intrinsic bulk nonlinearity of materials [15–18]. In the case of nonlinear interface characterization, the mixing volume will include not only the diffusion-bonded interface but also some of the surrounding material. In this case, both the bulk nonlinearity of the host material and the excess nonlinearity generated by the imperfect interface will contribute to the transmitted nonlinear signature. The relatively strong bulk nonlinearity of the host material is the baseline nonlinearity that represents a detection threshold for interface nonlinearity measurements. A high baseline level adversely affects the nonlinear contrast produced by interface imperfections. One way to suppress the bulk nonlinearity of the host material is to increase the incident angles of the two interacting shear waves so that the mixing volume will include less of the surrounding material but more of the interface. Increasing the incident angles also helps to move the inspection system away from the optimal bulk angular condition (the "resonance" condition) and thereby reduces the measured spurious bulk nonlinearity. The results show that decreasing the two incident angles can help reduce the bulk nonlinearity by approximately 3 dB [8], but it is still insufficient for some applications. In addition, there is a practical limit for how much these angles can be increased or decreased. In an immersion inspection system built for scanning purposes, all the transducers and the specimen are submerged in water. There are cutoff angles for efficient transmission of shear wave energy into the specimen that presents the lower and upper limits for the incident angles. The angles have to be above the longitudinal critical angle to ensure that there are only shear waves in the specimen.

This study's numerical study on imperfect interfaces showed that there is another approach to maximize the contribution of interface imperfections to the measured nonlinear signature. Both analytical approximations and computational simulations indicated that an imperfect interface generates the same amount of nonlinearity in both the reflected and transmitted ultrasonic fields [19]. Considering cases only when the diffusion bond is invisible to linear inspection, which means that there is no significant linear contrast from the interface, the bulk nonlinear signal of the material always propagates in the forward transmission direction. Therefore, directly detecting the nonlinear reflected signal from the interface instead of relying on the transmitted signal being reflected from the back wall completely eliminates, in theory, the adverse influence of bulk material nonlinearity, thereby increasing the sensitivity for different bond imperfections. However, performing reflection measurements requires a much more sensitive experimental system with an extremely high signal-to-noise ratio (SNR). In the first version of this study's nonlinear inspection system, narrow-band filters were used to separate the mixed nonlinear signal from the spurious second harmonic signals, and band pass filtering inherently increased the temporal width of the mixed signal. Because the time interval between the reflected signal and the first back-wall reflection of the transmitted signal can be very short, the two signals might overlap with each other, and it becomes difficult to resolve the sought reflected nonlinear signal.

2. IMAGING SYSTEM DESIGN

In this study, an advanced non-collinear shear-wave-mixing ultrasonic inspection system was

developed for detecting nonlinear reflection from diffusion-bonded interfaces. This effort involved both software and hardware development. The various mechanical, electric, and software components were integrated into a compact inspection system controlled by a single computer. The new nonlinear inspection system was designed specifically to increase the detection sensitivity to hidden interface imperfections between diffusion-bonded engine alloy components. To achieve this goal, a significant effort was devoted to analytical investigations and computational simulations aimed at improving the operational parameters of the new system. These efforts helped us further understand various aspects of the non-collinear shear wave mixing technique and exploit its potential in detecting hidden interface imperfections. Initial experiments conducted on diffusion-bonded Ti-6Al-4V specimens were aimed at validating this study's assumption that non-collinear shear wave mixing offers a unique potential for detecting hidden interface imperfections. In this section, analytical and numerical results are presented first to justify the choices made for this study in the optimization during the subsequent design phase of the project. The optimized design of the new imaging system capable of detecting hidden interface imperfections in diffusion-bonded specimens is then presented.

2.1 COMSOL FINITE ELEMENT SIMULATIONS FOR OPTIMIZED INTERFACE CHARACTERIZATION

One of the main goals of this project was to suppress the bulk nonlinearity detected by the non-collinear shear wave mixing technique to increase the detection sensitivity to interface imperfections. To achieve this goal, the mechanism of nonlinear shear wave mixing was further investigated. The host material can be modeled as an isotropic hyperelastic solid, and its quadratic nonlinearity can be characterized by its third-order elastic moduli. The third-order elastic moduli can be expressed by using either the method suggested by Landau and Lifshitz [20] or the method introduced by Murnaghan [21]. In this study, it was more convenient to use the Murnaghan coefficients to define the nonlinearity of the material because the COMSOL Multiphysics® software that was used to conduct the numerical simulations already has a built-in option that uses the Murnaghan coefficients to define the nonlinearity of a hyperelastic material. Because the study was focused on engine alloys such as Ti-6Al-4V, it was crucial to establish the three Murnaghan coefficients for this material. Based on the paper by Man et al. [22], the Murnaghan coefficients of Ti-6Al-4V were calculated as $l = 53$ GPa, $m = -113$ GPa, and $n = 54$ GPa; these coefficients were used throughout this study's numerical simulations. In bulk nonlinear materials characterization, the bulk resonance conditions:

$$\cos\varphi = c^2 - \frac{(1-c^2)(1+a^2)}{2a} \tag{1a}$$

and

$$\omega_1 \sin\theta_1 = \omega_2 \sin\theta_2 \tag{1b}$$

have to be satisfied to maximize the amplitude of the mixed longitudinal wave [15–18]. Here, the angle $\varphi = \theta_1 + \theta_2$ is the interaction angle between the two shear waves, $a = \omega_2 / \omega_1$ denotes the frequency ratio between the two interacting shear waves, and $c = c_s / c_d$ denotes the shear-to-longitudinal velocity ratio in the material. A schematic illustration of the numerical simulation model for bulk mixing is shown in figure 1. T_1 and T_2 are the two transducers for

transmitting the primary shear waves, and T_3 is the transducer for receiving the generated longitudinal wave. All three transducers have the same 3-mm width, and the distances between the center of the interaction zone and the transducers are set at 5 mm so that the two shear waves reach the center at the same time. The frequencies of the two shear waves are f_1 = 4.5 MHz and f_2 = 5.5 MHz. The number of cycles in the Hanning windowed tone burst are N_1 = 6 and N_2 = 7, respectively, to ensure that the two pulses are approximately the same length. The displacement amplitudes for the two shear waves are selected as $U_1 = U_2$ =1 nm. All the boundaries of the model, except for the bottom one, are covered with absorbing boundaries in the simulation to prevent spurious interference caused by reflected shear waves. The bottom boundary is of "longitudinal wave absorption" type to avoid the need for reflection correction of the measured displacement amplitude of the longitudinal wave. To prevent diffracted components of the primary shear waves from interfering with the much weaker nonlinear signals, the simulation was run twice by flipping the polarities of the excitation signals and averaging the two received signals. This technique efficiently suppresses the fundamental harmonics that will otherwise completely overshadow the sought mixed signals of nonlinear origin. The material parameters used in the following simulations are listed in table 1.

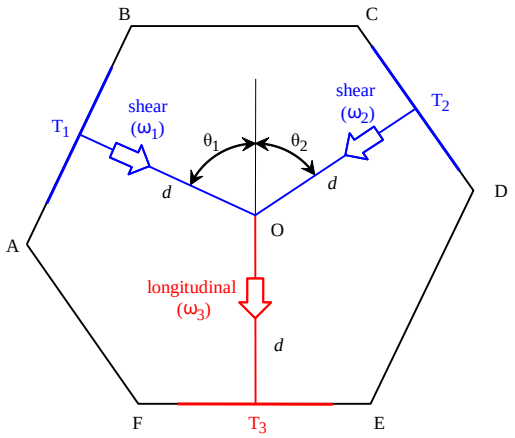

Figure 1. Schematic illustration for bulk mixing

Table 1. Material parameters used in the bulk mixing model

	ρ	λ	μ	*l*	*m*	*n*
	[kg/m^3]	[GPa]	[GPa]	[GPa]	[GPa]	[GPa]
Ti-6Al-4V	4456	81.72	45.89	53	-113	54

Figure 2(a) shows a typical simulated bulk nonlinear signal. The frequency of this signal is exactly 10 MHz. To find how the three Murnaghan coefficients affect the amplitude of the nonlinear longitudinal signal, parametric studies were run by changing each Murnaghan coefficient. The results showed that the amplitude of the nonlinear signal is linearly dependent only on the second Murnaghan coefficient, *m*, as shown in figure 2(b). This finding is also consistent with the analytical theory of shear wave mixing [15–18]. Escobar-Ruiz et al. showed that misaligning the inspection system from the bulk resonance condition helped suppress the

bulk nonlinearity [8]. As long as the angular condition in equation 1b is satisfied to ensure that the generated nonlinear signal is normal to the receiving transducer, misaligning the angles makes the periodicity of the interference pattern produced by the two shear waves deviate from the wavelength of the longitudinal wave and, therefore, helps reduce the bulk nonlinearity.

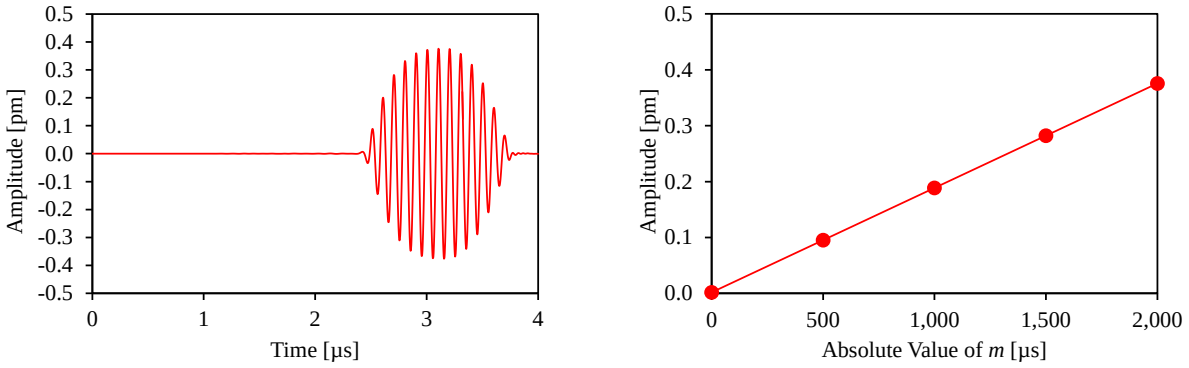

(a) (b)

Figure 2. The (a) typical simulated bulk nonlinear signal generated in Ti-6Al-4V with f_1 = 4.5 MHz, f_2 = 5.5 MHz and m = -2000 GPa and (b) relationship between the Murnaghan coefficient, m, and the amplitude of the bulk nonlinear signal

To find how much the bulk nonlinearity can be suppressed by misaligning the two shear wave transducers, another parametric study was run by changing the incident angle of the shear wave of lower frequency, whereas that of the other transmitter was chosen according to equation 1b. A simple geometric approximation was developed for estimating the bulking mixing efficiency [19]. Without detailed algebraic derivation, in the 2-D case considered here, the geometrical mixing efficiency η can be expressed as:

$$\eta = \frac{\sum_{i}^{3} A_i\, b_i\, \mathrm{sinc}^2\left[\frac{\pi b_i}{2}\left(\frac{1}{\lambda_d} - \frac{1}{\Lambda}\right)\right]}{\sum_{i}^{3} A_i\, b_i} \tag{2}$$

Here, A_i and b_i represent the widths and lengths of the three distinct parts of the interaction area in the 2-D case, and Λ denotes the periodicity of the interference pattern that is determined by the frequencies and incident angles of the two incident shear waves.

The numerical results shown in figure 3 are in agreement with the analytical approximation. Figure 3 also shows that misaligning the incident angles from the bulk resonance condition can help suppress the bulk nonlinearity by up to 20 dB. However, this technique has its own limitations. Nonlinear ultrasonic inspection based on non-collinear shear wave mixing is usually conducted with obliquely incident longitudinal transducers in either immersion or contact mode of operation. Unfortunately, lowering the incident angles of the interacting shear waves is limited by the requirement that the compressional waves generated by the transmitters hit the surface at incident angles above the first (longitudinal) critical angle in the coupling medium (water or

polymer wedge). In Ti-6Al-4V, this condition sets a limit of $\theta_{2m} = \sin^{-1}(c_s/c_d) \approx 31°$ on the smaller of the shear wave angles and $\theta_{1m} = \sin^{-1}(a\,c_s/c_d) \approx 39°$ on the larger one. In immersion inspection, the two refraction angles must be chosen above $\theta_1 \approx 54°$ and $\theta_2 \approx 42°$ to retain sufficiently high energy transmission into the specimen to be tested [8]. Though figure 3 shows that theoretically misaligning the angles can help suppress the bulk nonlinearity, this study's experiments showed that this technique can only suppress the bulk nonlinearity by approximately 6 dB.

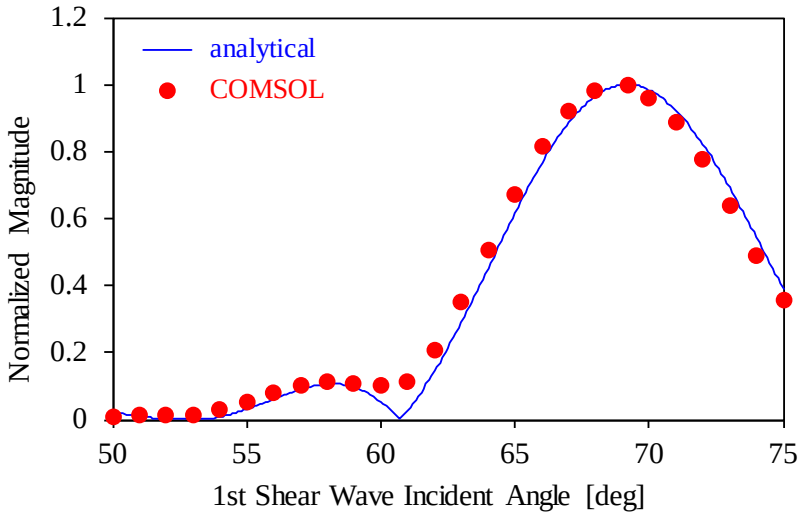

Figure 3. Comparison between analytical approximation and numerical results on the bulk mixing efficiency in Ti-6Al-4V

In an effort to further reduce the adverse influence of bulk nonlinearity in the host material and, therefore, increase the contrast for the imperfect interface between two diffusion-bonded solids, a combined analytical and computational investigation was conducted to identify the optimal inspection conditions for ultrasonic characterization of imperfect interfaces based on non-collinear shear wave mixing (see appendix A). Two analytical models were developed for nonlinear imperfect interfaces. The first model uses a finite nonlinear interfacial stiffness representation of an imperfect interface of vanishing thickness, whereas the second model relies on a thin nonlinear interphase layer to represent an imperfect interface region. Both models were numerically verified by comparison to COMSOL finite element (FE) simulations, and the study of the two models suggests another way of suppressing the spurious bulk nonlinearity. In the absence of linear reflection at the interface and incoherent nonlinear backscattering from the inhomogeneous microstructure of the neighboring material, the excess nonlinearity of an imperfect interface can be detected without interference from bulk nonlinearity by using reflection mode of inspection. Using the perturbation approximation method, the nonlinear reflection and transmission coefficients of the imperfect interface can be calculated as follows:

$$T^{(n)} = -R^{(n)} = \frac{1}{2}\omega_1\omega_2 Z_s^2 (S_{n2}\sin 2\theta_1 \sin 2\theta_2 - S_{n3}\cos 2\theta_1 \cos 2\theta_2) \tag{3}$$

Here, ω_1 and ω_2 are the two angular frequencies of the primary shear waves; θ_1 and θ_2 are the two incident angles; Z_s is the shear wave acoustic impedance; and S_{n2} and S_{n3} are the two

nonlinear normal compliance coefficients. Equation 3 has been numerically validated by FE simulations. Though in the finite interfacial stiffness model the nonlinear normal interfacial stiffness coefficients are directly defined, in the thin interphase layer model the two nonlinear normal compliance coefficients are expressed in the form of Lamé constants, Murnaghan coefficients, and the thickness of the interphase layer (see appendix A for details).

Comparisons between the analytical predictions and the numerical simulations of the two models are shown in figures 4 and 5. All the related material parameters used in the simulations are listed in tables 2 and 3. The numerical simulation results are in good agreement with the analytical approximation developed for both models. The small systematic error is caused by the fact that infinite plane waves were used in the analytical approximation; in the simulation, the waves had finite beam width. The resulting wave diffraction is the reason for the deviation between the simulation results and analytical prediction. Note that the thin interphase layer model is actually equivalent to a special case of the nonlinear interfacial stiffness model in which the two effective nonlinear compliance coefficients are equal to each other:

$$S_{n2} = S_{n3} = -\frac{(\lambda + 3\mu + 2m)\,d}{4\mu^2(\lambda + 2\mu)} \tag{4}$$

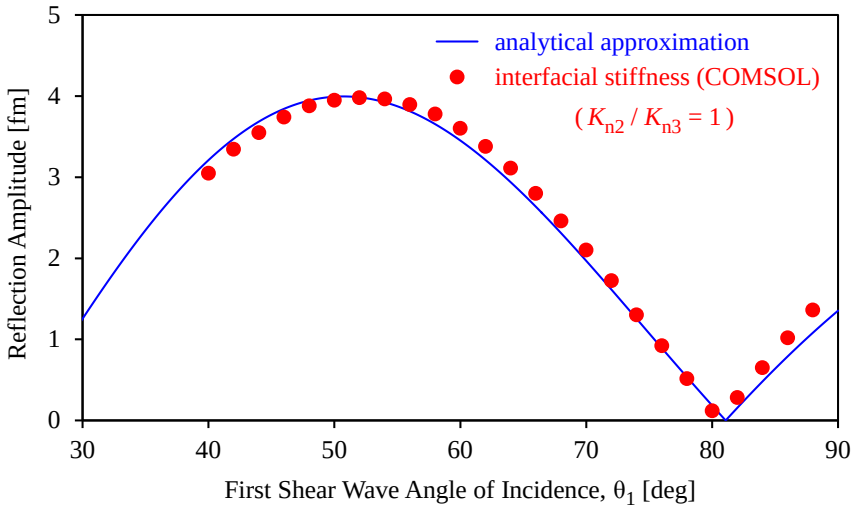

(a)

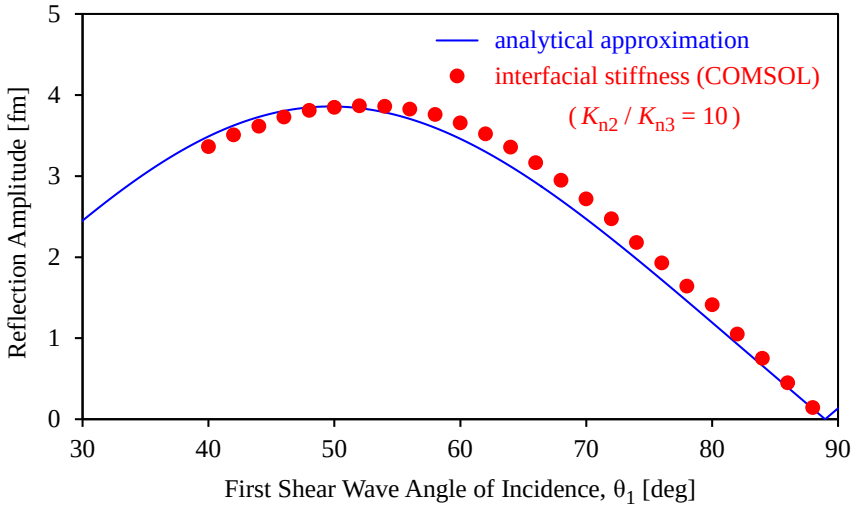

(b)

Figure 4. Comparison between analytical approximations and numerical results for the nonlinear reflection from an imperfect interface of finite interfacial stiffness with (a) K_{n2} / K_{n3} = 1 and (b) K_{n2} / K_{n3} = 10 (see table 2 for details)

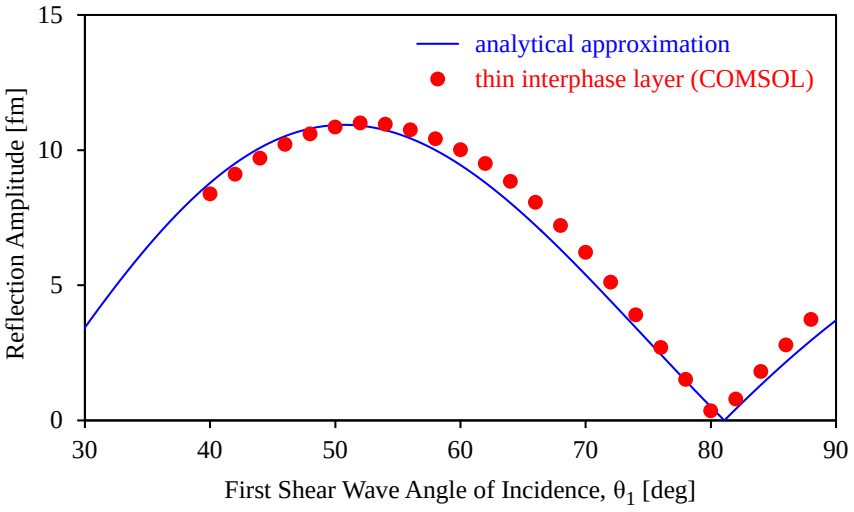

Figure 5. Comparison between analytical approximation and numerical results for the nonlinear reflection from a thin interphase layer (see table 3 for details)

Table 2. Material parameters used in the nonlinear finite stiffness model for figure 4

	ρ [kg/m^3]	λ [GPa]	μ [GPa]	K_{n1} [N/m^3]	K_{n2} [N/m^4]	K_{n3} [N/m^4]	K_{t1} [N/m^3]
Host Material	4456	81.72	45.89	N/A	N/A	N/A	N/A
Imperfect Interface #1	N/A	N/A	N/A	10^{17}	10^{27}	10^{27}	10^{17}
Imperfect Interface #2	N/A	N/A	N/A	10^{17}	10^{27}	10^{26}	10^{17}

Table 3. Material parameters used in the thin nonlinear interphase layer model for figure 5

	d [μm]	ρ [kg/m^3]	λ [GPa]	μ [GPa]	*l* [GPa]	*m* [GPa]	*n* [GPa]
Host Material	N/A	4,456	81.72	45.89	0	0	0
Imperfect Interface #3	10	4,456	81.72	45.89	0	-20,000	0

Based on equation 3, the normalized reflection coefficient versus angle of incident, θ_1, for various interfacial compliance ratios is plotted in figure 6. Figure 6 indicates that, for large values $S_{n3}/S_{n2} > 30$, the nonlinear transmission produced by an imperfect interface also decreases with decreasing angle of incidence, θ_1, below the bulk optimized angle; therefore, the bulk nonlinearity cannot be easily suppressed in the transmitted longitudinal wave by lowering the inspection angles as it was done in Escobar-Ruiz et al. [8]. In such cases, reflection mode of operation is preferable.

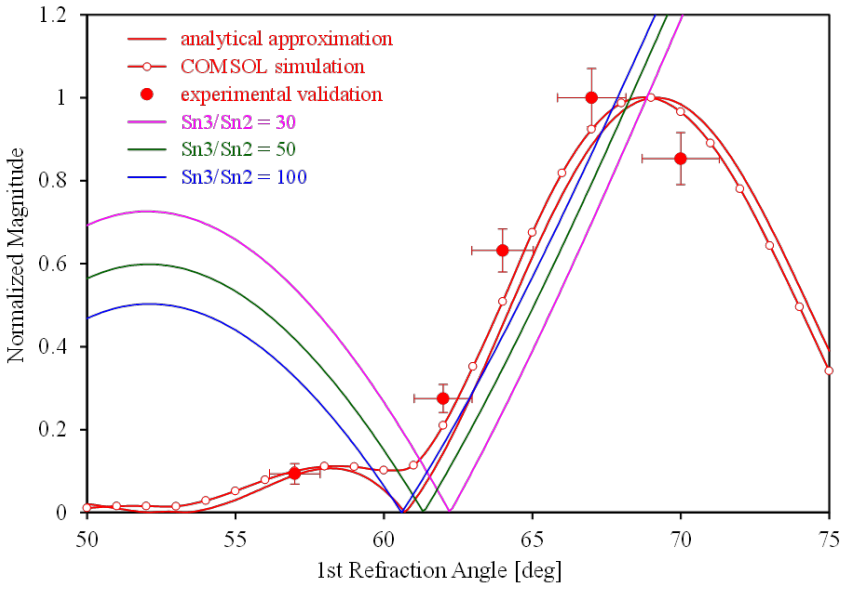

Figure 6. Analytical approximation of the transmission coefficient for interface and bulk nonlinearity (all values are normalized to the optimal bulk nonlinearity)

2.2 PRELIMINARY TESTS ON DIFFUSION-BONDED TI-6AL-4V SPECIMENS

Using the previously built experimental setup at University of Cincinnati, preliminary tests were conducted on a set of diffusion-bonded Ti-6Al-4V specimens provided by the industrial partner Rolls-Royce Corp® (RRC). A schematic illustration of the experimental arrangement is shown in figure 7. Eight Ti-6Al-4V diffusion-bonded specimens were created for this series of tests and an intact Ti-6Al-4V plate of double thickness was used as a reference piece to represent a perfect bond. To obtain a range of different bond qualities, the bonding time, temperature, and compressive stress level were set differently for each specimen during bonding. The quality of the diffusion bonds was assessed by RRC using cross-boundary grain growth (CBGG) measurements, which represents the proportion of grains that were observed to have grown across the interface and were therefore fully bonded [23]. Micrographs for each sample were taken approximately halfway between the center and the edge of the specimens at 500-times magnification, and each was analyzed to detect the percentage CBGG per unit area. Note that CBGG is not the inverse of interfacial percentage voiding, but instead represents a more statistically robust, if somewhat conservative, measure of the diffusion-bond quality [24, 25]. Unlike interfacial percentage voiding, CBGG is not directly susceptible to the measurement error associated with grains that are in close proximity to each other across the interface but do not offer the bond any significant strength [26]. Table 4 shows the measured CBGG values for all the samples. Figure 8 shows representative micrographs for samples 1 (6.59% CBGG), 3 (48.0% CBGG), and 7 (85.1% CBGG).

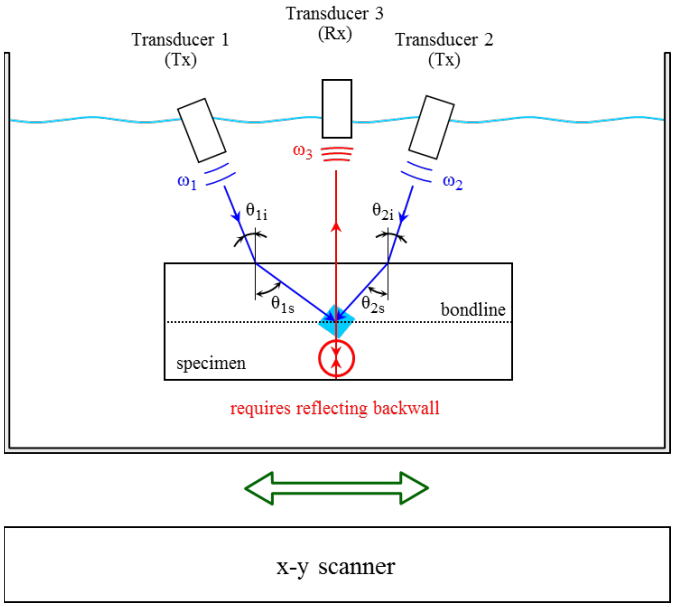

Figure 7. Schematic illustration of one-sided transmission experimental setup for bulk nonlinearity measurement

Table 4. CBGG for each specimen used in the initial validation experiment (100 % CBGG represents a perfect diffusion bond)

Sample No.	1	2	3	4	5	6	7	8	9
CBGG [%]	6.59	32.7	48.0	68.8	73.2	79.3	85.1	86.0	100
Temp. [°C]	695	745	745	745	795	845	915	775	800
Time [hrs]	2	2	3	2	2	2	2	4	2

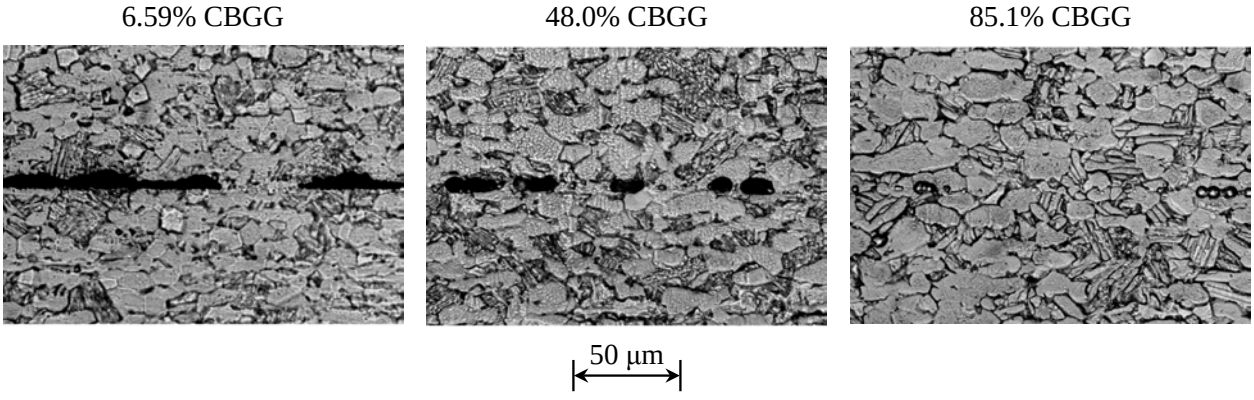

Figure 8. Micrographs of diffusion-bonded Ti-6Al-4V specimens 1, 3, and 7 at 500-times magnification, showing progressively higher diffusion-bond quality as quantified by the CBGG percentage

Both conventional linear and bulk nonlinear C-scan images were acquired for all the

diffusion-bonded Ti-6Al-4V specimens. The scanning area was 2″ x 2″ at the center of the specimens. The linear C-scan images were based on the measured magnitude of the 10-MHz spectral component of the longitudinal wave reflected from the imperfect interface. Figure 9 shows the detected linear reflection for different diffusion bonds. The measured linear reflections from different diffusion bonds were normalized to the linear reflection detected from the worst bonded specimen. Figure 9 shows that the linear ultrasonic responses are indistinguishable from one another for bond qualities greater than approximately 70% CBGG. Therefore, nonlinear measurements are needed to distinguish higher-quality diffusion bonds. To perform nonlinear measurements based on non-collinear shear wave mixing, the frequencies of the two shear waves were 4.5 MHz and 5.5 MHz, respectively, with pulse duration of 8 μs. In the first version of this study's nonlinear ultrasonic inspection system, rather low (≈200 W) peak electric power was used to drive the ultrasonic transmitters. By using external filters, the second harmonics with the frequency components of 9 MHz and 11 MHz were sufficiently suppressed. The two shear waves were timed to reach the center of the specimen at the same time, and the generated longitudinal wave signal, which had the frequency of 10 MHz, hit the back wall surface of the specimen and after reflection was picked up by the receiving transducer.

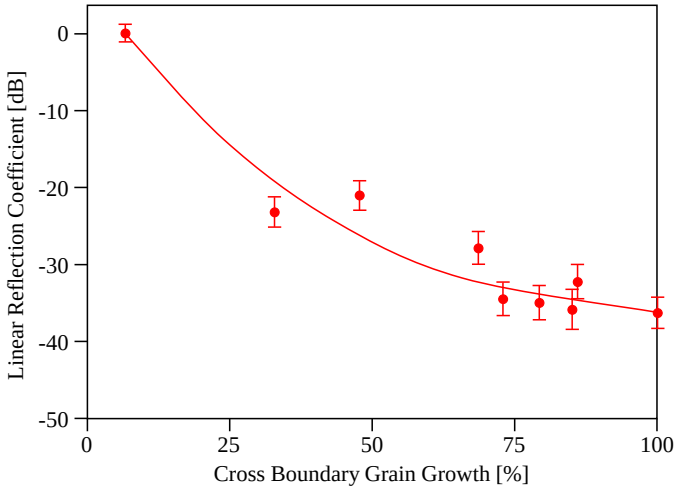

Figure 9. Normalized linear reflection coefficient versus CBGG in Ti-6Al-4V diffusion bonds

To investigate how well the bulk nonlinearity could be suppressed by misaligning the system from the bulk resonance condition, two nonlinear measurements were conducted on these Ti-6Al-4V specimens. The first experiment focused on detecting the optimized bulk nonlinearity, whereas the second experiment detected the nonlinearity with the system misaligned for higher selectivity to the diffusion-bonded interface. The experimental parameters used for bulk and interface configurations are listed in table 5.

Table 5. Experimental parameters for bulk and interface configurations

	φ [°]	θ_{1i} [°]	θ_{2i} [°]	θ_{1s} [°]	θ_{2s} [°]	S [mm]
Bulk	118.6	25.4	20.9	68.0	50.6	47.0
Interface	96.4	22.0	18.1	54.0	42.4	29.1

The normalized nonlinear responses in bulk and interface configurations are shown in figure 10. The measurement conducted in the interface configuration was repeated twice to verify its reproducibility. Previous analytical and numerical studies indicated that misaligning the incident angle by 10° suppresses the bulk nonlinearity by approximately 20 dB. Figure 10 shows that misaligning the system reduced the total (bulk plus interface) nonlinearity by approximately 3 dB in the experiment. Figure 11 shows both the previously presented linear response and the nonlinear response obtained in the more sensitive interface configuration. These results indicate that the nonlinear measurement helps distinguish diffusion bonds that have CBGG values above 70%. However, this approach is not sufficient enough to distinguish good bonds from very good bonds above 70% CBGG due to the fact that, in transmission mode of inspection, the nonlinearity generated by the diffusion bond has to compete with the relatively high bulk nonlinearity of the host material. Therefore, it is important to implement the reflection mode of inspection to better eliminate the adverse influence of bulk nonlinearity and to further increase the inspection sensitivity to subtle imperfections found in high-quality diffusion bonds.

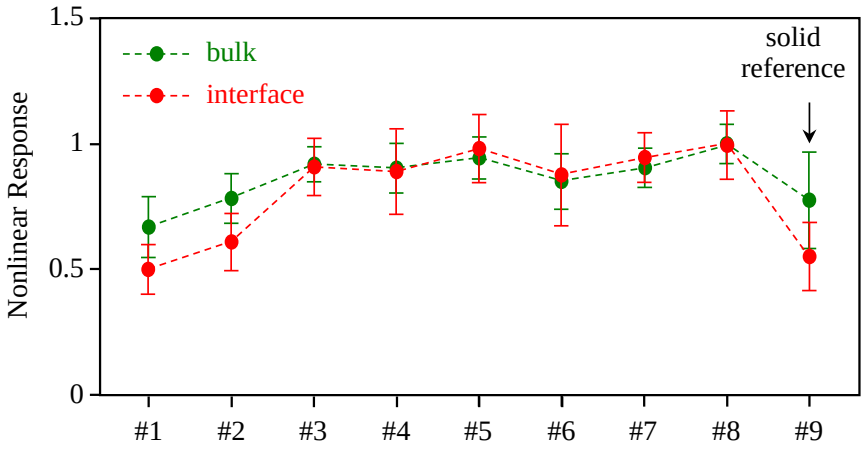

Figure 10. Normalized nonlinear responses in bulk and interface configurations

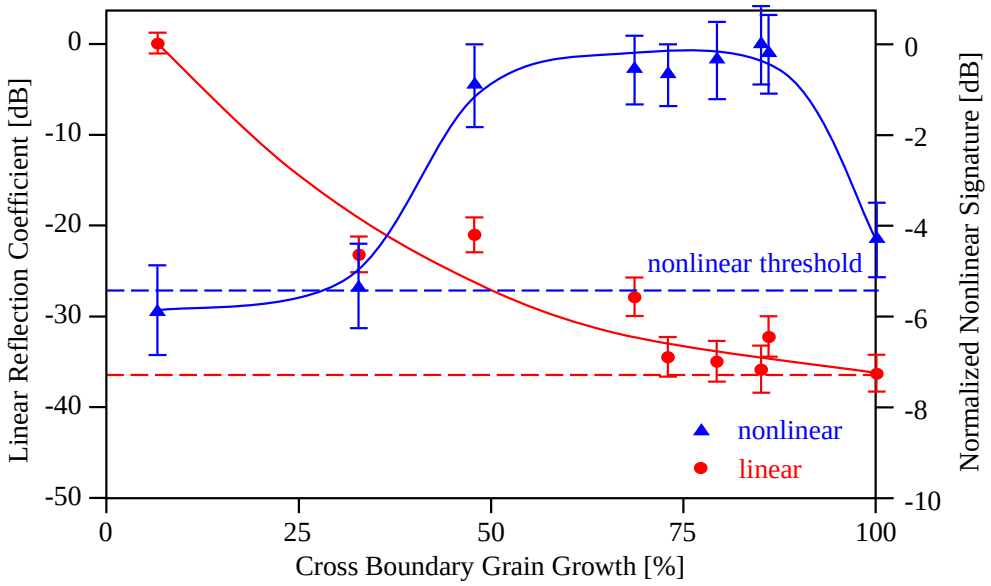

Figure 11. Comparison between normalized linear reflection and nonlinear signature

3. HARDWARE DEVELOPMENT

The preliminary analytical, computational, and experimental results presented in section 2 all indicated that major hardware and software modifications will be needed to upgrade the existing first version of the nonlinear ultrasonic inspection system for high-resolution imaging and quantitative characterization of subtle interface imperfections in high-quality diffusion-bonded engine components. This section describes the extensive hardware modifications made on the nonlinear inspection system to facilitate the goals of this development and research project. In section 4, the associated software upgrades are discussed.

3.1 SYSTEM-LEVEL DESIGN CONFIGURATION

To make the nonlinear ultrasonic inspection system suitable for detecting weak nonlinear reflections from high-quality diffusion-bonded interfaces, the hardware and software of the existing system had to be significantly redesigned. The simplified block diagram of the first version of the pulser/receiver system is shown in figure 12. For the excitation of the primary shear waves, the system transferred the numerically calculated wave forms from the controlling computer to two DS 345 arbitrary function generators (AFGs) to generate the driving signals, while the whole system was synchronized by a third AFG. After amplification, the output signals of two BTM00250 AlphaSA RF Amplifiers were driving two 5-MHz, 0.25″-diameter immersion transducers. The nonlinear signal was received by a 10-MHz, 0.5″-diameter, 5″ focal length transducer and amplified by a 5072 PR pulser/receiver. The signal then was digitized using an LT 264M Digital Oscilloscope and transferred back to the master computer through a General Purpose Interface Bus (GPIB) for further analysis.

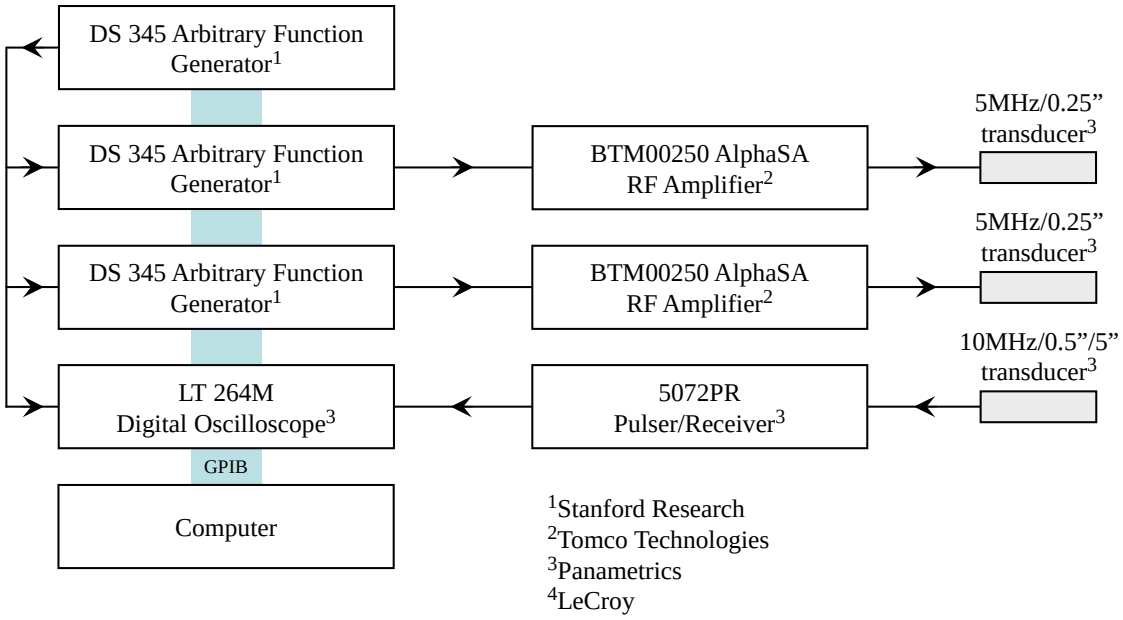

Figure 12. Simplified block diagram of the first version of the pulser/receiver system

The authors' goal was to build not just a more-advanced inspection system with higher sensitivity, but also a more compact one. For this purpose, the three standalone AFGs were replaced with a single CompuGen 4302 four-channel AFG card that plugs directly into the computer through a peripheral component interconnect (PCI) bus. The pulser/receiver was also replaced with an AD-IPR-1210 ADC/pulser/receiver PCI card. The gated power amplifiers used in the first version of the nonlinear inspection system offered only 200 W peak power so that the transmitters generated shear wave displacements at the low end of the range required to produce interface closure in tight kissing bonds. To increase the system's sensitivity to clapping nonlinearity, these amplifiers were replaced with more powerful BTO4000 AlphaS RF Amplifiers. This upgrade increased the peak electric driving power to 4000 W. The simplified block diagram of the upgraded second version of the pulser/receiver system is shown in figure 13.

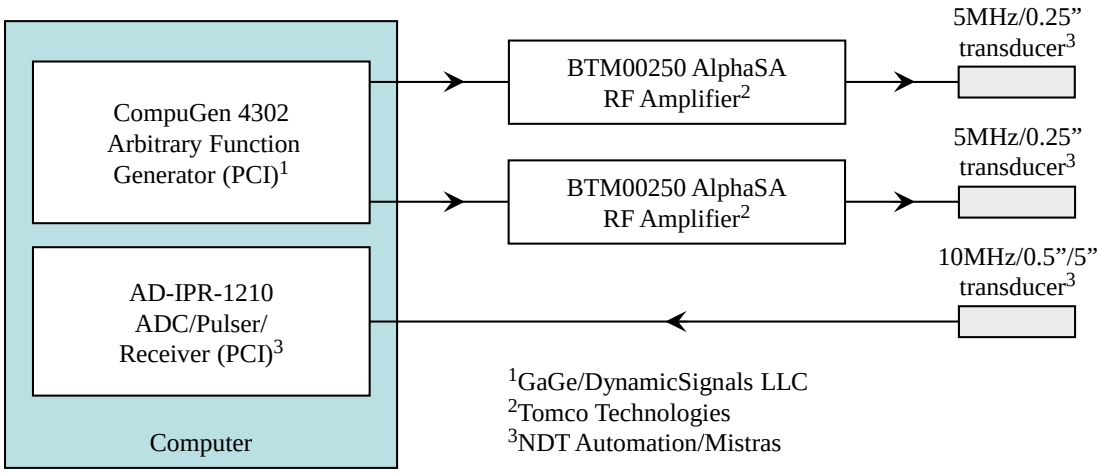

Figure 13. Simplified block diagram of the upgraded second version of the pulser/receiver system

To supplement the ADC/pulser/receiver board and more powerful gated amplifiers in the upgraded second version of the nonlinear inspection system, two MFA-PPD linear stages and two URS50BPP rotational stages from Newport Corporation were also purchased for the necessary automation of transducer alignment procedure. These components were necessary to automate the transducer alignment procedure and bring it under computer control via an integrated software system described in section 4.5.

3.2 NEW HARDWARE CONSTRUCTION

The detailed block diagram of the final system configuration is shown in figure 14. Both the CompuGen 4302 AFG and the AD-IPR-1210 ADC/pulser/receiver have been integrated into the computer and the two boards communicate with the computer through the PCI bus. Channel #1 (CH1) of the CompuGen 4302 AFG was programmed to generate the master trigger signal for the whole inspection system that also serves as the switching signal for the two gated amplifiers. The required switching signal for the gate input of the power amplifiers is 0–5 V; therefore, the gate signal from CH1 of the AFG, which is limited to ±0.87 V, is too low to turn on and off the gated power amplifiers. Therefore, a SIM 983 scaling amplifier is used to amplify the gating signal. Channels #2 and #3 (CH2 and CH3) produce the software controlled input signals for the two power amplifiers. Finally, Channel #4 (CH4) generates a polarity signal to synchronize the software in cases in which phase measurements are needed for coherent averaging of the measured nonlinear signals. To read this low-frequency square wave pulse into the nonlinear signal analyzer, a BNC-2110 ADC that communicates with the computer through a GPIB interface is used.

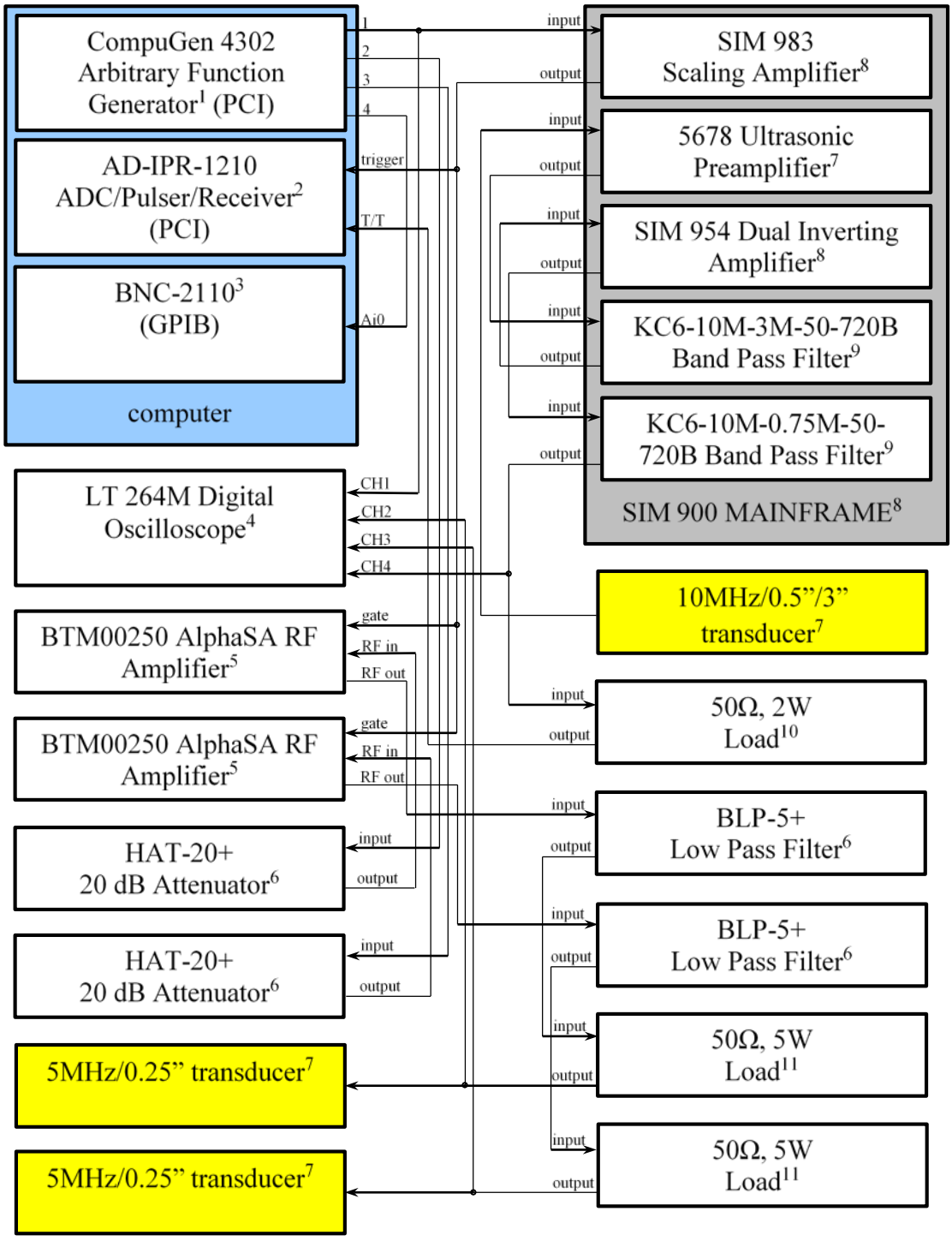

Figure 14. Block diagram of new nonlinear imaging system

After the driving pulses are amplified by the gated power amplifiers, two 5-MHz low-pass filters are used to filter the driving signals to suppress any higher harmonics produced by nonlinear distortion in the power amplifiers. After the nonlinear signal is picked up by the receiver, a Panametrics 5678 ultrasonic preamplifier is used to increase the level of this weak signal by

40 dB. This preamplifier has very low input noise density of ≈2 $nV/Hz^{1/2}$, which is necessary to increase the system's SNR. A band pass filter (BPF) with center frequency of 10 MHz and bandwidth of 3 MHz follows the preamplifier to suppress the spurious higher harmonics of the excitation signals. After filtering, another 24 dB gain is added to the level of the nonlinear signal by a SIM 954 dual inverting amplifier. This stage is followed by a second BPF with center frequency of 10 MHz and a much narrower bandwidth of 0.75 MHz to further suppress unwanted spectral components in the detected nonlinear signal. The SIM 983 scaling amplifier, 5678 ultrasonic preamplifier, SIM 954 dual inverting amplifier, and two filters are all integrated into a SIM 900 mainframe that provides power for these hardware components. The manufacturers of the individual components are listed in table 6.

Table 6. List of the manufacturers of the individual hardware components

ID in Figure 14	Manufacturer
1	DynamicSignals LLC
2	NDT Automation
3	National Instruments
4	Teledyne LeCroy
5	Tomco Technologies
6	Mini Circuits
7	Panametrics
8	Stanford Research Systems
9	TTE
10	Pomona Electronics
11	BroadWave Technologies

3.3 TRANSDUCER POSITIONING AND ORIENTATION

One of the significantly improved features of the upgraded nonlinear imaging system is the automated transducer alignment option that replaced the former time-consuming manual alignment of the transducers based on the analytically estimated inspection angles and positions. Figure 15 shows a schematic illustration of the upgraded transducer alignment system. The four degrees of freedom (DOFs) that were automated are shown in green, whereas the three axial DOFs that remained manually adjustable are shown in purple. To automate the alignment procedure, two MFA-PPD linear stages and two URS50BPP rotational stages from Newport Corporation were purchased and installed in the nonlinear inspection system.

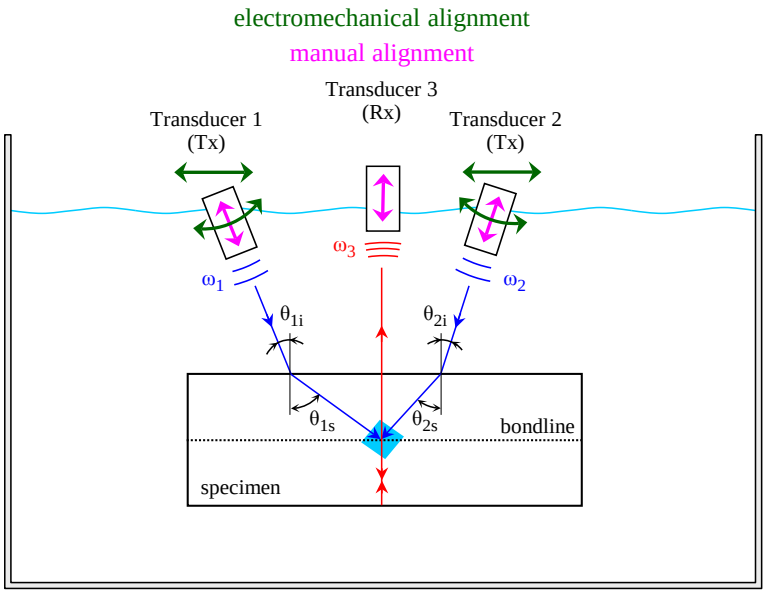

Figure 15. A schematic illustration the four automated DOFs (green) and three axial DOFs (purple) that remained manually adjustable

New fixtures were designed and built to mount the transducers on those electromechanical stages, as shown in figure 16. With the linear and rotational stages implemented into the system, the computer is able to control the angles of two transmitting transducers and the separation distance between them independently via software. The LabVIEW™ program for the linear and rotational stages was first separately tested. These stages greatly increased the accuracy and speed of the alignment procedure. In the old system, the manual precision of the rotation was only 0.5°. Because the transducer is immersed in water, 0.5° angular alignment error for the incident wave in water can cause 1.5° angular error for the refracted shear wave in the specimen. According to previous analytical and numerical studies, 1.5° angular error can substantially reduce the strength of the mixed nonlinear signal. In the upgraded electromechanical system, the rotational error has been reduced to 0.1° and, because of the alignment optimization program discussed later, the alignment procedure became much more accurate, easier, and faster.

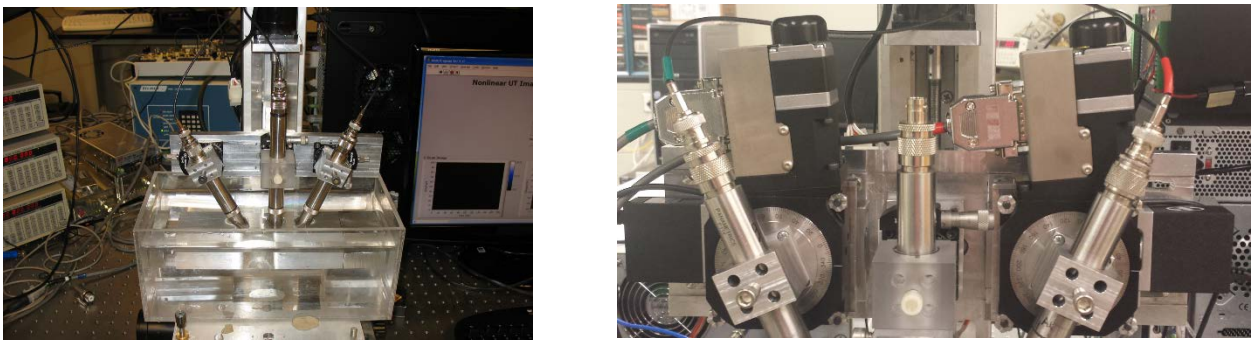

(a) (b)

Figure 16. The (a) first version of the non-collinear mixing immersion scanner and (b) the upgraded second version with electromechanical alignment

4. SOFTWARE DEVELOPMENT

To fully exploit the enhanced capabilities of the redesigned nonlinear inspection system, it was important to establish fast and reliable communication between the computer and all the incorporated hardware components so that pulse generation, data acquisition, scanning control, and image processing could be performed by a single master computer. The purpose of the integration was not only to make the system more compact but also more sensitive. For this purpose, the spurious nonlinearity from various system components, such as amplifiers, transducers, and immersion fluid, was suppressed by not only hardware means like filtering but also by software means. In particular, a novel four-way polarity flipping technique was developed and implemented in the system. In this section, the main features of a LabVIEW-based software package developed for the new nonlinear imaging system are presented.

4.1 DIGITAL SIGNAL PROCESSING SOFTWARE

Figure 17 shows the main panel of the LabVIEW software, which includes the pulse generation and scanning control parts. The upgraded inspection system uses a four-channel CompuGen 4302 AFG to produce the analog pulses for the two transmitting transducers. The conversion rate of the CompuGen 4302 board can be set to 75 MHz, 150 MHz, or 300 MHz. When the conversion rate is too high, the function generator produces too many data points for a given window length, thereby increasing the calculation and transfer time needed to produce the chosen waveform during the setup period. For our purposes, the lowest conversion rate, f_c = 75 MHz, was chosen as a default value, and the total setup time for generating the two driver signals was approximately 30 seconds. The trigger rate of the pulses can be selected arbitrarily. However, integer multiples of 50 Hz should be avoided when selecting the trigger rate because, in such cases, the board produces somewhat distorted signals with unexpected high-frequency components. Channel #1 of the CompuGen 4302 AFG was programmed to generate a trigger signal for the whole inspection system that also serves as the switching signal for the two gated amplifiers. Once the temporal length of the gate signal is defined, the number of consecutive data points that need to be set high can be determined by multiplying the gate length with the chosen 75 MHz sampling rate of the digital-to-analog converter (DAC). The logical high level is set to +0.87 V, which is the highest output voltage that can be generated by the CompuGen 4302 AFG,

and the logical low level is set to 0V.

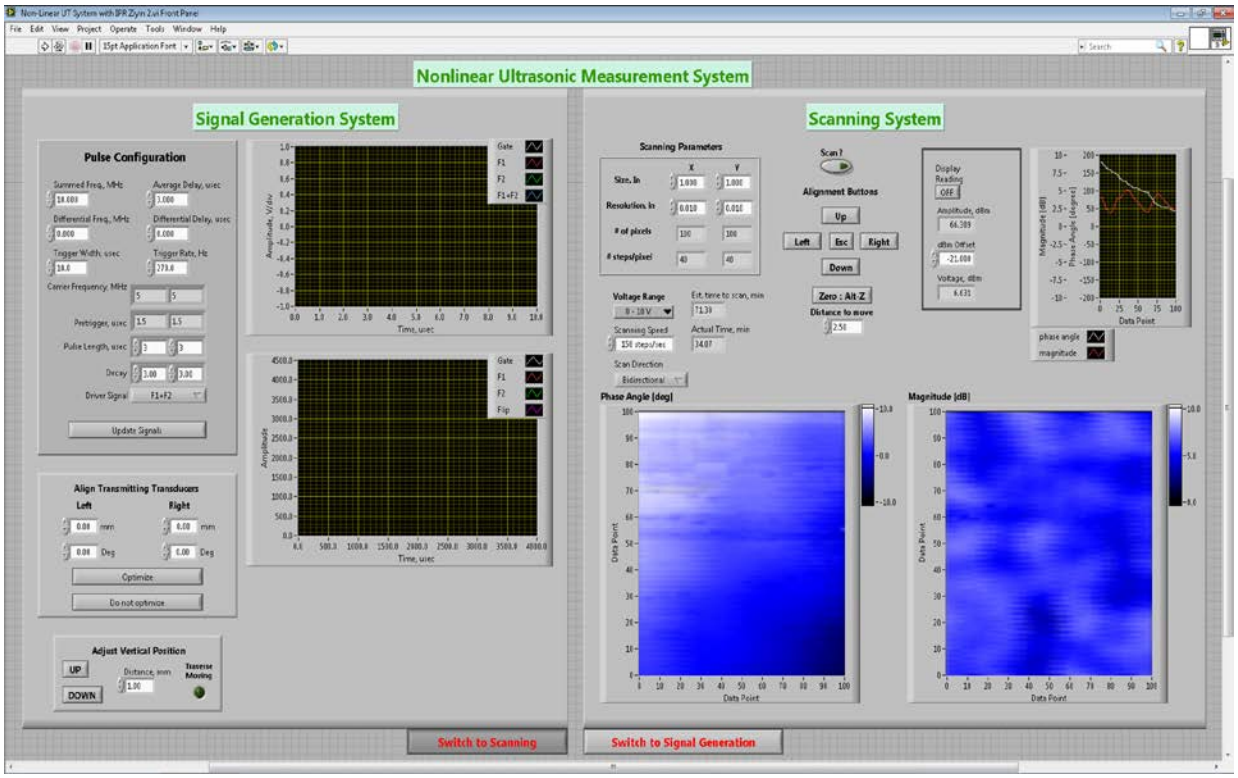

Figure 17. Main software control panel of the nonlinear ultrasonic measurement system

Rather than adjusting the delays of the two driver signals independently within the gate, they can be controlled in unison by either adjusting the average delay or the differential delay. The former is used to move the two signals relative to the gate, whereas the latter is used to ensure that the two shear pulses arrive to the center of the interaction zone exactly at the same time regardless of the mechanical position and orientation of the transducers. Output channels #2 and #3 of the AFG are programmed to generate the analog signals for the transmitting transducers through the gated amplifiers. The carrier frequencies and temporal lengths of these two pulses can be independently defined. The two pulses are tapered sinusoidal tone bursts. Because they are programmed in the same way, only the first pulse, $g_1(t)$, will be described as an example:

$$g_1(t) = U_1 W(t - t_d)\sin[2\pi f_1 (t - t_d)] \tag{5}$$

where f_1 is the carrier frequency, t_d is the delay time, U_1 = 0.87 V is the pre-set amplitude of the signal, and $W(t)$ is a window function. The tapered window function that determines the envelope of the generated tone burst has a bell-shape curve as follows:

$$W(t) = \exp\left[-(\alpha \frac{t - t_p/2}{t_p/2})^2\right][H(t) - H(t - t_p)] \tag{6}$$

where α is a decay parameter used to control the shape of the envelope within the window, t_p is pulse length, and H denotes the Heaviside step function. The 12-bit CompuGen 4302 AFG converts the calculated numerical values from zero to $N = 4096$ to the voltage range between -0.87 V and +0.87 V. Accordingly, the tapered tone burst signal g_1 is digitized into a series of numerical values, $G_1(n)$, used to drive the DAC of the AFG:

$$G_1(n) = \frac{N}{2}\left[\frac{1}{U_1} g_1\left(\frac{n}{f_c}\right) + 1\right] \tag{7}$$

where n is the serial number of the data point and $U_1 = 0.87$ V and $f_c = 75$ MHz are the previously defined reference voltage level and selected conversion rate of the DAC, respectively.

Both analytical and numerical investigations indicated that the typical nonlinear reflection from an imperfect interface is very weak and, therefore, difficult to detect. Therefore, the SNR of the nonlinear imaging system had to be significantly increased to detect the nonlinear reflection signal from imperfect interfaces. Frequency separation was used in the first version of the nonlinear inspection system to separate the weak mixed nonlinear signal from the stronger second harmonic signals of the primary waves. According to this approach, the frequencies of the two shear waves were set to 4.5 MHz and 5.5 MHz so that the sought mixed signal had the summed frequency of 10 MHz, whereas the second harmonic signals had frequencies of 9 MHz and 11 MHz. By using a BPF of 10-MHz center frequency and sufficiently narrow bandwidth (e.g., 500 kHz), the mixed nonlinear signal could be filtered out while the other spurious nonlinear components were significantly suppressed. However, this spectral separation was particularly difficult when the object under test had relatively small thickness because the applied tone burst had to be limited in length, which in turn widened its bandwidth. Because of this widening, the 10-MHz mixed signal could not be sufficiently discriminated from the nearby nonlinear components of 9-MHz and 11-MHz frequency using narrow-band filtering only.

To increase the critical SNR of the nonlinear inspection system, a novel four-way polarity flipping scheme was implemented that effectively suppressed all spurious signals regardless of their frequency content. This technique requires generating all possible polarity combinations of the input signals; the output signals acquired from each combination will have to be averaged in a certain way to fully eliminate all the spurious components. Assuming $g_1(t)$ and $g_2(t)$ to be the input signals for the two shear wave transducers, the received signal, $h(t)$, for all possible polarity combinations can be written as follows:

$$h^{(++)} = N_1\{g_1 + g_2\} + N_2[g_1^2 + g_2^2 + 2\,g_1\,g_2] + \ldots \tag{8a}$$

$$h^{(+-)} = N_1\{g_1 - g_2\} + N_2[g_1^2 + g_2^2 - 2\,g_1\,g_2] + \ldots \tag{8b}$$

$$h^{(--)} = N_1\{-g_1 - g_2\} + N_2[g_1^2 + g_2^2 + 2\,g_1\,g_2] + \ldots \tag{8c}$$

$$h^{(-+)} = N_1\{-g_1 + g_2\} + N_2[g_1^2 + g_2^2 - 2\,g_1\,g_2] + \ldots \tag{8d}$$

where N_1 and N_2 are the linear and quadratic coefficients in the Taylor series of the system's overall transfer function. The received signals acquired from these four polarity combinations are averaged as follows:

$$\bar{h} = \frac{h^{(++)} - h^{(+-)} + h^{(--)} - h^{(-+)}}{4} = 2 N_2 g_1 g_2 \tag{9}$$

The averaged signal is proportional to the sought nonlinear mixed signal, $g_1 g_2$, and both the fundamental linear components and their spurious nonlinear second harmonic components are completely eliminated. This technique can dramatically increase the SNR and makes it possible to adjust the frequencies of the two primary shear waves without any limitation on the frequency selectivity of the BPF (e.g., the $a = f_2/f_1$ frequency ratio can be much lower than the usually used $a = 1.22$ value or even be set to unity). This technique has been implemented in the pulse generation software by linking four segments of the driving signal containing all possible polarity combinations listed in equations 8a–8d into four-pulse "sequences" that can be averaged after reception in a single operation at very high processing speeds.

In the pulse generation software, a sub-panel was created for setting the polarities of the two input signals, as shown in figure 18. The buttons in the first and second columns select the polarities of the first and second driving signals, respectively, and the four rows represent the four pulses in each sequence. The polarity of each pulse can be flipped as needed by clicking on the appropriate button. Figure 19 shows an example of the generated four combinations of the pulses driving the two transmitters. According to equation 9, in the default setting of ++, +-, --, -+, selective measurement of the mixed nonlinear signal can be achieved by flipping the polarity of each received pulse relative to the one preceding it during averaging and assuring that, in each measurement cycle, the number of pulses averaged is an integer multiple of four. It was found that this simple four-way polarity flipping technique suppressed by as much as 30–35dB the spurious nonlinear signals that are difficult to reject by band pass filtering, which dramatically increases the sensitivity of the nonlinear imaging system.

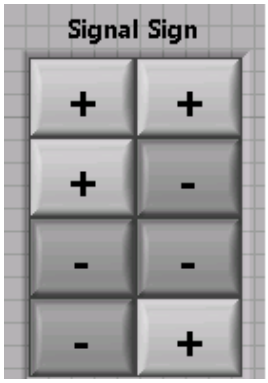

Figure 18. Polarity selection sub-panel

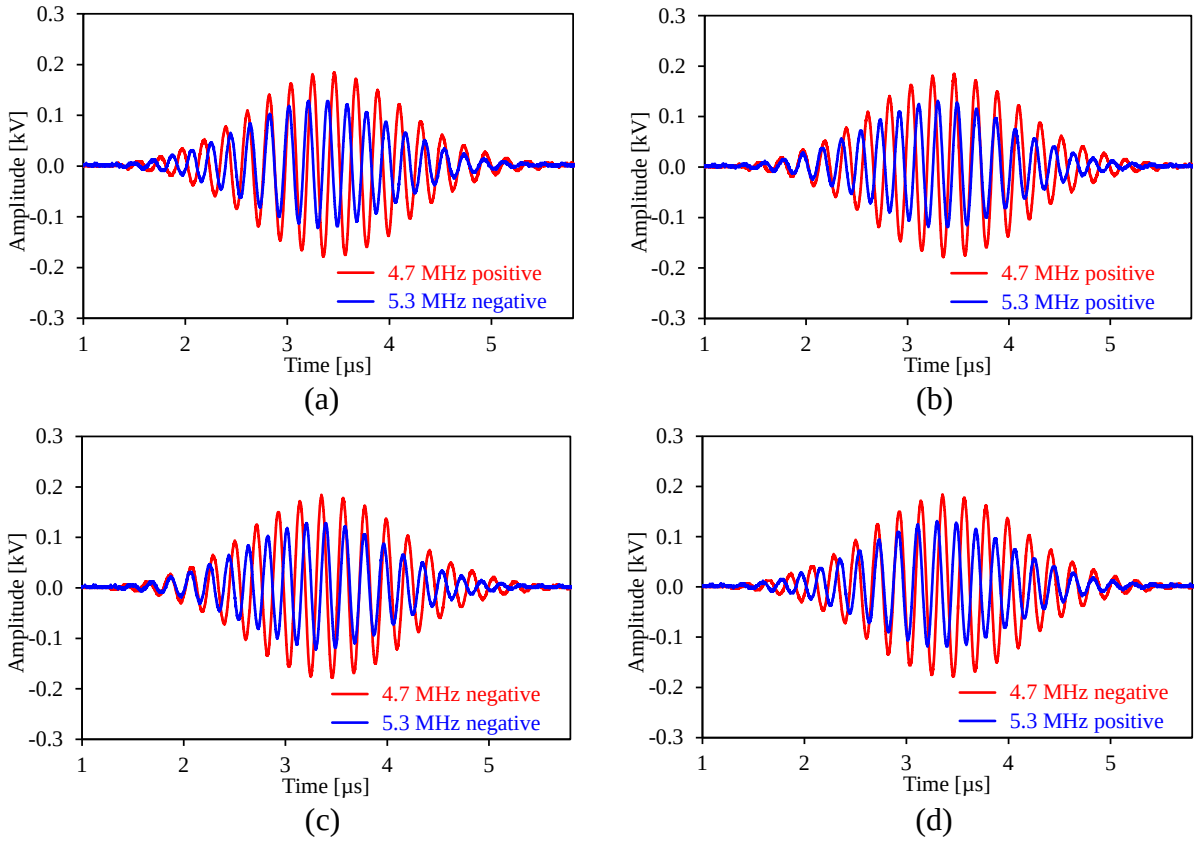

Figure 19. Four combinations of the driving pulses for the transmitting transducers after amplification

4.2 SCANNER CONTROL SOFTWARE

A unique feature of the developed nonlinear inspection system is that it is capable of generating intuitive C-scan images of the spatial distribution of nonlinearity in the specimens being tested. Commercial linear ultrasonic C-scan systems usually have large immersion tanks to accommodate different sizes of specimens and move transducers to scan the component being tested. The nonlinear imaging system developed in this project was designed for laboratory-level inspection of small specimens with regular shapes. Because three separate immersion transducers are needed for non-collinear mixing and the inspection angles and positions of all three transducers must remain the same throughout the scanning process, the specimen being tested is moved to do the scanning instead of moving the transducers. In the first version of the nonlinear imaging system, a custom built immersion tank of 12″ x 6″ x 5″ was mounted on a MAXY4009W1-S4 XY translation stage from Velmex for scanning purposes. In its basic configuration, the XY stage had a limited travel distance of 5″ x 5″, which was found insufficient in some cases. Therefore, the XY stage was disassembled and the x-axis slide was replaced with a single axis MN10-150-801-20 slide also from Velmex. This modification extended the x-axis travel distance to 12″. A bigger immersion tank of 16″ x 7″ x 4.5″ was also built and mounted on the redesigned stage to accommodate larger components.

The software for scanning control was also developed in LabVIEW. The scanning panel is

shown in figure 20. In the scanning program, the scanning speed of the two slides can be selected. The alignment buttons adjust the initial starting point at the center of the scanned area. The scanning area can be determined by defining the x- and y-axis scanning distances, and the resolutions for each direction can be independently selected. Based on these parameters, the number of steps for the stepping motors can be calculated. In the first version of the imaging system, there was only a single unidirectional mode of scanning, which means that the nonlinear signature was measured and recorded only when the specimen was moving from right to left. Unidirectional scanning eliminates positioning errors caused by inevitable backlash in the mechanical scanning system, but it is inefficient for large specimens to take no data when the tank is moving from left to right (i.e., half of the total scanning time). In addition to the hardware backlash problem, which could have been suppressed by mechanical improvements, the relatively long running averaging needed to achieve sufficient SNR for nonlinear imaging also causes an effective software backlash. In the revised version of the scanning system, the program was modified to record the nonlinear signature during scanning in both directions. This added option of scanning was named bidirectional scanning. Naturally, the part of the data collected when the specimen was moving from left to right needed to be reversed before storing the array as a whole. In addition, an adjustable offset was introduced between odd and even image rows to compensate for the above-mentioned hardware and software backlash. The new bidirectional scanning mode reduces the scanning time needed to cover the same inspection area with the same resolution by a factor of two.

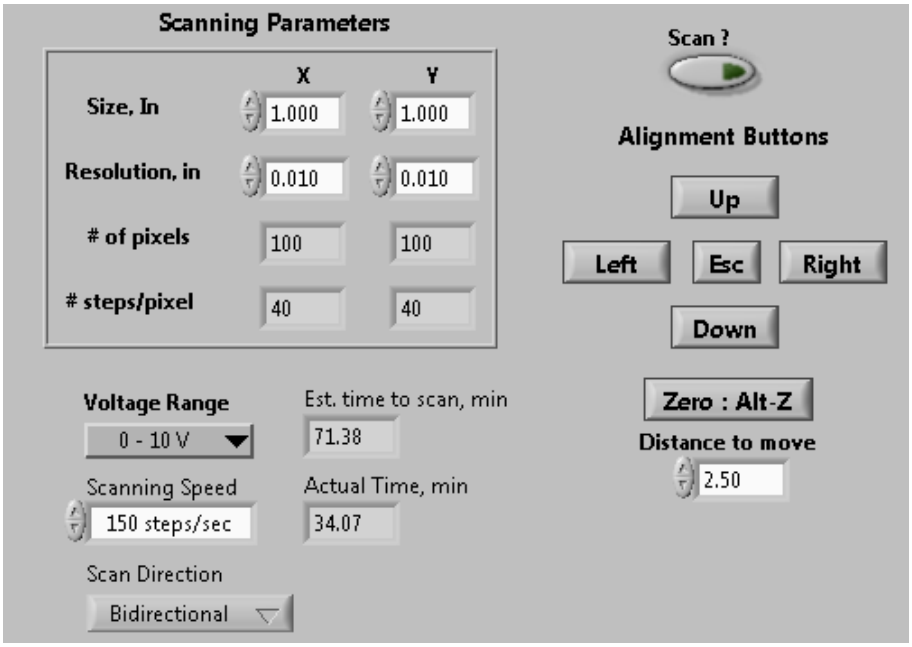

Figure 20. Scanning panel of the nonlinear imaging system

With the scanning size and resolution defined by the user, the pixel numbers along the x and y axes can be calculated. Based on the resolution selected, the step size of the stepping motor, and the pitch size of the lead screw, the number of steps for each pixel can also be calculated. Note that after the scanning speed has been selected by the user, the software can estimate how much time it will take to scan one pixel. This parameter is important because there is a refreshing time

for each measured data point in the signal processing part of the software. This refreshing time reflects the time consumed by averaging integer multiples of four-pulse sequences for a single measured data point. If the scanning speed is too fast, the time to scan one pixel is shorter than the refreshing time; therefore, there will not be enough time to acquire the necessary minimum one new data point for every pixel. If the scanning speed is sufficiently slow, the time to scan one pixel is longer than the refreshing time, and more than one data point will be collected for each pixel. In that case, the program will average all the data points for that pixel to further increase the SNR at the expense of longer total scanning time.

4.3 IMAGE PROCESSING SOFTWARE

In the first version of the nonlinear inspection system, the nonlinear signal picked up by the receiving transducer was analyzed by a digital oscilloscope that functioned as an analog-to-digital converter (ADC). The amplitude of the gated nonlinear signature and the magnitude of its 10-MHz frequency component were transferred to the computer through a GPIB interface, and two alternative nonlinear C-scan images were built up from these measured values. The processing speed allowed by this system configuration was low and the first version of the four-way polarity flipping technique had to be implemented using hardware switches. In the upgraded inspection system, the external oscilloscope was replaced by an AD-IPR-1210 ADC/pulser/receiver board that plugs directly into the motherboard of the controlling computer through a PCI bus. This multi-function board replaced the external digital oscilloscope and the external pulser/receiver. The received nonlinear signal can be directly digitized and transferred into the computer's memory at high speed, and further signal analysis can be performed effectively by software means. Thanks to the much improved communication speed through the PCI bus, the four-way polarity flipping scheme could be implemented by purely software means. The LabVIEW program developed for analyzing the nonlinear signature will be presented in detail in section 4.4.

After the necessary analysis of the measured nonlinear signature, the temporal waveform of the signal, the frequency spectrum of the gated part of the signal and the phase of the gated signal are all displayed. Figure 21 shows 1-D line scans and 2-D C-scans of the nonlinear signature as they appear on the control panel of the software. Though C-scan images were constructed from either the peak amplitude of the nonlinear signal or the magnitude of its 10-MHz frequency component in the first version of the system, the new system builds nonlinear images from the magnitude of the 10-MHz frequency component and its phase angle. It is necessary to scale the magnitude of the measured 10-MHz frequency component for displaying and recording purposes. This is achieved by choosing a reference magnitude level so that the measured amplitude falls within a -10 dB to +10 dB range.

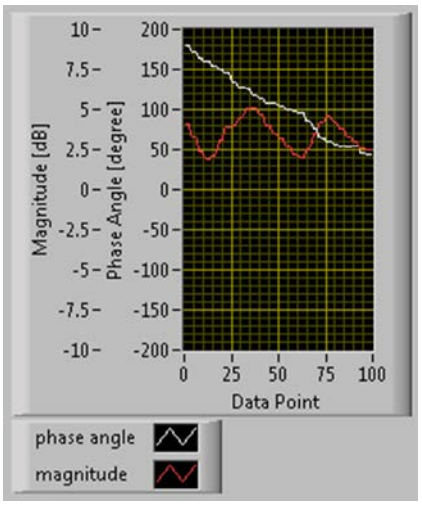

(a)

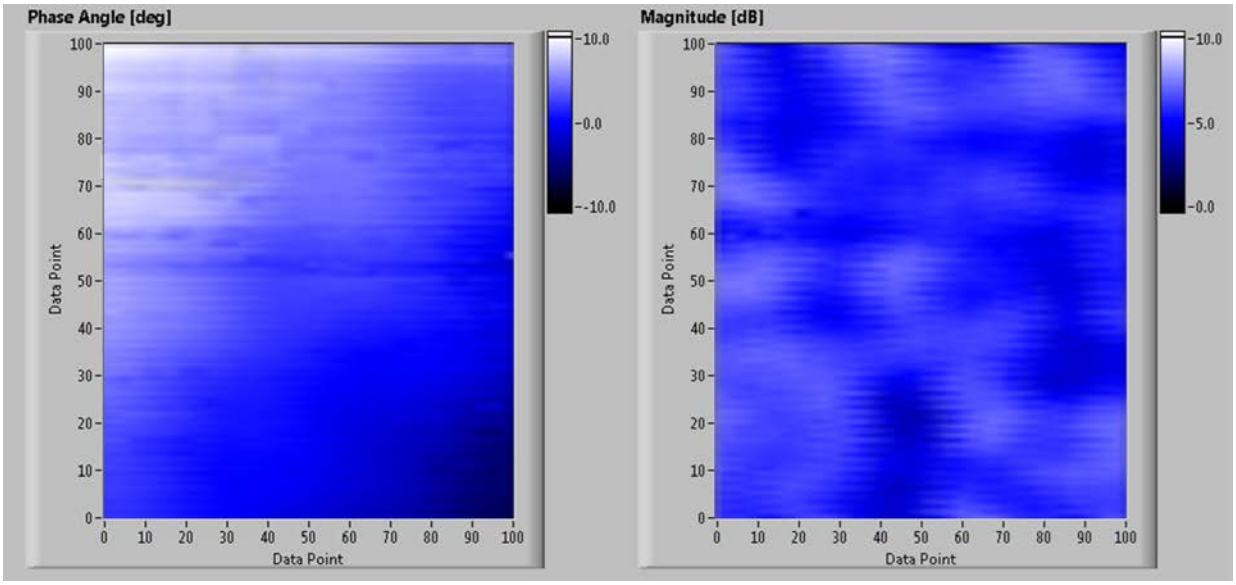

(b)

Figure 21. Nonlinear (a) 1-D line scans and (b) 2-D C-scans on the front panel of the software

4.4 NONLINEAR SIGNATURE ANALYSIS SOFTWARE

The control panel for the nonlinear signature analysis program is shown in figure 22. The AD-IPR-1210 ADC/pulser/receiver board replaced the digital oscilloscope and the external pulser/receiver. This board communicates with the computer through a PCI bus instead of through a GPIB interface, which significantly shortens the time for transferring data. The entire nonlinear signature analysis, which was previously performed mostly by the digital oscilloscope under external control, is now conducted in the LabVIEW program by the computer. With built-in SubVIs, which are similar to subroutines in text-based programming languages, LabVIEW is easy to optimize for nonlinear signature analysis. Similar to a digital oscilloscope,

the program can select the delay time, the width of the temporal window and the voltage scale to locate the nonlinear signal in the received waveform. The program can also numerically amplify the signal by using a gain function. Like an oscilloscope, the program also has a user-selected trigger mode to choose between external and internal mode, and the trigger level can be defined.

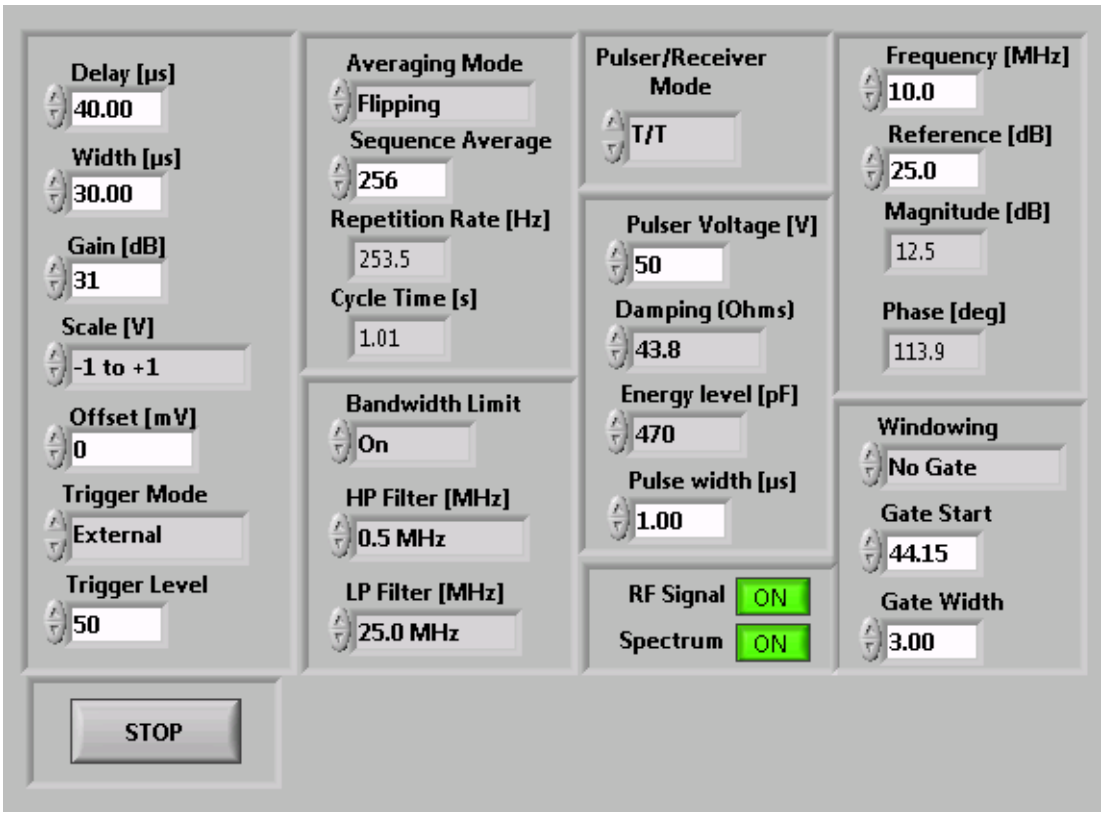

Figure 22. Nonlinear signature analysis control panel

To better analyze the signal in the frequency domain, a windowing function was implemented in the program. With the gate start time and gate width defined, the starting point and the length of the gate is calculated. There are two types of windowing methods implemented in the program: one is a rectangular windowing without tapering, and the other one is a Hanning window that is tapered by a weighted cosine function. After applying the windowing function to the gated signal, a fast Fourier transform (FFT) was used to calculate the spectrum of the received signal and to measure the magnitude and phase angle at the chosen center frequency. Another important modification made to the software was to implement the four-way polarity flipping averaging. This technique was described in section 4.1, in which the four possible polarity combinations of pulses were discussed along with how to link the four pulses into sequences and how to average the received pulses within each sequence to suppress unwanted components. In the nonlinear signature analysis panel, there is an averaging mode selection panel with three options:

1. No averaging
2. Averaging without polarity flipping
3. Averaging with polarity flipping

When options 2 and 3 are chosen, the number of averaged sequences can be defined by the user.

The repetition rate of four-pulse sequences is also user controlled. The default value of the repetition rate is 270 Hz, which corresponds to a pulse repetition rate of 1080 Hz. When the flipping option is selected, the ADC/pulser/receiver board stores four received pulses corresponding to the consecutive driving pulse combinations. Then the polarities of the second and fourth nonlinear pulses within each sequence are inverted before the four pulses are averaged. In this way, the spurious second harmonics are greatly suppressed. Equation 9 indicates that the proper order of the pulse combinations should always be ++, +-, --, -+, and so on. If the ADC/pulser/receiver board saves the received pulses without proper synchronization, the first pulse can be generated from any of the four polarity combinations. That is, the four consecutive nonlinear signals stored in the ADC/pulser/receiver board can be generated from:

1. ++, +-, --, -+
2. +-, --, -+, ++
3. --, -+, ++, +-
4. -+, ++, +-, --

With the averaging method programmed to invert the polarities of the second and fourth pulses before averaging all four pulses within the same sequence, the averaging yields $+\overline{h}$ in cases 1 and 3 and $-\overline{h}$ in cases 2 and 4. In the latter two cases, the spurious nonlinearity is still suppressed; however, there will be a 180° phase shift in the averaged mixed nonlinear signature. As a result, a random 180° phase change appears in the recorded waveform of the mixed nonlinear signal, and no coherent pixel averaging can be applied to the nonlinear image. To overcome this problem, output CH4 of the AFG is used to generate a square wave synchronizing signal at half the pulse repetition frequency, which is typically 540 Hz. The rising edge of this synchronizing signal occurs 600 μs after the “non-inverted” pulse combinations (i.e., pulse pairs with ++ and -- polarity combinations are generated).

This square wave is read into the nonlinear signature analysis software through an AD converter and allows phase-proper averaging of long series of sequences and different pixel values. When the ADC/pulser/receiver board reads its first nonlinear signal, it also reads the synchronizing square pulse. If the synchronizing signal is at its high level, then the first nonlinear signal stored was generated from either +- or -+ polarity combinations. Therefore, in those cases, the polarity of the averaged nonlinear signal is inverted to compensate for the 180° phase shift. FFT is applied to the averaged nonlinear signature, and the magnitude and phase angle of each frequency component can be calculated. Using SubVIs included with the software of the ADC/pulser/receiver board, it can be also used as a linear pulser/receiver. By selecting the pulser/receiver mode, the inspection system can be easily switched between conventional linear and mixing nonlinear inspection modes using the same control program.

For example, figure 23 shows a typical detected bulk nonlinear signal including multiple reflections within the specimen (yellow) and the gate window (green) as it appears in the waveform display of the LabVIEW program. Figure 24 shows the magnitude and phase spectra of the processed nonlinear waveform after applying a Hanning window to the principal nonlinear pulse before calculating its FFT.

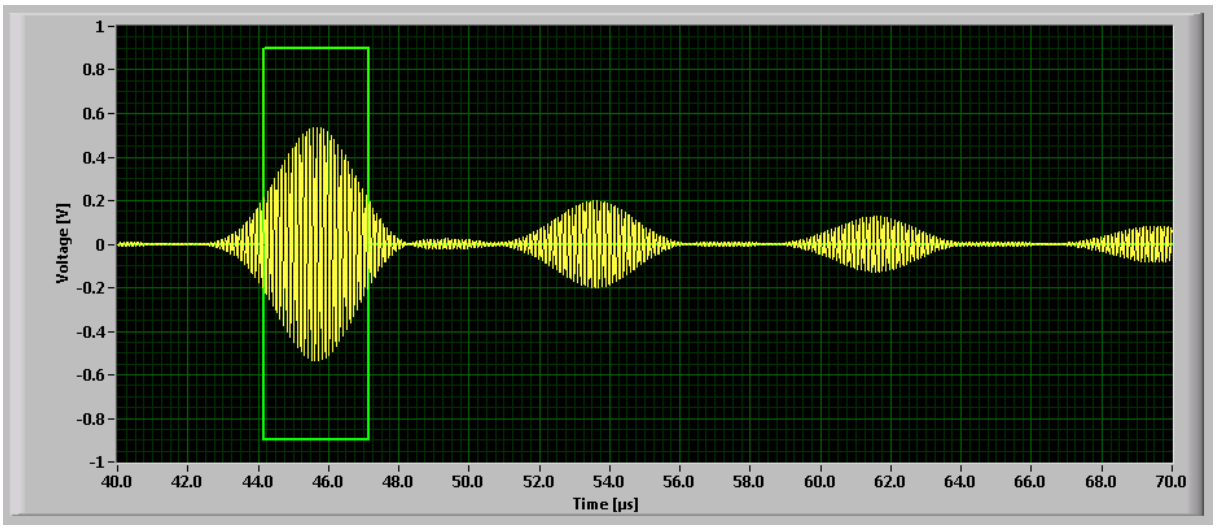

Figure 23. Optimized bulk nonlinear signal from a diffusion-bonded Ti-6Al-4V specimen

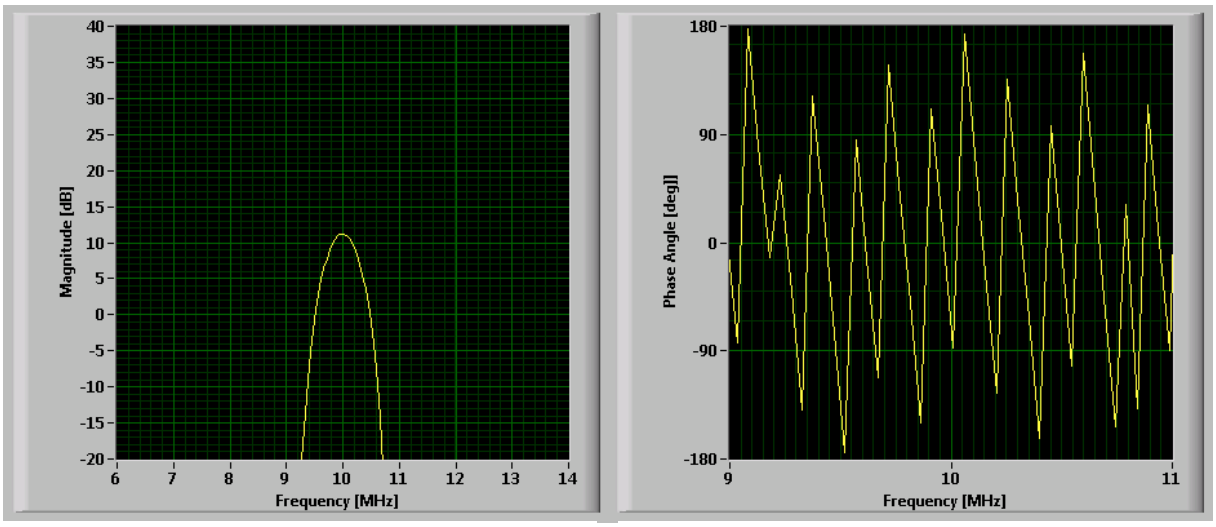

(a) (b)

Figure 24. Frequency spectrum (a) magnitude and (b) phase angle of the gated and windowed nonlinear signal

4.5 AUTOMATED TRANSDUCER ALIGNMENT

With the hardware modification described in section 3.3, the angular and lateral linear movement of the transmitting transducers could be automated under control by the integrated LabVIEW software. The main steps of the adopted optimization process are as follows. One of the transmitting transducers is first rotated within an angular range defined by the user, and several data points of the magnitude of the nonlinear signature are collected. Based on these data points and their angular positions, the corresponding second-order polynomial regression curve is calculated and the angle where the peak occurs is determined. Then the transducer is

automatically rotated to the optimized angular position. The next step is to find the optimized lateral position for the same transducer. Again, the transducer is moved within a predefined distance range, and numerous data points of the magnitude of the nonlinear signature are collected. Another second-order polynomial regression curve is calculated based on these data points, and the optimized lateral position is determined. In this way, the optimized angular and lateral positions of the transmitting transducer are fixed. Then the same process is applied to the other transducer to find its optimized position. After the first iteration, the nonlinear signature still might not be exactly at its peak; therefore, a second or third iteration of this process is conducted with gradually reduced angular and linear ranges until the optimized nonlinear signature is found with satisfactory accuracy. To integrate this optimization process into the main LabVIEW program, a simple subroutine was first developed that rotates the transducer to the angle defined and then acquires the magnitude of the 10-MHz frequency component of the nonlinear signature. A similar program was also developed for the lateral linear stage to move the transducers to a desired lateral position and then acquire the magnitude of the 10-MHz frequency component of the nonlinear signature.

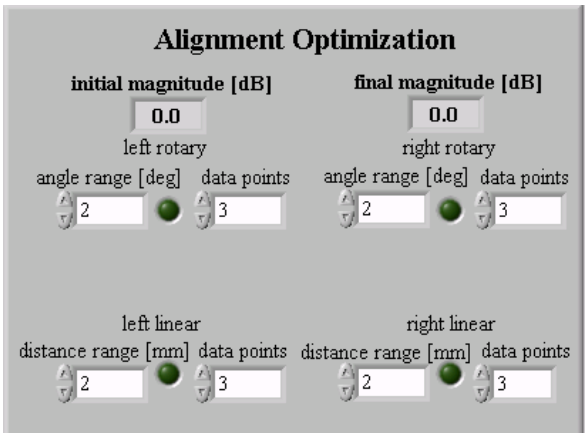

Figure 25. Control panel of the transducer alignment optimization program

The transducer alignment optimization program control panel is shown in figure 25. The first step in the search routine is to choose the angular and linear movement ranges. According to figure 3, the angular range for the main lobe of the bulk analytical approximation is approximately 18° for the refraction wave, which means that the angular range for the incident wave in water is approximately 6°. If the angular range for the transducer exceeds 6° during optimization, then the program will collect data points that are on the side lobe of the bulk analytical approximation curve shown in figure 3. In those cases, using a second-order polynomial regression curve will give the wrong position for the peak, and further iterations cannot help to recover because the search will not be convergent or will converge to the wrong alignment. To prevent such an error, first the system is aligned manually to approximately locate the optimal nonlinear signature to ensure that the initial configuration is relatively close (e.g., within ±2°) to the peak of the main lobe. Then, the operator can select a safe initial angular range of ±2°, which is reduced to ±1° in the second iteration and to ±0.5° in the third iteration. Because misaligning the lateral positions of the transducers does not affect the strength of the nonlinear signature as much as misaligning the angles of the transducers, the lateral linear range can be selected to start at ±1 mm and can be further reduced to ±0.5 mm in subsequent iterations.

5. PRELIMINARY TESTS AND VALIDATION

This report describes the main steps of redesigning and rebuilding of the hardware and software components of the nonlinear ultrasonic imaging system. The ultimate goal of these efforts was to make the nonlinear inspection system more suitable for ultrasonic characterization of diffusion-bonded engine alloys. The next step in this direction was the conduction of preliminary tests on low- to high-quality diffusion-bonded specimens previously tested by various linear and nonlinear inspection methods to test the upgraded nonlinear inspection system. The immediate purpose of these tests was to validate that the SNR, sensitivity, and resolution of the upgraded inspection system were sufficiently improved to use it on high- to very-high-quality diffusion bonds.

5.1 INSPECTION SYSTEM AND MEASUREMENT PROCEDURE VALIDATION

The preliminary validation tests were conducted by reproducing a series of measurements on diffusion-bonded Ti-6Al-4V specimens conducted earlier using the first version of the nonlinear ultrasonic inspection system [8]. The inspection was performed in transmission mode of operation on eight diffusion-bonded Ti-6Al-4V specimens prepared by RRC and a double-thickness intact plate that was used as a reference representing an ideal "perfect" bond. Measurements were made in both optimized bulk configuration and misaligned interface configuration. Interface configuration suppresses the bulk nonlinearity of the surrounding host material, thereby enhancing the contrast to interface imperfections. All the specimens, except the intact reference piece, were diffusion bonded from two 0.5″ thick flat Ti-6Al-4V plates by Vacuum Process Engineering, Inc. (VPE) of Sacramento, California, under contract from RRC. The bonding conditions were selected so that the specimens covered a wide range of bond quality from low through medium to high. The detailed bonding conditions are shown in table 7.

Table 7. Bonding conditions for the first batch of diffusion-bonded Ti-6Al-4V specimens

Sample	#1	#2	#3	#4	#5	#6	#7	#8
Temperature [°C]	695	745	745	745	795	845	915	775
Time [hrs]	2	2	3	2	2	2	2	4
Pressure [psi]	1800	1800	1800	1800	1800	1800	500	1800
Crushing strain [%]	0.3	0.9	1.0	1.1	2.3	3.5	5.5	2.2
CBGG [%]	6.59	32.7	48.0	68.8	73.2	79.3	85.1	86.0

After bonding, destructive tests were performed on the specimens to obtain the metallurgical images of the bond region to establish the diffusion-bond quality. Micrographs of the diffusion-bonded Ti-6Al-4V specimens are shown in figure 8. The listed percentage values represent the measured crushing strain (CS) for each specimen. The bond quality was further assessed by RRC based on a proprietary CBGG measurement method. CBGG represents the proportion of grains that have "grown" across the interface and 100% CBGG indicates a perfect bond. The CBGG value is widely accepted as the best overall metallurgical indicator of diffusion-bond quality.

Nonlinear inspection of these specimens was performed in both bulk and interface configurations using experimental parameters that were previously listed in table 5. The scanning area for the nonlinear inspection was 2″ x 2″, and for each pixel the magnitude of the 10-MHz frequency component of the nonlinear signature was measured. With the newly designed nonlinear imaging system, the nonlinear inspection was repeated on the same specimens with the same bulk and interface configurations described in the paper by Escobar-Ruiz et al. [8]. The nonlinear C-scan images obtained by the upgraded system are shown in figure 26.

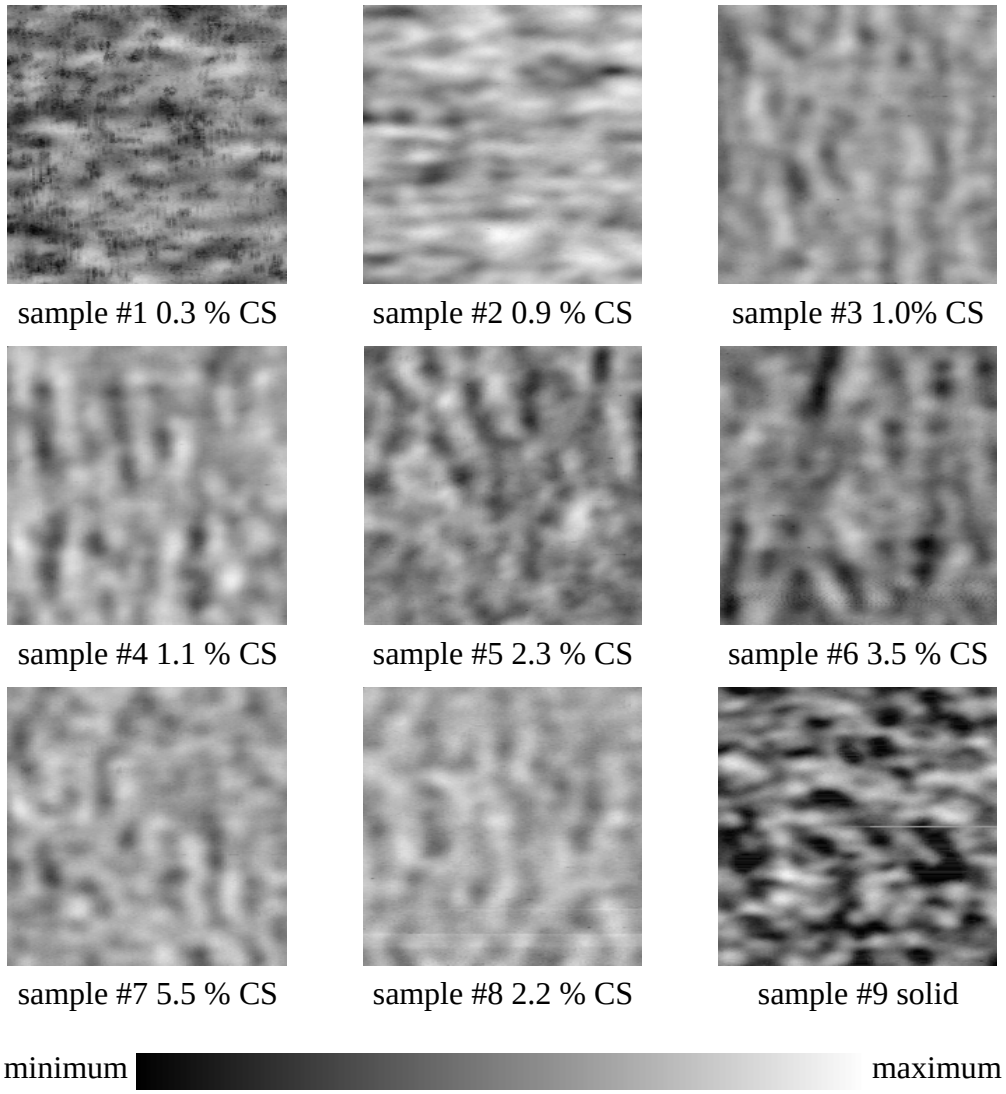

Figure 26. Nonlinear transmission amplitude images of the first batch of diffusion-bonded Ti-6Al-4V specimens in interface configuration (2″ × 2″)

Figure 26 shows that samples #1 and #9 exhibit weaker nonlinear transmitted signatures than the other samples. To quantitatively analyze the detected nonlinear signature of different bond qualities, the acquired magnitude data for every pixel was averaged for each image and the averaged value was used to represent the strength of the nonlinear signature for that particular specimen. The comparison between the results from the paper by Escobar-Ruiz et al. [8] and

those obtained by the upgraded nonlinear imaging system is shown in figure 27. Figure 27(a) indicates that in the previous study, which used frequency filtering to suppress the spurious nonlinearity caused by second harmonics, the interface configuration helped suppress the bulk nonlinearity by less than 3 dB. The results obtained with the upgraded inspection system using the same interface and bulk alignments listed in table 5 indicate that bulk nonlinearity suppression doubled to approximately 6 dB. In conclusion, the results obtained by the enhanced nonlinear imaging system not only reproduced those obtained earlier, but the suppression of bulk nonlinearity significantly improved with using the interface configuration.

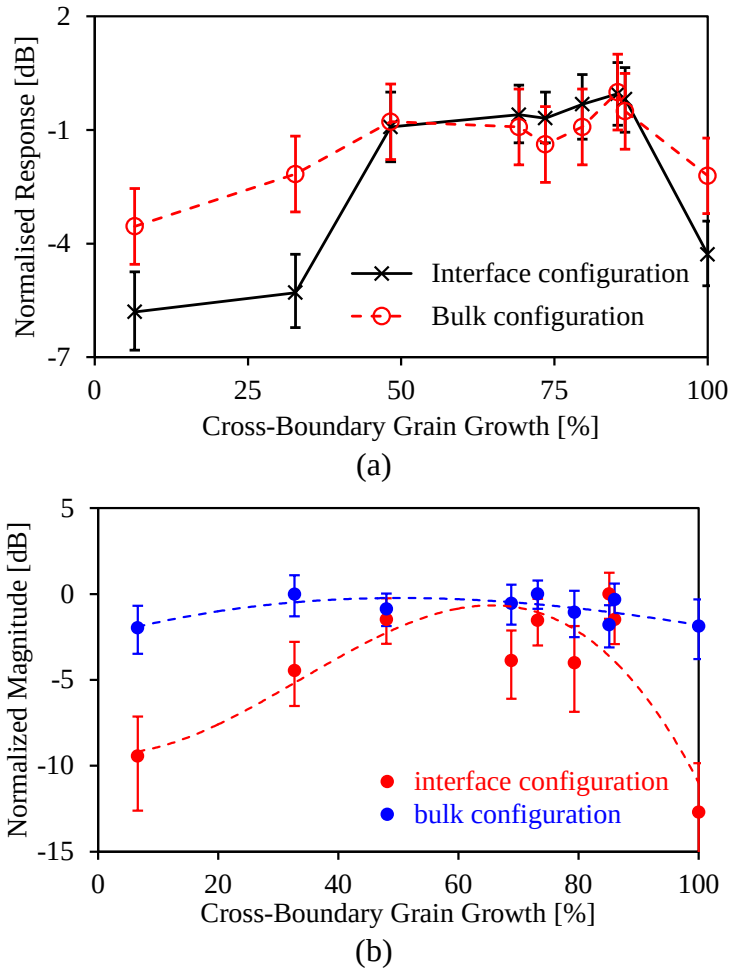

Figure 27. Nonlinear signatures of the first batch of diffusion-bonded Ti-6Al-4V specimens in transmission mode of operation (a) with frequency filtering [8] and (b) with four-way polarity flipping using the upgraded nonlinear imaging system

6. MICROSTRUCTURAL EXAMINATION OF DIFFUSION-BONDED SPECIMENS

For the purposes of assessing the feasibility of diffusion-bond characterization using nonlinear reflection measurements from the bond interface, in addition to the first batch of Ti-6Al-4V diffusion-bonded specimens made earlier, VPE and RRC optimized the diffusion-bonding process and manufactured a second batch of six diffusion-bonded Ti-6Al-4V specimens

representing the highest bond quality technologically possible. The specimens in the second batch were made under the optimized bonding conditions listed in table 8. VPE and RRC also prepared eight IN718 diffusion-bonded specimens to facilitate the testing of the nonlinear ultrasonic inspection technique in a different engine alloy. The IN718 specimens were made under the bonding conditions listed in table 9. The technological parameters listed in tables 8 and 9 were selected by RRC and VPE following an initial feasibility study conducted on small coupons of the same materials. Before bonding, both the Ti-6Al-4V and IN718 plates were 0.5″ thick and in their intact annealed states of HRC 36 and HRC 24 Rockwell C hardness, respectively. All parts were surface ground parallel to 0.001″ with average 13Ra surface finish (13 μin average roughness or 0.35 μm rms). The second batch of IN718 specimens were nickel sulfamate plated with 200–250 μin (5.0-6.3 μm) thickness. Such interlayers are routinely used in solid-state diffusion bonding when reduction of bonding temperature, pressure, or time is required. This is because interlayers used in diffusion bonding are made of soft metals so that localized plastic flow can take place easily and because localized diffusion is enhanced by the presence of interlayers at the interface. As a result, bonding can be carried out at lower temperatures or pressures compared to bonding without interlayers [23].

Table 8. Bonding conditions for the second batch of diffusion-bonded Ti-6Al-4V specimens

Sample	T1T2	T3T4	T5T6	T7T8	T9T10	T11T12
Temperature [°C]	845	875	905	915	935	945
Time [hrs]	2	2	2	2	2	2
Pressure [psi]	1800	1000	750	750	350	200
Crushing strain [%]	5.5	4.2	4.6	5.4	7.3	5.5

Table 9. Bonding conditions for diffusion-bonded IN718 specimens

Sample	IN1-2	IN3-4	IN5-6	IN7-8	IN9-10	IN11-12	IN13-14	IN15-16
Temperature [°C]	1125	1125	1143	1173	1173	1173	995	995
Time [hrs]	3	3	3	3	3	5	5	5
Pressure [psi]	1000	1500	1500	1500	1500	2000	2000	3500
Crushing strain [%]	0.08	0.65	1.00	2.50	1.70	3.60	1.50	3.00

6.1 DIFFUSION-BONDED TI-6AL-4V SPECIMENS

Microstructural evaluation of diffusion-bonded Ti-6Al-4V specimens included both destructive metallurgical and nondestructive ultrasonic and eddy current measurements. The latter was prompted by the observation that when performing nonlinear inspection on the second batch of Ti-6Al-4V diffusion-bonded specimens using the same alignment configuration as used in the previous tests on the first batch, the measured nonlinearity exhibited a distinct anisotropic behavior. The different nonlinear signatures measured in two orthogonal directions on the second batch of Ti-6Al-4V specimens is shown in figure 28. These results indicate that the average nonlinear signature dropped approximately 3 dB when the specimen was rotated by 90°. One possible explanation for this phenomenon is that the texture of the new Ti-6Al-4V specimens was unusually strong; therefore, the ultrasonic properties varied significantly between two

orthogonal directions. To validate this assumption, ultrasonic shear wave birefringence measurements were conducted in two orthogonal directions to characterize the degree of anisotropy. These Ti-6Al-4V specimens were diffusion bonded in a way that the rolling direction of the top plate was orthogonal to that of the bottom plate; therefore, the shear wave birefringence could only be measured through half the thickness of the specimen (i.e., through a single plate). To measure the shear wave velocity in the 0.5″-thick single plate, a 5-MHz, 0.5″-diameter normal incidence contact shear wave transducer was placed close to the edges of the specimens where the bonding was not very good and the linear reflection from the interface could be detected. Once the linear reflection from the diffusion-bonded interface was detected, the transducer was rotated to find the directions where wave propagation was the fastest and the slowest. The biggest time difference between the arrival times of the linear reflected signal was recorded and based on this value the relative shear wave birefringence was calculated. For each plate, the measurement was repeated at five different locations to increase the measurement accuracy.

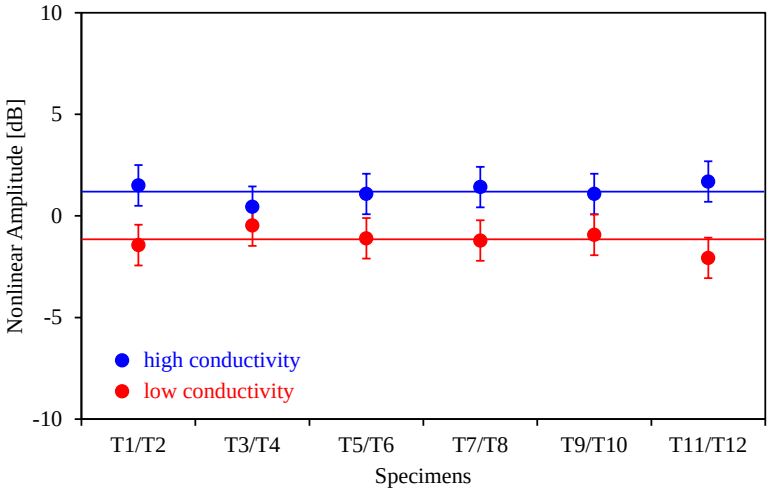

Figure 28. Nonlinear signature measured in orthogonal directions in the second batch of diffusion-bonded Ti-6Al-4V specimens

Shear wave birefringence measurements were performed on both the first and second batches of Ti-6Al-4V diffusion-bonded specimens. The results shown in figure 29(a) indicate that the second batch of Ti-6Al-4V specimens exhibited a much higher degree of anisotropy than the first batch of specimens. The average relative shear wave difference measured in the first batch of specimens was only 1.7%, whereas in the second batch of specimens the average relative shear wave difference was as high as 5.6%. To further validate this finding, the relative electric conductivity difference between two orthogonal principal directions was also measured by using a directional eddy current probe. Electrical conductivity anisotropy is an independent indicator of texture in titanium alloys that preferentially crystallize in hexagonal crystallographic symmetry and, therefore, exhibit strong electric anisotropy in a textured state of the material. The results of the electric conductivity measurements are shown in figure 29(b). The relative conductivity difference measured in the second batch of specimens is almost three times higher than that measured in the first batch of specimens on average. The presence of both acoustic and electric

anisotropy confirms the previous assumption that the second batch of Ti-6Al-4V diffusion-bonded specimens was highly textured.

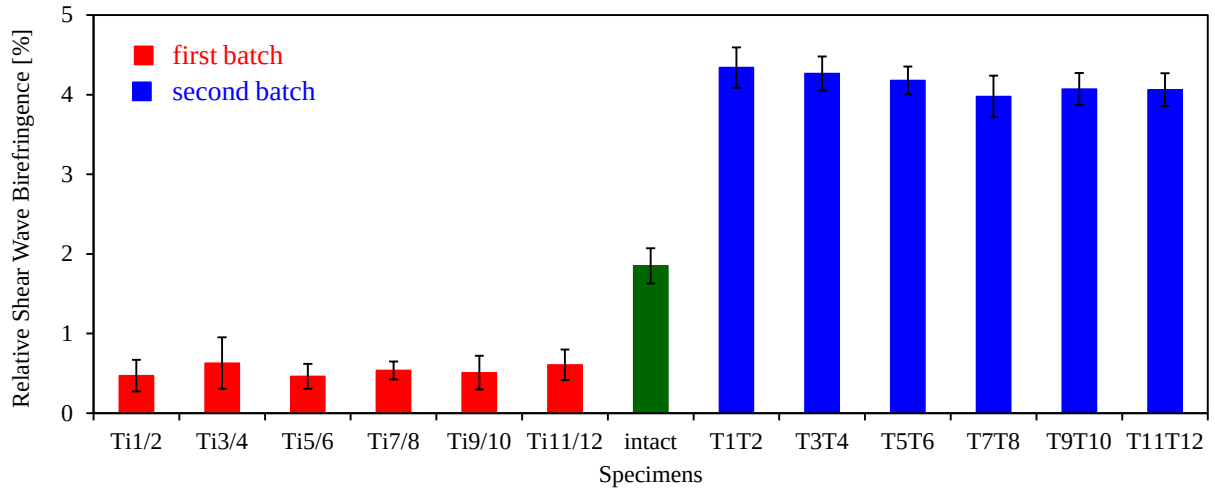

(a)

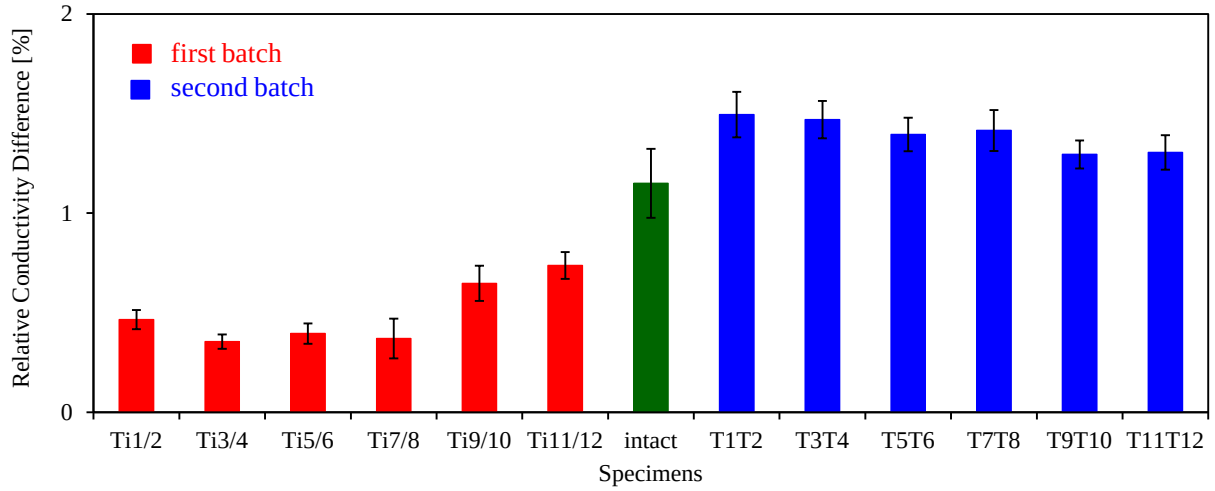

(b)

Figure 29. Relative (a) shear wave velocity difference and (b) electric conductivity difference measured in diffusion-bonded Ti-6Al-4V specimens

Figure 28 shows that to perform reliable nonlinear inspection, the non-collinear shear wave mixing measurement has to be taken in the same direction for all the specimens. To compare nonlinear measurements taken from diffusion-bonded Ti-6Al-4V specimens of significantly different anisotropic texture, it is necessary to determine the principal directions of texture, repeat the measurements in both directions, and average the measured values.

The micrographs of the microstructures of the second batch of diffusion-bonded Ti-6Al-4V specimens were also taken by VPE. The small samples prepared for metallurgic examination were cut from the specimens with the cutting plane vertical to the diffusion-bonded interfaces. Examples of these micrographs are shown in figure 30. The images revealed that all six

specimens exhibited perfect diffusion bonds with no perceivable lack of bond in the metallurgical sections.

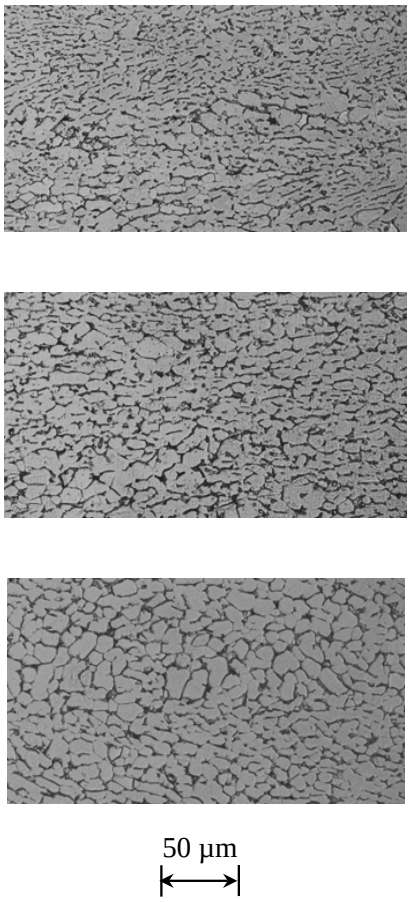

Figure 30. Examples of optical micrographs taken from the second batch of diffusion-bonded Ti-6Al-4V specimens at 500× magnification

6.2 DIFFUSION-BONDED IN718 SPECIMENS

Eight diffusion-bonded IN718 specimens were prepared for nonlinear inspection. The first batch of six specimens did not yield any useful data because they all exhibited excessively high ultrasonic attenuation indicating that very substantial grain coarsening occurred during diffusion bonding. To further investigate this effect, linear ultrasonic attenuation measurements were conducted on these specimens that indicated that no ultrasonic transmission was possible in the 5–10-MHz frequency range of interest. To perform the attenuation measurement, an intact IN718 specimen with the same thickness as the diffusion-bonded ones was used as the reference piece. A contact longitudinal transducer with a center frequency of 10 MHz and 0.25″ diameter was used to detect the back wall echo in the IN718 specimens. For each specimen, the frequency spectrum of the first back wall reflection was recorded and compared to the spectrum detected from the reference piece. Figure 31 shows the results for this attenuation measurement. It is obvious from these results that all six IN718 diffusion-bonded specimens exhibited excessively

high ultrasonic attenuation that exceeded 100 dB at 10 MHz (i.e., at the center frequency of the sought nonlinear mixed signal).

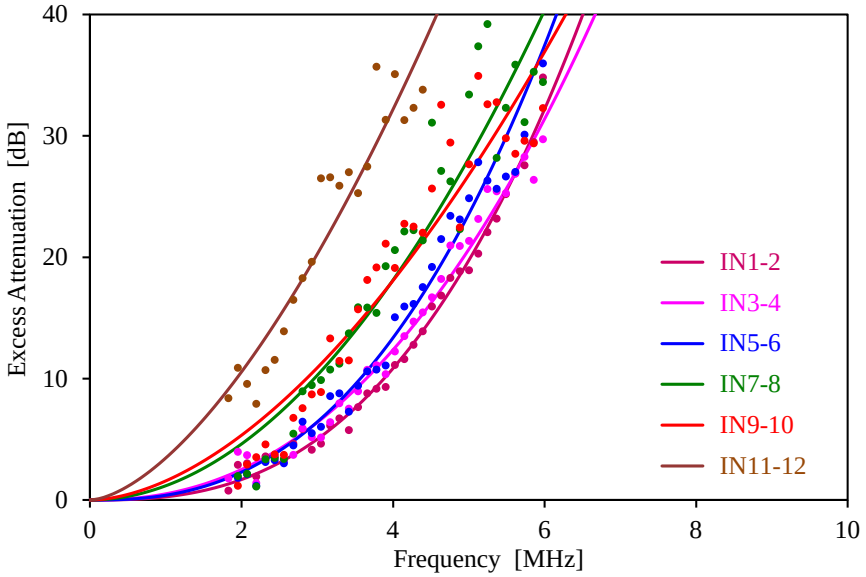

Figure 31. Ultrasonic attenuation measured in the first batch of diffusion-bonded IN718 specimens

The most likely explanation for such excessively high attenuation at 10 MHz is that the grain size has significantly increased during bonding. Metallurgical micrographs of the intact and thermally exposed specimens were prepared and examined. The micrographs of the original IN718 plate and the diffusion-bonded IN718 specimens are shown in figures 32 and 33, respectively. These images show that the original grain size in the intact IN718 material is approximately 40–80 μm, whereas after diffusion bonding the grain size has increased to an average of 200–400 μm. The reason for this dramatic grain coarsening is that the temperature used during bonding was above the gamma prime and gamma double prime solvus temperatures of IN718, which are between 1000°C and 1050°C, and once the delta phase went into solution, there was nothing to prevent grain growth. The large grain size significantly attenuates the high-frequency components of the ultrasonic wave, and as a result, the first batch of diffusion-bonded IN718 specimens could not be inspected even with the upgraded nonlinear imaging system.

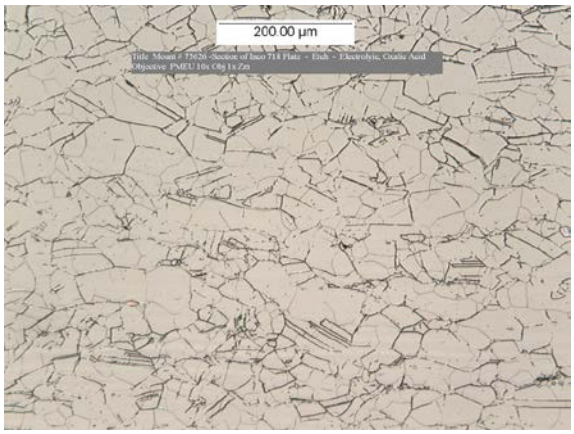

Figure 32. Micrograph of the original IN718 plate used for the diffusion-bonded specimens

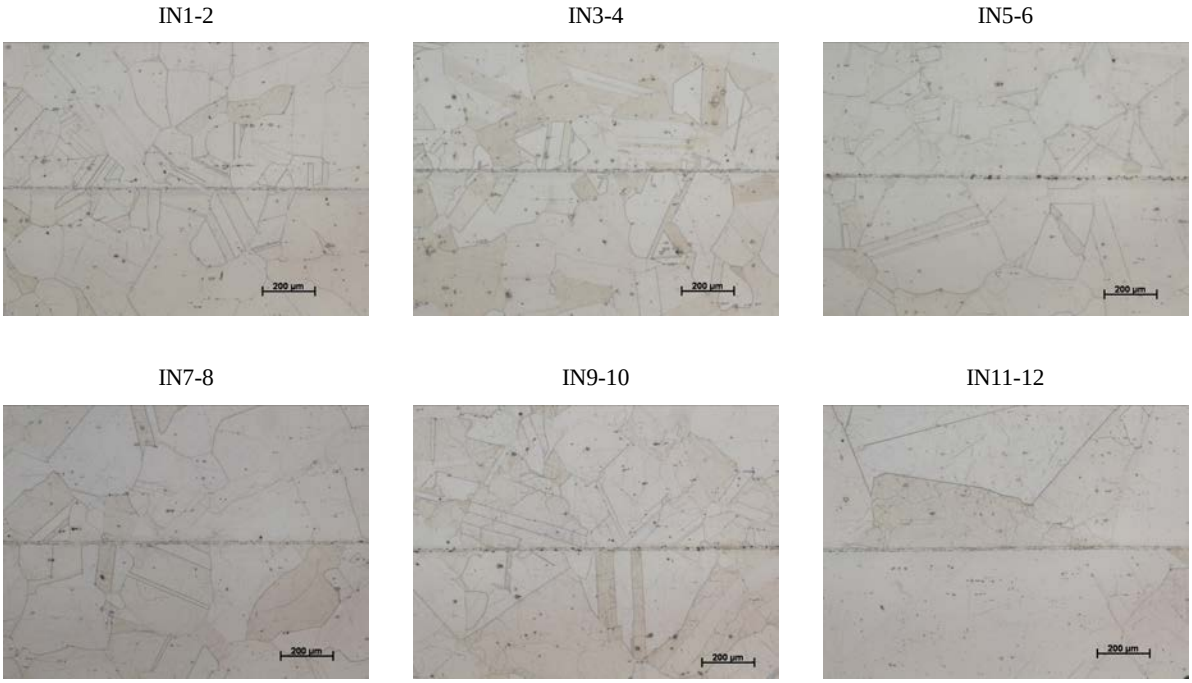

Figure 33. Micrographs of the first batch of diffusion-bonded IN718 specimens

A second batch of two IN718 diffusion-bonded specimens was made with a bonding temperature below the δ solvus temperature to prevent grain growth; however, to reduce the bonding temperature, the bonding pressure had to be greatly increased to ensure high bonding quality. In addition, a 40-µm-thick Nickel foil was placed between the two parts to facilitate diffusion bonding. Unfortunately, the applied very-high crushing pressure caused significant tangential plastic flow which, in turn, accelerated grain growth despite the lower temperature. The results of the attenuation measurement and the corresponding micrographs are shown in figures 34 and 35, respectively. Though the bonding temperature was lowered, specimen IN15-16 still exhibited approximately 27 dB attenuation at 10 MHz and its grain size increased to 100 ~ 200 µm. Only specimen IN13-14 could be tested successfully by the nonlinear imaging system because its attenuation at 10 MHz was only approximately 10 dB with grain size between 50 ~ 100 µm.

However, though the optimized bulk nonlinear signature could be detected from IN13-14, such a high attenuation made it difficult to find the weak nonlinear reflection signal from the diffusion-bonded interface, and increased averaging was needed to obtain acceptable SNR.

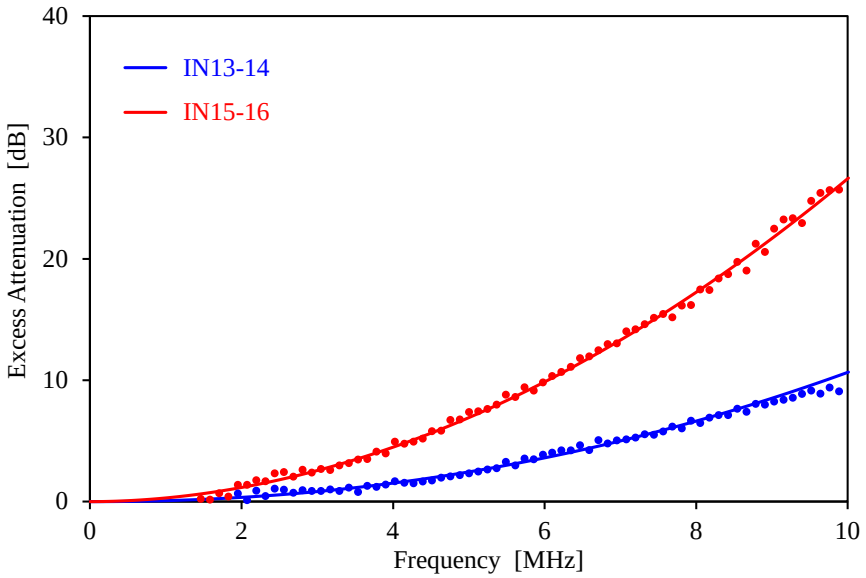

Figure 34. Ultrasonic attenuation measured in the second batch of diffusion-bonded IN718 specimens

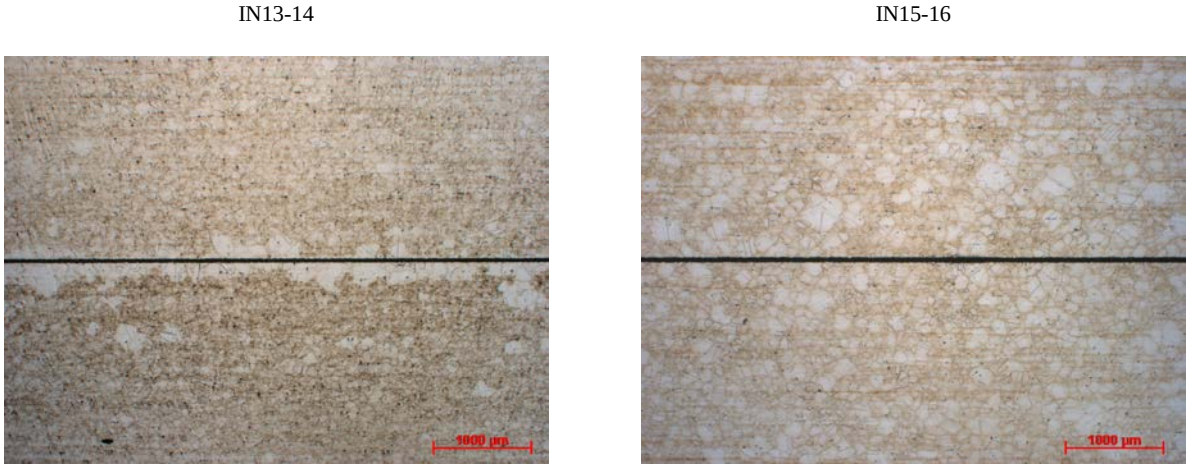

Figure 35. Micrographs of the second batch of IN718 diffusion-bonded specimens (the black line is the remainder of the nickel sulfamate coating used to facilitate diffusion bonding)

7. NONDESTRUCTIVE TESTING

After the necessary preliminary tests performed on both Ti-6Al-4V and IN718 diffusion-bonded specimens, it is clear that the second batch of Ti-6Al-4V specimens all have the expected very-high bond quality that places them in the range between the best bond quality of the first

batch of specimens and the intact reference specimen. Though metallographic inspections showed no detectable lack of bond (i.e., the CBGG values of the second batch of Ti-6Al-4V specimens are all nominally 100 %), their bond qualities should still vary from each other because they were made under systematically changing processing parameters (see table 8). It is possible that further investigation could have distinguished the CBGG values of the specimens in the second batch of diffusion-bonded Ti-6Al-4V specimens by cutting and inspecting numerous slices from each specimen, but so far it is certain that all the new Ti-6Al-4V specimens have less than 5 % lack of bond. Unfortunately, with one exception, all the diffusion-bonded IN718 specimens exhibited gross grain coarsening during bonding and, accordingly, very high ultrasonic attenuation at 10-MHz inspection frequency. Therefore, only one bonded specimens (IN13-14) could be inspected by the upgraded nonlinear imaging system.

7.1 LINEAR ULTRASONIC SCANS

Neither linear nor nonlinear inspection alone can sufficiently distinguish the full range of bond quality from worst to perfect; therefore, in addition to the nonlinear inspection, linear ultrasonic scans were also obtained. An immersion transducer of 10-MHz center frequency, 0.5″ diameter, and 3″ focal length was used for linear inspection. To focus at the interface, the transducer was placed 1.5″ above the top surface of the specimens. The gate for the sought linear reflection signal was set halfway between the 1st and 2nd back wall reflections and necessarily included not only the reflection from the interface but also some grain backscattering from the surrounding host material. The obtained linear images of the second batch of diffusion-bonded Ti-6Al-4V specimens are shown in figure 36. These linear images do not reveal any perceivable diffusion-bonded imperfections. The apparent horizontal lines on the C-scan of specimen T1T2 were caused by surface scratches. The dark squares in the center at the bottom of the images are caused by the missing pieces removed by electric discharge machining for metallurgical inspection.

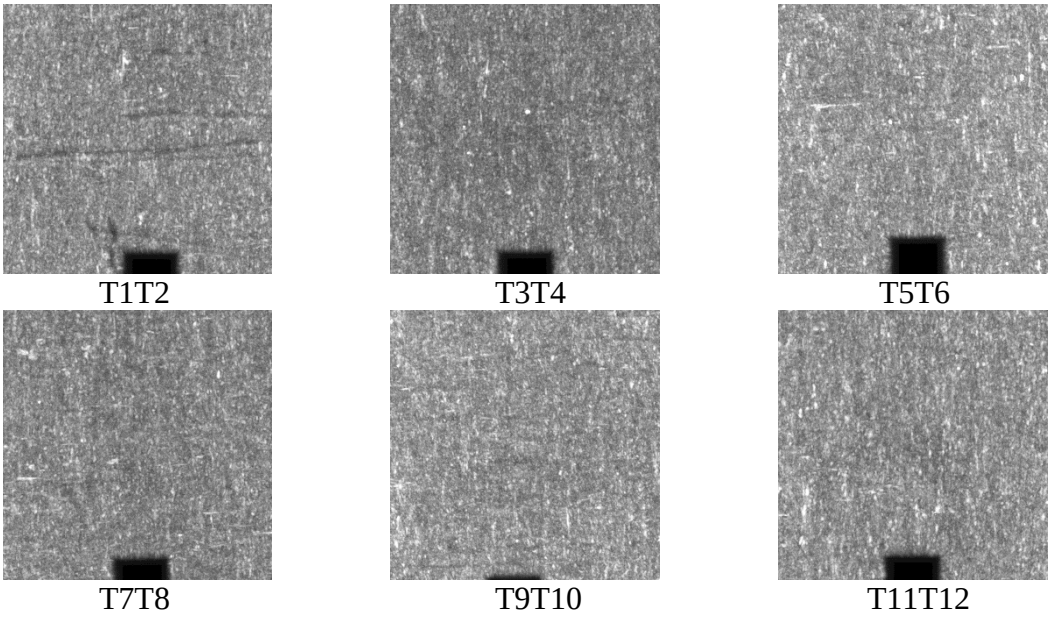

Figure 36. Linear C-scan images of the second batch of diffusion-bonded Ti-6Al-4V specimens taken at 10 MHz (100 mm × 100 mm)

First, linear ultrasonic inspection of the second batch of diffusion-bonded IN718 was conducted with the same transducer of 10-MHz center frequency. The results revealed traces of a highly scattering area and a few possible point defects in specimen IN13-14 made under lower crushing pressure. Therefore the inspection was repeated with a different transducer of 5-MHz center frequency, 0.25″ diameter, and 2″ focal length. To focus at the interface, the transducer was placed approximately 0.5″ above the top surface of the specimen and the signal gate was set to be at the center between the 1st and 2nd back wall reflections. The linear C-scan images acquired from the second batch of diffusion-bonded IN718 specimens at 5 MHz are shown in figure 37. These linear images show that specimen IN13-14 had an area and a few spots where the imperfections of the bond can be detected by conventional linear inspection. Therefore, this specimen is promising for nonlinear inspection because it has the transition area from good bond quality to bad bond quality, which is expected to exhibit high nonlinearity. Specimen IN15-16 did not show any imperfections by low-frequency linear inspection. However, the ultrasonic attenuation in this specimen was so high that neither linear nor nonlinear inspection was really possible and the detected linear contrast is mainly incoherent electric noise that could be suppressed with excessive averaging. As a result, from the eight diffusion-bonded IN718 specimens, only IN13-14 will be inspected by the nonlinear imaging system.

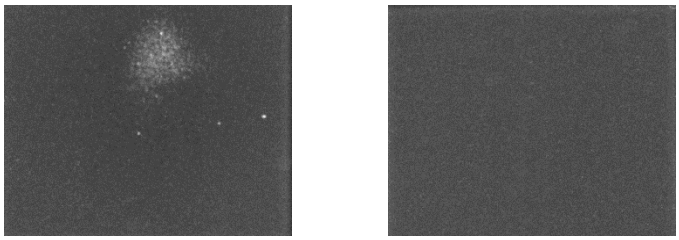

(a) IN13-14 (b) IN15-16

Figure 37. Linear C-scan images of the second batch of diffusion-bonded IN718 specimens taken at 5 MHz (100 mm × 80 mm)

7.2 NONLINEAR ULTRASONIC SCANS

To make the best possible comparison, both batches of diffusion-bonded Ti-6Al-4V specimens were inspected by the upgraded nonlinear ultrasonic inspection system using primary shear wave frequencies of f_1 = 4.5 MHz and f_2 = 5.5 MHz. The temporal length and decay parameter of both driving signals were t_p = 3 μs and α = 3, respectively. The interface configuration listed in table 5 was used for transducer alignment. Transmission mode images were obtained earlier from the first batch of diffusion-bonded Ti-6Al-4V specimens using the upgraded nonlinear inspection system (see figure 26). In the next step, nonlinear reflection images were taken from these diffusion-bonded interfaces, and the obtained amplitude and phase angle images are shown in figures 38 and 39, respectively. The listed percentage values represent the measured CS for each specimen. The amplitude images in figure 38 show a basically random spatial distribution of the nonlinear reflection, but it is clear that both the lowest and highest bond qualities exhibit reduced nonlinearity as expected. In addition, sample #2, which has the second lowest bond quality, exhibits the weakest nonlinear reflection signature among all the specimens. Like the amplitude images, the phase images in figure 39 also show a basically random spatial distribution of the nonlinear reflection, except for the lowest bond quality that exhibits a fairly uniform phase with limited random variation. This behavior indicates that a significant fraction of the forward-propagating bulk nonlinear signal got reflected backward; therefore, in the case of this low-quality specimen, nonlinear reflection from the interface includes a strong linear reflection of the otherwise forward-propagating bulk nonlinear signal.

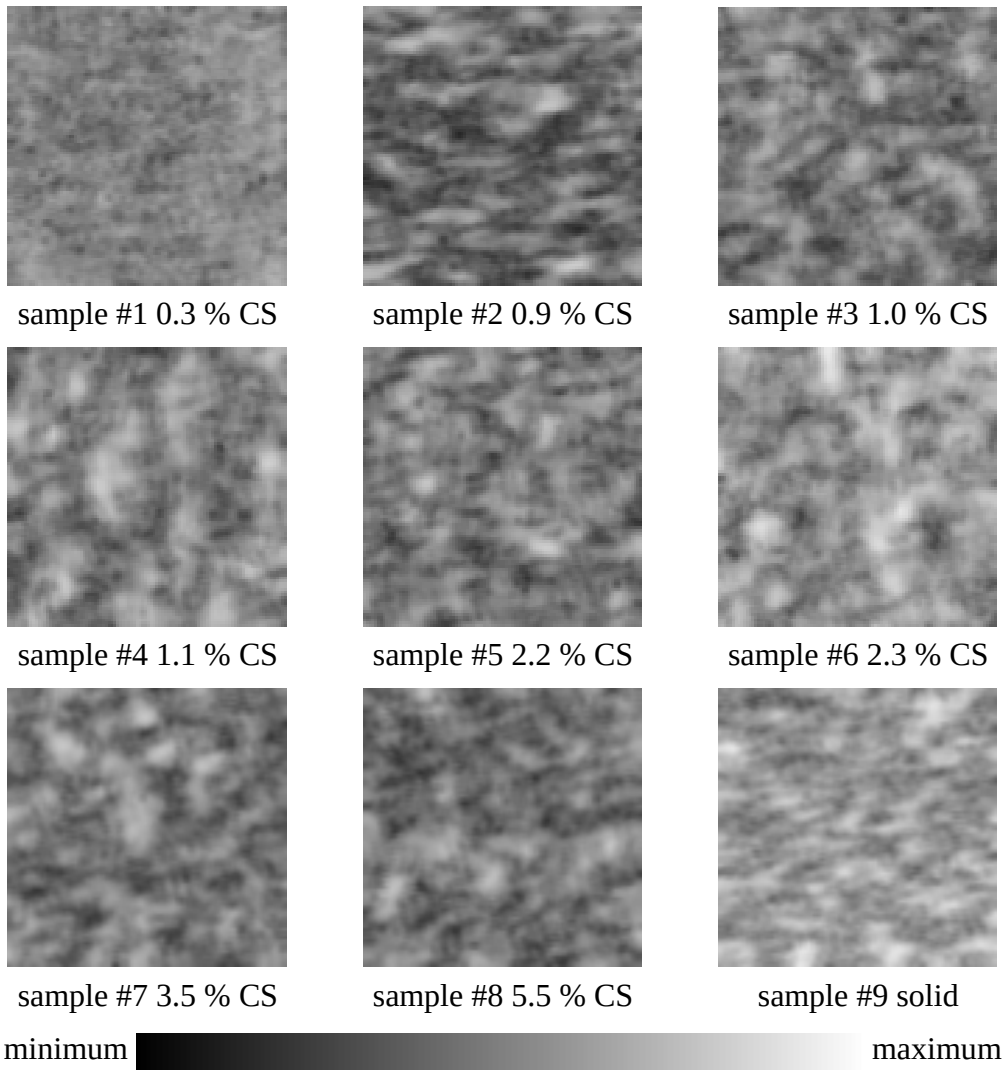

Figure 38. Nonlinear reflection mode amplitude images of the first batch of diffusion-bonded Ti-6Al-4V specimens taken in interface configuration (2″ × 2″)

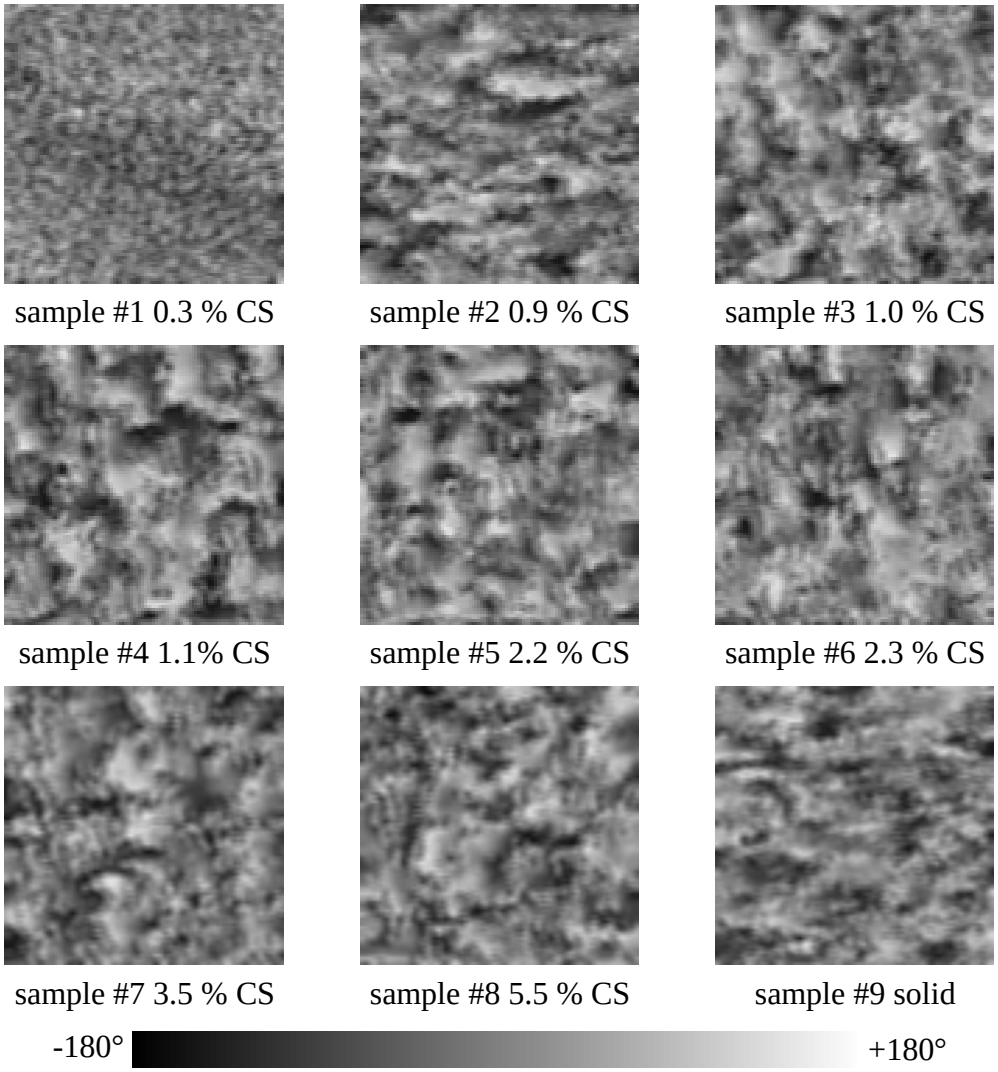

Figure 39. Nonlinear reflection mode phase angle images of the first batch of diffusion-bonded Ti-6Al-4V specimens taken in interface configuration (2″ × 2″)

Similar nonlinear inspection was also performed on the second batch of six Ti-6Al-4V specimens. As a first step, transmission mode nonlinear images were obtained. The results shown in figure 40 indicate that the nonlinear signature is relatively weak and exhibits a fairly uniform signature except some elongated features that are related to the high macroscopic texture in these specimens. Both the low level and uniform distribution of the nonlinear signature exhibited by these specimens in transmission mode of operation indicate that the interface contribution to the detected nonlinear signal is very weak and the nonlinear transmission is dominated by the bulk contribution. Based on these observations, it is not likely that these high-quality diffusion bonds can be distinguished using transmission mode nonlinear inspection. Better sensitivity can be achieved using the unique reflection mode of operation offered by the upgraded nonlinear inspection system. Figures 41 and 42 show the amplitude and phase angle images, respectively, obtained using nonlinear reflection measurements from the second batch of diffusion-bonded Ti-6Al-4V specimens.

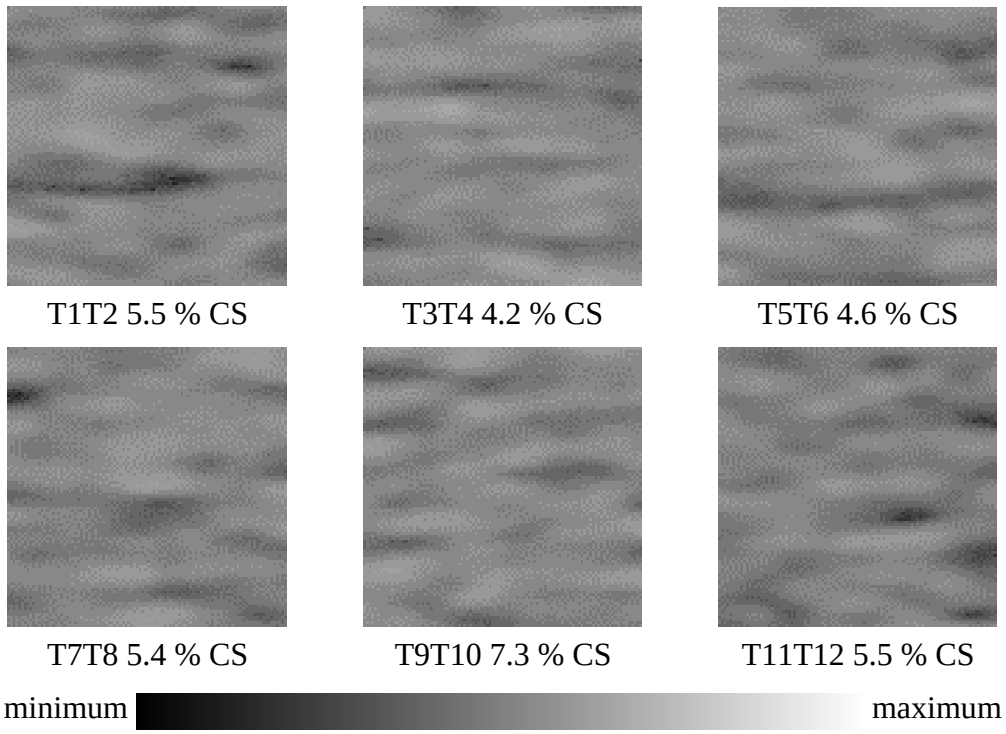

Figure 40. Nonlinear transmission mode amplitude images of the second batch of diffusion-bonded Ti-6Al-4V specimens taken in interface configuration (1″ × 1″)

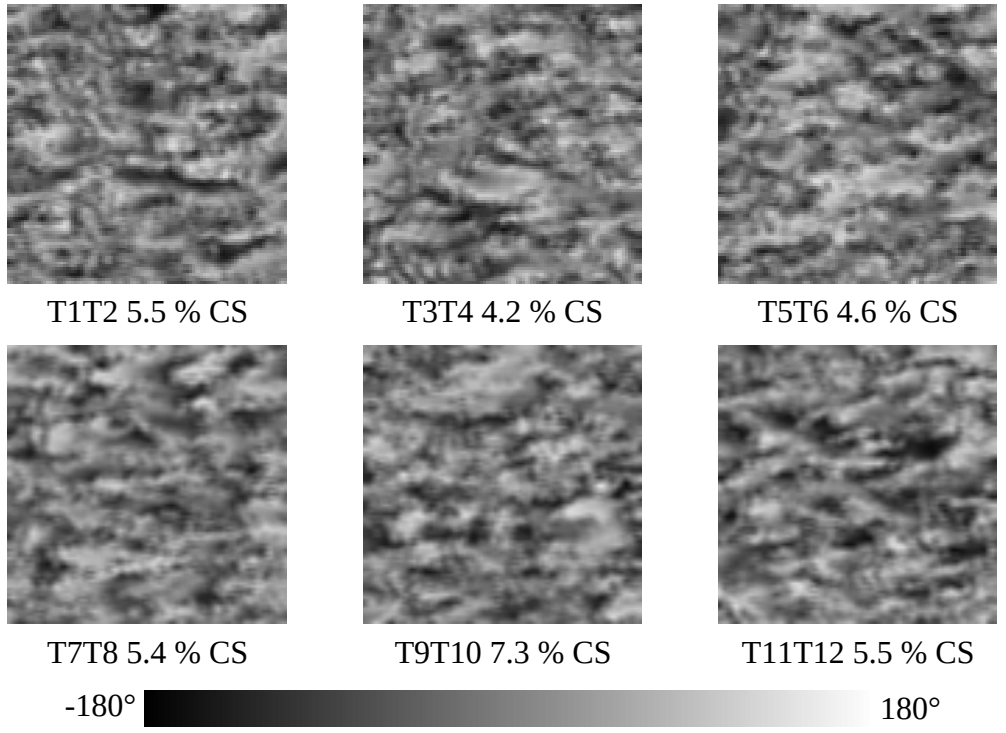

Figure 41. Nonlinear reflection mode amplitude images of the second batch of diffusion-bonded Ti-6Al-4V specimens taken in interface configuration (2″ × 2″)

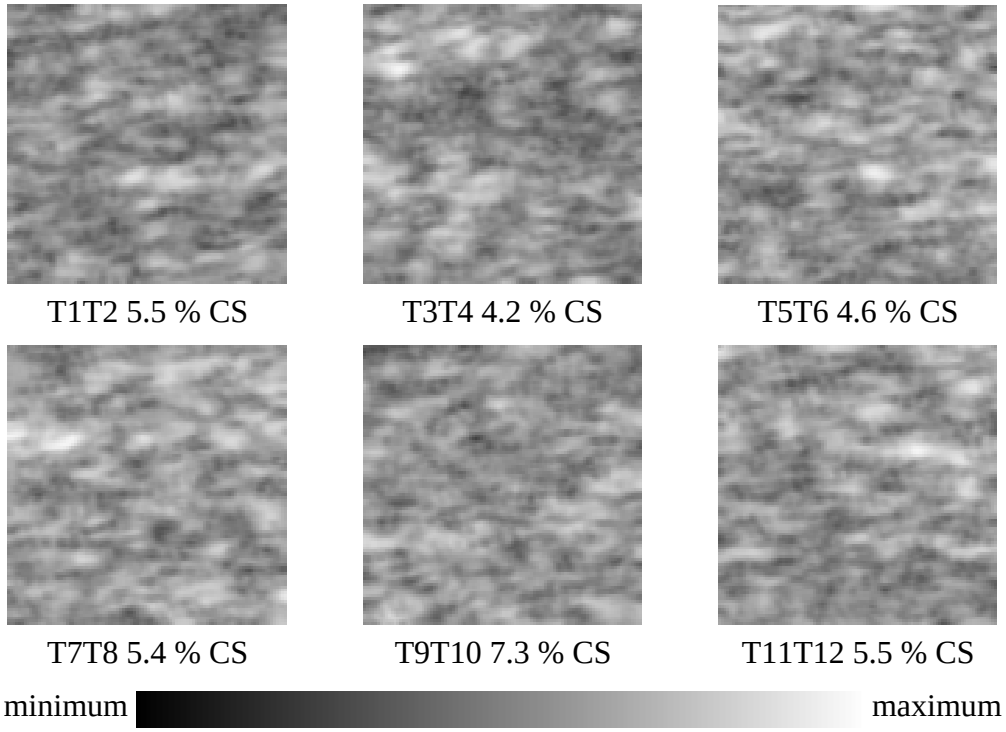

Figure 42. Nonlinear reflection mode phase angle images of the second batch of diffusion-bonded Ti-6Al-4V specimens taken in interface configuration (2″ × 2″)

The nonlinear amplitude and phase images obtained from two batches of Ti-6Al-4V diffusion-bonded specimens will be quantitatively analyzed in section 8 to further investigate how nonlinear inspection based on nonlinear reflection from the interface helps better assess high-quality diffusion bonds. As for the diffusion-bonded IN718 specimens, only IN13-14 could be tested by nonlinear inspection. Because of the very-high ultrasonic attenuation, the detected nonlinear reflection was very weak. To show that the measured signals are still reproducible, figure 43 shows two images obtained in two separate scans. The spot of increased grain scattering shown in the linear image in figure 37(a) is not perceivable; therefore, it was likely produced by excess local grain coarsening rather than interface imperfection.

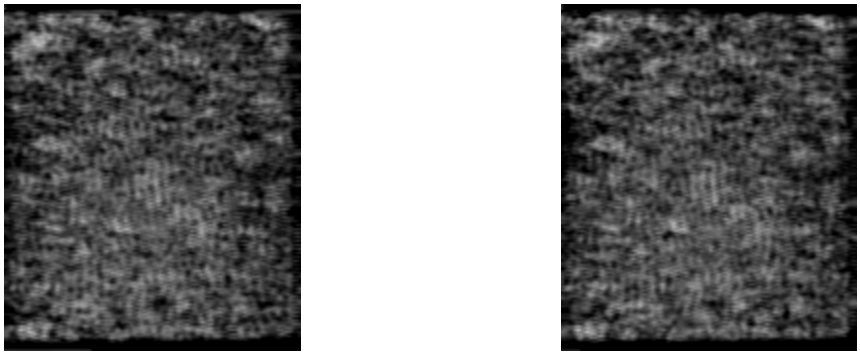

Figure 43. Nonlinear reflection amplitude images from the (a) first and (b) second scans of diffusion-bonded IN718 specimen IN13-14 (3″ × 3.5″)

8. QUANTITATIVE EVALUATION OF LINEAR AND NONLINEAR ULTRASONIC IMAGES

The amplitude and phase images of the nonlinear reflection signature collected by the upgraded non-collinear shear wave mixing inspection system from the nine samples in the first batch and six samples of the second batch of diffusion-bonded Ti-6Al-4V specimens were presented in the preceding section along with that of the single diffusion-bonded IN718 specimen IN13-14 that was found suitable for nonlinear inspection. In this section, a detailed quantitative analysis of those nonlinear C-scan images will be presented.

8.1 DATA ASSESSMENT AND CORRELATION ANALYSIS

Each pixel in the recorded nonlinear amplitude and phase-angle C-scans represent one data point that is an average of multiple measurements that fell in that particular bin during scanning. The number of averaged values depends on the scanning speed and the refreshing rate of the digital data processor, but preferentially it is at least two or three. Therefore, each C-scan contains the same number of data points as the number of image pixels. Based on all these data points, an overall average value and standard deviation were calculated to quantitatively characterize the strength and variance of the nonlinear signature in the entire frame recorded for a given specimen. First, the average amplitude for each specimen was calculated based on the nonlinear transmission amplitude images of the first and second batches of diffusion-bonded Ti-6Al-4V specimens previously shown in figures 26 and 40. The comparison between the first and second batches of Ti-6Al-4V diffusion-bonded specimens is shown in figure 44. For easier comparison, the frame averages were normalized to the highest average amplitude found among the 15 specimens.

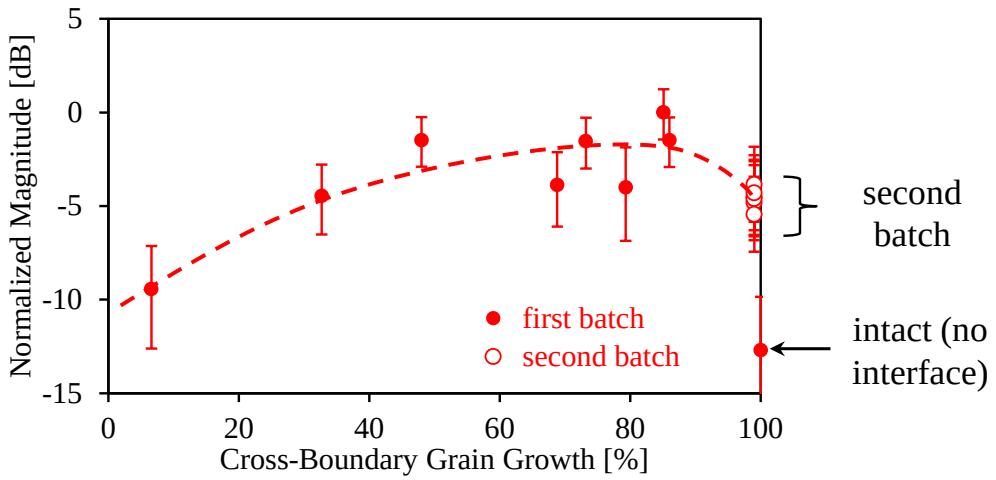

Figure 44. Combined nonlinear amplitude results obtained with transmission measurements in interface configuration from both batches of diffusion-bonded Ti-6Al-4V specimens

It was mentioned in section 6.1 that despite the fact that the bonding conditions for the second batch of very-high quality diffusion-bonded Ti-6Al-4V specimens were different, they all exhibited apparently perfect bonds and registered at 100 % CBGG value. Because metallurgical

analysis was limited to one slice from each specimen, they are all plotted as having maximum CBGG just below the ideal reference specimen cut from a single double-thickness plate. Note that figure 40 also indicated that there was no perceivable difference between the nonlinearity detected in transmission mode even in the misaligned interface configuration that helps to suppress the competing bulk nonlinearity of the surrounding host material. The most important conclusion that can be drawn from the results shown in figure 44 is that all six high-quality diffusion-bonded Ti-6Al-4V specimens in the second batch exhibit weak nonlinearity that falls between that of the most nonlinear specimens of the first batch and the "perfect" reference specimen.

The question arises whether the measured nonlinearity in the high-quality specimens that belong to the second batch show any correlation with any of the bonding parameters provided by the manufacturer, VPE. The average nonlinear signatures of the second batch of diffusion-bonded Ti-6Al-4V specimens are plotted against their respective bonding temperature and CS in figure 45. These results also show that non-collinear shear wave measurements conducted in transmission mode of operation yield no perceivable difference in nonlinearity levels of these high-quality diffusion bonds.

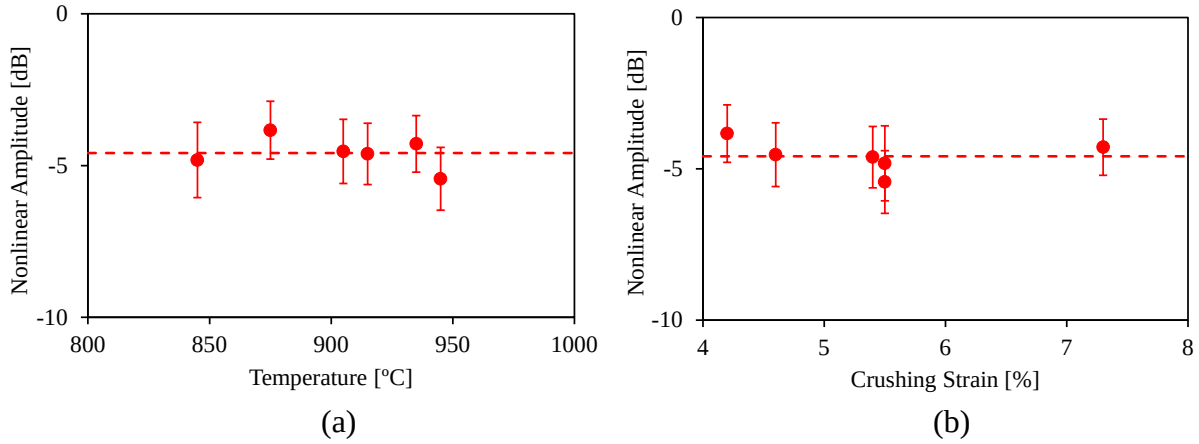

Figure 45. Nonlinear amplitudes of the second batch of diffusion-bonded Ti-6Al-4V specimens detected in transmission mode with interface configuration versus (a) bonding temperature and (b) CS during bonding

Fortunately, the significantly increased detection sensitivity of the upgraded nonlinear inspection system also allows the measurement of nonlinear signatures in reflection mode of operation. Therefore, the nonlinear reflection C-scans obtained from the second batch of diffusion-bonded Ti-6Al-4V specimens were further analyzed to determine whether they are easier for distinguishing between high-quality bonds. For the purposes of analyzing the nonlinear reflection signatures, two types of averaging methods were used, namely incoherent and coherent averaging as follows:

$$U_{\text{incoh}} = \sqrt{\frac{1}{MN} \sum_{m=1}^{M} \sum_{n=1}^{N} A_{mn}^2} \tag{10}$$

$$U_{\text{coh}} = \frac{1}{MN}\left|\sum_{m=1}^{M}\sum_{n=1}^{N} A_{mn}e^{i\theta_{mn}}\right| \tag{11}$$

Incoherent averaging produces the root mean square of the individual pixel magnitudes over the entire frame that is best suited for summing uncorrelated quantities like randomly distributed backscattering grain noise. In contrast, coherent averaging yields the magnitude of the average of complex pixel values over the entire frame that is better suited for summing correlated quantities like reflection from a cluster of scatterers, which are distributed in the same plane and, therefore, exhibit similar phase angles. In reflection mode of operation, this difference can be exploited to suppress essentially incoherent bulk nonlinear scattering from the surrounding host material relative to the partially coherent plane nonlinear scattering from interface imperfections.

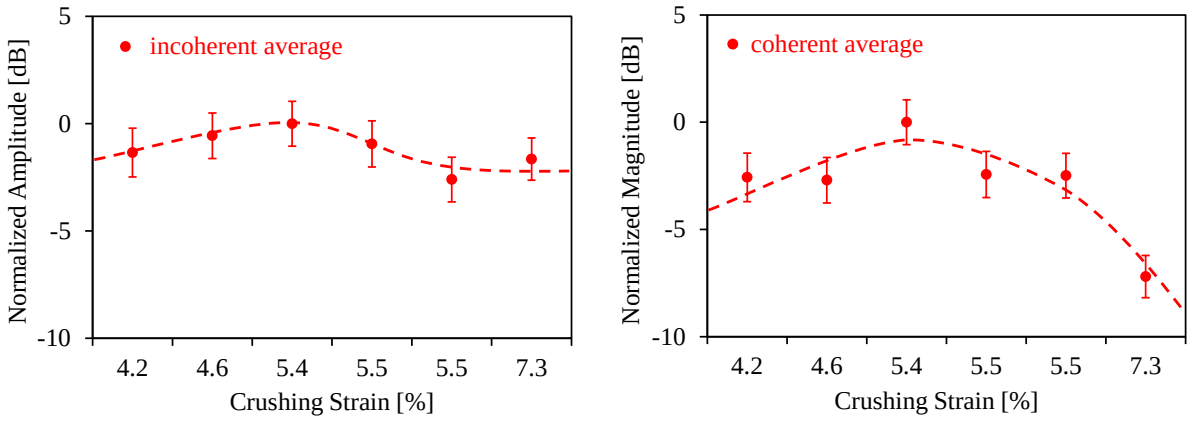

Figure 46. Normalized nonlinear reflection levels obtained with (a) incoherent averaging and (b) coherent averaging from the second batch of high-quality diffusion-bonded Ti-6Al-4Vspecimens versus CS

According to the results shown in figure 46(a), though incoherent averaging yields a perceivable trend among the nonlinear reflection levels of high-quality diffusion bonds, the coefficient of determination is low (i.e., the statistical significance of such regression is low). The main reason for this is not so much the roughly ±1 dB random variation of the nonlinear signature within each nonlinear C-scan, but rather the small total change of the incoherent average from specimen to specimen among high-quality diffusion bonds. In contrast, figure 46(b) indicates that coherent averaging yields much larger variation from specimen to specimen among high-quality diffusion bonds; therefore, the observed trend is statistically more significant and can be exploited for distinguishing the subtle differences that exist among the second batch of high-quality diffusion-bonded Ti-6Al-4V specimens, which all have apparently “perfect” diffusion bonds with no detectible lack of bond. These results show that for high-quality diffusion bonds, coherent averaging works better for assessing bond quality because this averaging method helps to suppress incoherent grain noise coming from the host. The ability to detect the nonlinear grain noise with the redesigned nonlinear inspection system is also apparent in the nonlinear images of the IN718 diffusion-bonded specimen IN13-14 previously shown in figure 43. Because of the high ultrasonic attenuation at 10-MHz inspection frequency, the nonlinear reflection from the

interface was extremely weak and essentially overshadowed by nonlinear grain noise. Still, the similar patterns shown in the two repeated C-scan images indicated that the inspection system actually measured the nonlinear grain noise in the IN718 specimen with possibly some contribution from interface imperfections that could not be positively identified in the absence of a reliable baseline for comparison. These results also indicate that the enhanced nonlinear imaging system is sufficiently sensitive to detect nonlinear grain noise, a new addition to the arsenal of ultrasonic NDE that can be exploited for nonlinear materials characterization as its linear counterpart has been for many years.

8.2 COMPARISON OF LINEAR AND NONLINEAR BOND CHARACTERIZATION

Conventional linear ultrasonic inspection has been proven to be a robust and effective method in detecting imperfections in poor- to medium-quality diffusion-bonded specimens. However, as the bond quality increases, the ability to distinguish different bond qualities by linear inspection quickly drops. Figure 47 shows a simple illustration of the principal difference between the contrasts produced by linear and nonlinear ultrasonic inspections. When the two bonded parts are made of similar material, linear reflection from the interface drops to zero when the fraction of bonded area increases. If the two parts are made of dissimilar materials, the linear reflection will drop to a finite threshold value as the bond quality increases. The reflection threshold is caused by acoustic impedance mismatch between the two materials and weak imperfections will remain hidden below this threshold. In contrast, nonlinear inspection is sensitive to elastic nonlinearity that occurs during opening and closing of the imperfect interface. Therefore, nonlinear inspection can detect very weak imperfections even in relatively well-bonded specimens. Very poorly bonded specimens exhibit very low nonlinearity because the interface imperfections are permanently open; however, in such cases the linear inspection method works sufficiently well for assessing bond quality. In perfectly bonded specimens, the interface nonlinearity is also very low because the two surfaces of the interface are either bonded or compressed so tight that the acoustic vibration amplitudes produced by even the highest available ultrasonic power cannot open the interface.

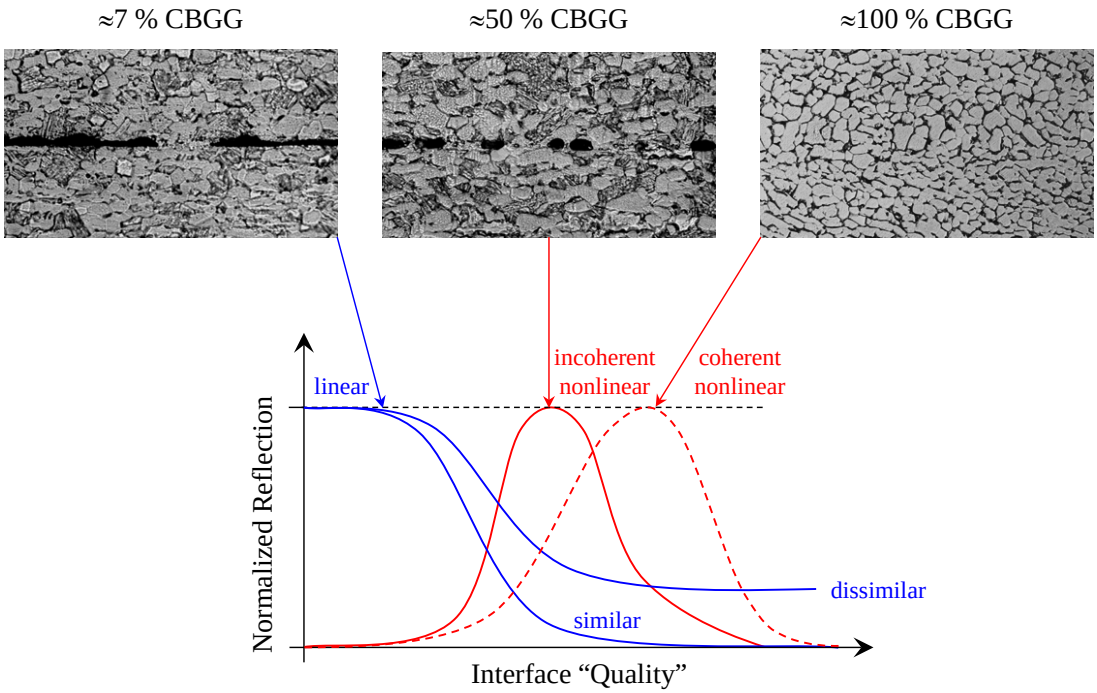

Figure 47. Schematic comparison of linear versus nonlinear bond characterization

Figure 47 shows that neither linear nor nonlinear inspection alone is sufficient to assess a wide range of diffusion-bond quality. However, the nonlinearity of the interface imperfection will reach a peak during the transition from poorly bonded specimens to perfectly bonded specimens, which can be exploited to extend the range of inspection available with linear ultrasonic techniques alone. By combining the two ultrasonic inspection methods, bond characterization can be extended over a substantially increased range of bond quality. For diffusion-bonded specimens with approximately 80 % CBGG value, incoherent averaging of the nonlinear reflection is the better approach for assessing bond quality. However, for high bond quality specimens that exhibit CBGG close to 100 %, coherent averaging appears to be more suitable for bond assessment because it better suppresses the incoherent nonlinear grain noise that might otherwise overshadow the sought nonlinear reflection from weak interface imperfections.

9. CONCLUSIONS

This project had two main goals. The first goal was to redesign the non-collinear ultrasonic shear wave mixing inspection system to increase its sensitivity and selectivity to interface imperfections encountered in diffusion-bonded engine components. The upgraded nonlinear inspection system was integrated into a more robust and compact nondestructive evaluation tool that will be available for engine manufacturers for further studies. The second goal was to test the enhanced capabilities of the nonlinear inspection system on high-quality diffusion-bonded engine alloy specimens. During this phase of the project, the ability of the upgraded inspection system was exploited for quantitative characterization of diffusion-bonded interfaces using nonlinear ultrasonic reflection measurements.

Preliminary analytical and numerical studies provided a better understanding of the non-collinear shear wave mixing technique. Investigation of bulk nonlinear mixing showed that the strength of the mixed longitudinal wave generated by the interacting shear waves is linearly dependent only on the second Murnaghan coefficient. An analytical approximation of the strength of the nonlinear signature detected in the transmission as a function of the interaction angle between the two shear waves was developed and validated by numerical simulation. Two analytical models were developed for studying the nonlinearity of imperfect interfaces between two solids based on shear wave mixing, namely the nonlinear interfacial stiffness model and the nonlinear thin interphase layer model. The results showed that the imperfect interface generates the same amount of nonlinearity in both reflection and transmission.

The shear wave mixing technique was initially used to detect intrinsic bulk nonlinearity of the material. This technique was first adapted for the measurement of interface nonlinearity generated by imperfections in diffusion bonds in transmission mode of operation. In that case, interface imperfections added only little nonlinearity to the relatively high bulk material nonlinearity. Because of the adverse influence of bulk material nonlinearity, the system had to be misaligned from the optimized bulk configuration in hope of suppressing the material nonlinearity in earlier studies. However, this simple technique turned out to be insufficient for the characterization of high-quality diffusion bonds. An analytical study of nonlinear ultrasonic interaction with imperfect interfaces showed that misaligning the system not only suppressed the bulk nonlinearity, it also suppressed the nonlinearity generated by the imperfect interface to almost the same extent. This investigation showed that diffusion-bond quality can be better characterized by detecting the nonlinear reflection from the interface because there is no coherent bulk nonlinearity in the reflection direction. When such bulk nonlinearity occurs in the backward direction due to reflection from interface imperfections, linear techniques are sufficient to use. However, because the nonlinear reflection from the interface is a particularly weak signal, the nonlinear imaging system had to be redesigned, rebuilt, and thoroughly tested and validated.

The project started with a system development phase. The nonlinear imaging system was redesigned to better exploit the non-collinear mixing method for C-scan imaging and quantitative evaluation of hidden interface imperfections in diffusion-bonded parts. In the upgraded inspection system, pulse generation and data acquisition were integrated into one computer. The driving power was increased by more than one order of magnitude, and optimizing the electronic components on the receiving side greatly reduced the electric noise. Integration with pulse generation and data acquisition also increased the digitization rate, imaging resolution, and speed. The mechanical scanning system was significantly improved by introducing an electromechanical alignment system and interleaved scanning. Besides the integration and upgrade of the system's hardware components, a LabVIEW-based software was also developed for electromechanical scanning and alignment; signal generation and reception; data acquisition; signal conditioning; and image processing. In the enhanced system, the alignment procedure of the transmitting transducers was automated, and an optimization program was developed to find the maximum of the nonlinear signature.

In the upgraded inspection system, spurious nonlinearity from various system components, such as amplifiers, transducers, and immersion fluid, was further suppressed. To increase the signal-to-noise ratio (SNR), a novel four-way polarity-flipping technique was developed and

implemented in the system. This signal processing method, which was realized by purely software means in the final version of the inspection system, further increased the SNR by as much as 30–35 dB. These improvements in the hardware and software components made the upgraded nonlinear inspection system uniquely suitable for detecting the weak nonlinear reflection from subtle interface imperfections. Reflection mode of operation made it possible to inspect interfaces with single-sided access, only without the need for back wall reflection. The upgraded image processing software records both the amplitude and the phase-angle distributions of the nonlinear signature so that, in addition to incoherent averaging, coherent averaging can be also used for better suppression of nonlinear grain noise.

After the various upgrades on the nonlinear inspection system were implemented, earlier measurements described by Escobar-Ruiz et al. [8] were repeated using transmission mode of operation for validation purposes. The obtained results indicated that, even in the transmission mode, the new system significantly improved the suppression of spurious bulk nonlinearity from the host material. Next, a new set of very-high quality (cross-boundary grain growth [CBGG] $\approx$ 100 %) diffusion-bonded Ti-6Al-4V specimens manufactured by Vacuum Process Engineering, Inc. were tested to establish the improved detection threshold of the nonlinear inspection system. The nonlinear reflection signal from the interface was successfully located and amplitude and phase-angle C-scan images were obtained and analyzed. These results demonstrated that, in agreement with previous analytical and numerical predictions, detecting the nonlinear reflection from the interface is a better option to characterize high-quality diffusion-bonded interfaces. However, the observed random phase of the reflected signature also indicated that existing nonlinear interface models are insufficient for accurately describing the nonlinear interaction of incident shear waves with high-quality diffusion-bonded interfaces.

It was also found that the anisotropic texture of the first and second batches of Ti-6Al-4V diffusion-bonded specimens was different. The results showed that the new specimens exhibited much higher degree of anisotropy than the old specimens, which perceivably affected the strength of the nonlinear signal measured in two orthogonal directions. Therefore, nonlinear inspection of the new specimens was consistently performed in the same orientation relative to the texture direction. To compare to results from low-texture specimens, measurements in highly textured specimens must be taken and averaged from two orthogonal directions.

Nonlinear inspection conducted in transmission mode of operation with interface configuration was not able to distinguish different bond qualities among diffusion-bonded Ti-6Al-4V specimens of the high-quality second batch. The specimens were then tested in reflection mode of operation. It was found that with coherent averaging, a statistically significant trend exists between the averaged nonlinear reflection signatures and manufacturing process parameters. Because none of these high-quality bonds exhibited less than 100 % CBGG, further quantitative correlation with bond quality or strength could not be established. A set of diffusion-bonded IN718 specimens were also tested to establish the feasibility of nonlinear ultrasonic characterization of diffusion-bonded nickel-base super alloys, but the extreme grain coarsening that inevitably occurred during bonding made nonlinear ultrasonic tests all but impossible. Therefore, a pair of additional diffusion-bonded IN718 specimens were prepared and tested to determine if grain coarsening could be controlled without compromising the quality of the diffusion bond. However, severe grain coarsening put one of the specimens outside the range of

sensitivity of even the upgraded nonlinear inspection system. The other specimen was tested with the enhanced nonlinear inspection system and yielded reproducible nonlinear images, but comparison to other diffusion-bonded IN718 specimens was not possible before the end of the research project.

The tests conducted on diffusion-bonded Ti-6Al-4V specimens showed that the nonlinear reflection from weak interface imperfections can be detected and quantitatively characterized by the enhanced inspection system. By analyzing the nonlinear reflection signature, the results revealed that, for specimens with medium to high bond qualities of approximately 70 % CBGG, incoherent averaging was sufficient to distinguish between different bond qualities, whereas for specimens with very-high bond qualities of approximately 100 % CBGG, coherent averaging helps to suppress the nonlinear grain noise more efficiently and, therefore, appears to be a better option for bond characterization.

10. REFERENCES

1. Ohsumi, M., Kiyotou S., and Sakamoto, M., "The Application of Diffusion Welding to Aircraft Titanium Alloys," *Transactions of the Iron and Steel Institute of Japan*, Vol. 25, 1985, pp. 513–520.

2. Aboudi, J., "Damage in Composites: Modeling of Imperfect Bonding," *Composites Science and Technology*, Vol. 28, 1987, pp. 103–128.

3. Aghdam, M. M., Smith, D. J., and Pavier, M. J., "Finite Element Micromechanical Modeling of Yield and Collapse Behavior of Metal Matrix Composites," *Journal of the Mechanics and Physics of Solids*, Vol. 48, No. 3, March 2000, pp. 499–528.

4. Aghdam, M. M. and Falahatgar, S. R., "Micromechanical Modeling of Interface Damage of Metal Matrix Composites Subjected to Transverse Loading," *Composites Structures*, Vol. 66, No. 1, December 2004, pp. 415–420.

5. Aghdam, M. M., Falahatgar, S. R., and Gorji, M., "Micromechanical Consideration of Interface Damage in Fiber Reinforced Ti-Alloy Under Various Combined Loading Conditions, *Composites Science Technology*, Vol. 68, No. 15, December 2008, pp. 3406–3411.

6. Nagy, P. B., "Ultrasonic Classification of Imperfect Interfaces," *Journal of Nondestructive Evaluation*, Vol. 11, No. 3–4, December 1992, pp. 127–139.

7. Milne, K., Cawley, P., Nagy, P. B., Wright, D. C., and Dunhill, A., "Ultrasonic Non-Destructive Evaluation of Titanium Diffusion Bonds," *Journal of Nondestructive Evaluation*, Vol. 30, No. 4, December 2011, pp. 225–236.

8. Escobar-Ruiz, E., Ruiz, A., Hassan, W., et al., “Non-Linear Ultrasonic NDE of Titanium Diffusion Bonds,” *Journal of Nondestructive Evaluation,* Vol. 33, No. 2, June 2014, pp. 187–195

9. Escobar-Ruiz, E., Wright, D. C., Collison, I., Cawley, P., and Nagy, P. B., “Reflection Phase Measurements for Ultrasonic NDE of Titanium Diffusion Bonds,” *Journal of Nondestructive Evaluation*, Vol. 33, No. 4, December 2014, pp. 535–546.

10. Richardson, J. M., “Harmonic Generation at an Unbonded Interface—I. Planar Interface Between Semi-Infinite Elastic Media,” *International Journal of Engineering Science*, Vol. 17, 1979, pp. 73–85.

11. Barnard, D. J., Dace, G. E., Rehbein, D. K., and Buck, O., “Acoustic Harmonic Generation at Diffusion Bonds,” Journal of Nondestructive Evaluation, Vol. 16, No. 2, June 1997, pp. 77–89.

12. Ohara, Y., Kawashima, K., Yamada, R., and Horio, H., “Evaluation of Amorphous Diffusion Bonding by Nonlinear Ultrasonic Method,” *Review of Progress in Quantitative Nondestructive Evaluation,* Vol. 23, 2004, pp. 944–951.

13. Yamada, R., Kawashima, K., and Murase, M., “Application of Nonlinear Ultrasonic Measurement for Quality Assurance of Diffusion Bonds of Gamma Titanium Aluminum Alloy and Steel,” *Research in Nondestructive Evaluation*, Vol. 17, No. 4, October 2006, pp. 223–239.

14. Ulrich, T. J., Sutin, A. M., Claytor, T., et al., “The Time Reversed Elastic Nonlinearity Diagnostic Applied to Evaluation of Diffusion Bonds,” *Applied Physics Letters*, Vol. 93, No. 151914, October 2008.

15. Jones, G. L. and Kobett, D. R., “Interaction of Elastic Waves in an Isotropic Solid,” *The Journal of the Acoustical Society of America*, Vol. 35, 1963, pp. 5–10.

16. Taylor, L. H. and Rollins, F. R., “Ultrasonic Study of Three-Phonon Interactions. I. Theory,” *Phys. Rev.* Vol. 136, 1964, A591–A596.

17. Childress, J. D. and Hambrick, C. G., “Interactions Between Elastic Waves in an Isotropic Solid,” *Phys. Rev.* Vol. 136, 1964, A411–A418.

18. Korneev, V. A. and Demčenko, A., “Possible Second-Order Nonlinear Interactions of Plane Waves in an Elastic Solid,” *Journal of Acoustical Society of America*, Vol. 135, 2014, pp. 591–598.

19. Zhang, Z., Nagy, P.B., and Hassan, W. (2015). “Numerical study of material nonlinearity assessment based on non-collinear ultrasonic wave mixing,” in *Rev. Progr. QNDE,* 34, AIP Conf. Proc. 1650, pp. 1599–1608.

20. Landau, L. D. and Liftshitz, E. M., *Theory of Elasticity*, Pergamon, Oxford, 1986, “Dislocations,” pp. 122.

21. Murnaghan, F. D. “Finite Deformations of an Elastic Solid,” *American Journal of Mathematics*, Vol. 59, 1937, pp. 235–260.

22. Man, C. S., Koo, L., and Shepard, M. J., “Dispersion of Rayleigh Waves in Titanium Alloy Resulting from Inhomogeneous Residual Stress Induced by Low Plasticity Burnishing,” *Review of Progress in Quantitative Nondestructive Evaluation*, Vol. 21, May 2002, pp. 1651–1658.

23. Yan, P. and Wallach, E. R., “Diffusion-Bonding of TiAl,” *Intermetallics 1*, Vol. 1, No. 2, 1993, pp. 83–97.

24. Hu, W., Ponge, D., and Gottstein, G., “Origin of Grain Boundary Motion During Diffusion Bonding by Hot Pressing,” *Materials Science and Engineering: A*, Vol. 190, No. 1–2, January 1995, pp. 223–229.

25. Huang, Y., Ridley, N., Humphreys, F. J., and Cui, J. Z., “Diffusion Bonding of Superplastic 7075 Aluminum Alloy,” *Materials Science Engineering: A*, Vol. 266, 1999, pp. 295–302.

26. Huang, Y., Cui, J., and Ma, L., “Kinetics of Grain Growth Across Bond Interface During Diffusion Bonding,” *MRS Proceedings*, Vol. 196, 1990, pp. 137–142.

27. Baik, J. M. and Thompson, B. R., “Ultrasonic Scattering from Imperfect Interfaces: A Quasi-Static Model,” *Journal of Nondestructive Evaluation*, Vol. 4, No. 3, December 1984, pp. 177-196.

28. Zhang, Z., Nagy, P. B., and Hassan, W., *Ultrasonics 65*, 2016, pp. 165–176.

APPENDIX A—ANALYTICAL MODELING OF SHEAR WAVE MIXING AT AN IMPERFECT INTERFACE

In a seminal paper on this subject, Baik and Thompson introduced a quasi-static model to study the linear acoustic reflection and transmission from imperfect interfaces [A-1]. According to their linear finite interfacial stiffness model for imperfect interfaces of negligible thickness, both normal σ_{xx} and tangential σ_{xy} stresses are required to be continuous at the interface. The interface imperfection exhibits itself through small normal $\Delta u_x = u_x(0^+) - u_x(0^-)$ and tangential $\Delta u_y = u_y(0^+) - u_y(0^-)$ interface opening displacements that are proportional to the normal and tangential interface tractions:

$$\begin{bmatrix} \sigma_{xx} \\ \sigma_{xy} \end{bmatrix} = \begin{bmatrix} K_n & 0 \\ 0 & K_t \end{bmatrix} \begin{bmatrix} \Delta u_x \\ \Delta u_y \end{bmatrix} \tag{A-1a}$$

or alternatively:

$$\begin{bmatrix} \Delta u_x \\ \Delta u_y \end{bmatrix} = \begin{bmatrix} S_n & 0 \\ 0 & S_t \end{bmatrix} \begin{bmatrix} \sigma_{xx} \\ \sigma_{xy} \end{bmatrix} \tag{A-1b}$$

where K_n and K_t are the normal and tangential interfacial stiffness coefficients, respectively, and S_n and S_t are the corresponding normal and tangential interfacial compliance coefficients. Similarly, the nonlinear finite interfacial stiffness model also requires that the normal σ_{xx} and tangential σ_{xy} stresses be continuous at the interface. The nonlinear interface imperfection exhibits itself through normal Δu_x and tangential Δu_y interface opening displacements that are nonlinear functions of σ_{xx} and σ_{xy} as follows:

$$\begin{bmatrix} \sigma_{xx} \\ \sigma_{xy} \end{bmatrix} = \begin{bmatrix} K_{n1} & 0 & K_{n2} & K_{n3} & K_{n4} \\ 0 & K_{t1} & K_{t2} & K_{t3} & K_{t4} \end{bmatrix} \begin{bmatrix} \Delta u_x \\ \Delta u_y \\ \Delta u_x^2 \\ \Delta u_y^2 \\ \Delta u_x \Delta u_y \end{bmatrix} + \ldots \tag{A-2a}$$

or:

$$\begin{bmatrix} \Delta u_x \\ \Delta u_y \end{bmatrix} = \begin{bmatrix} S_{n1} & 0 & S_{n2} & S_{n3} & S_{n4} \\ 0 & S_{t1} & S_{t2} & S_{t3} & S_{t4} \end{bmatrix} \begin{bmatrix} \sigma_{xx} \\ \sigma_{xy} \\ \sigma_{xx}^2 \\ \sigma_{xy}^2 \\ \sigma_{xx} \sigma_{xy} \end{bmatrix} + \ldots \tag{A-2b}$$

Here, for simplicity, the discussion is limited to quadratic nonlinearity. K_{ni} *and* K_{ti} are linear (i = 1) and nonlinear (i = 2,3,4) normal and tangential interfacial stiffness coefficients. Similarly, S_{ni} and S_{ti} are linear (i = 1) and nonlinear (i = 2,3,4) normal and tangential interfacial compliance coefficients. The stiffness and compliance forms given in equation A-2 are equivalent and can be converted into each other by simple inversion as follows:

$$S_{n1} = \frac{1}{K_{n1}},\ S_{n2} = -\frac{K_{n2}}{K_{n1}^3},\ S_{n3} = -\frac{K_{n3}}{K_{n1}K_{t1}^2},\ S_{t1} = \frac{1}{K_{t1}},\ S_{t4} = -\frac{K_{t4}}{K_{n1}K_{t1}^2} \quad \text{(A-3a)}$$

or:

$$K_{n1} = \frac{1}{S_{n1}},\ K_{n2} = -\frac{S_{n2}}{S_{n1}^3},\ K_{n3} = -\frac{S_{n3}}{S_{n1}S_{t1}^2},\ K_{t1} = \frac{1}{S_{t1}},\ K_{t4} = -\frac{S_{t4}}{S_{n1}S_{t1}^2} \quad \text{(A-3b)}$$

In equation A-2, the linear elements that must vanish for an isotropic interface because of symmetry requirements were replaced with zeros. In addition, assuming that the nonlinear interface exhibits symmetry for tangential deformations of opposite signs, $K_{n4} = K_{t2} = K_{t3} = 0$, and consequently $S_{n4} = S_{t2} = S_{t3} = 0$, will also hold. It should be pointed out that the interfacial spring model is usually presented in the literature as a stiffness relationship. However, the compliance formulation is more straightforward to use in the case under consideration here; therefore, the compliance form given in equation A-2b is used.

The investigation is limited to interface imperfections that cannot be detected using conventional linear reflection or transmission measurements. In such cases, the linear interfacial compliance can be assumed to vanish and the normal σ_{xx} and tangential σ_{xy} stress components at the interface can be approximated by the unperturbed superposition of the shear stresses produced by the two incident waves. Then, the weak perturbation produced by the nonlinear interfacial compliance can be directly calculated from these normal and tangential stress components using equation A-2b. Following the simple rules of stress transformation, pure shear stress of magnitude τ in a coordinate system rotated by an angle θ relative to the *xy* coordinate system produces the following normal and shear stress components:

$$\sigma_{xx} = -\sigma_{yy} = \tau\sin(2\theta) \quad \text{(A-4a)}$$

$$\sigma_{xy} = \tau\cos(2\theta) \quad \text{(A-4b)}$$

Assuming that two shear waves that mix at the interface produce shear stress levels of τ_1 and τ_2 that could be expressed as:

$$\tau_1 = -Z_s\frac{\partial u^{(1)}}{\partial t} \quad \text{(A-5a)}$$

$$\tau_2 = -Z_s\frac{\partial u^{(2)}}{\partial t} \quad \text{(A-5b)}$$

where Z_s denotes the shear wave acoustic impedance of the host material and $u^{(1)}$ and $u^{(2)}$ are the transverse displacements produced by the first and second incident shear waves, respectively. The spatial and temporal variation of these transverse displacements can be expressed as follows:

$$u^{(1)} = U^{(1)} \cos(\mathbf{k}_1 \cdot \mathbf{r} - \omega_1 t) \tag{A-6a}$$

$$u^{(2)} = U^{(2)} \cos(\mathbf{k}_2 \cdot \mathbf{r} - \omega_2 t) \tag{A-6b}$$

where $\mathbf{r}$ denotes the position vector, and $U^{(1)}$ and $U^{(2)}$ are the displacement amplitudes of the first and second incident shear waves, respectively. Both phase terms are neglected for the sake of simplicity. Then, the linearly combined stresses at the interface ($x = 0$) are:

$$\sigma_{xx}^{(l)} = -\omega_1 Z_s U^{(1)} \sin(k_{y1} y - \omega_1 t) \sin(2\theta_1) + \omega_2 Z_s U^{(2)} \sin(k_{y2} y - \omega_2 t) \sin(2\theta_2) \tag{A-7a}$$

$$\sigma_{xy}^{(l)} = -\omega_1 Z_s U^{(1)} \sin(k_{y1} y - \omega_1 t) \cos(2\theta_1) - \omega_2 Z_s U^{(2)} \sin(k_{y2} y - \omega_2 t) \cos(2\theta_2) \tag{A-7b}$$

Assuming that $k_{y1} + k_{y2} = 0$, the nonlinear normal interface opening displacement of angular frequency $\omega_3 = \omega_1 + \omega_2$ is:

$$\Delta u_x^{(3)} = S_{n2} \left(\sigma_{xx}^{(l)} \right)^2 + S_{n3} \left(\sigma_{xy}^{(l)} \right)^2 \tag{A-8}$$

where:

$$\left(\sigma_{xx}^{(l)} \right)^2 = \omega_1 \omega_2 Z_s^2 U^{(1)} U^{(2)} \cos[(\omega_1 + \omega_2)t] \sin(2\theta_1) \sin(2\theta_2) \tag{A-9a}$$

and:

$$\left(\sigma_{xy}^{(l)} \right)^2 = -\omega_1 \omega_2 Z_s^2 U^{(1)} U^{(2)} \cos[(\omega_1 + \omega_2)t] \cos(2\theta_1) \cos(2\theta_2) \tag{A-9b}$$

Here, only one half of the mixed signal of $\omega_3 = \omega_1 + \omega_2$ angular frequency is used for interface characterization, whereas the other half of $\omega_4 = \omega_1 - \omega_2$ angular frequency is disregarded. Because of the symmetric normal interface opening displacement in both directions, the reflected and transmitted mixed longitudinal waves will have the same amplitude:

$$U^{(3)} = \frac{\Delta u_x^{(3)}}{2} \tag{A-10}$$

The longitudinal wave transmission T_3 and reflection R_3 coefficients for the mixed nonlinear signal can be defined as follows:

$$T_3 = -R_3 = \frac{U^{(3)}}{U^{(1)} U^{(2)}} \tag{A-11}$$

Combining equations A-8–A-11 yields the sought reflection and transmission coefficients:

$$T_3 = -R_3 = \frac{1}{2}\omega_1 \omega_2 Z_s^2 \left(S_{n2} \sin 2\theta_1 \sin 2\theta_2 - S_{n3} \cos 2\theta_1 \cos 2\theta_2 \right) \tag{A-12}$$

Another way to model interface imperfections is to use a thin interphase layer. This model assumes that the excess nonlinear compliance of the interface can be accounted for by introducing a homogeneous interphase layer of small thickness, *d,* around the imperfect interface. The third-order (i.e., nonlinear) elastic properties of this otherwise perfectly bonded interphase layer can be obtained by appropriately modifying the corresponding elastic properties of the host material. It can be shown that, to model nonlinear interface imperfections with a thin homogeneous layer of hyperelastic material exhibiting quadratic nonlinearity, the nonlinear interfacial compliances defined in equation A-2b must satisfy not only the previously mentioned symmetry condition ($S_{n4} = 0$) but also a second condition that $S_{n2} = S_{n3}$. In addition, the interphase layer must be very thin relative to both the longitudinal and shear wavelengths. The hyperelastic material will be characterized by its two Lamé constants, λ and μ, three Murnaghan constants, ℓ, *m*, and *n*, and density ρ. To limit the solution to imperfect interfaces that are hidden from linear ultrasonic inspection, it is assumed that the density and linear Lamé constants of the interphase layer are identical to those of the surrounding host material. Out of the three nonlinear Murnaghan coefficients, only the second coefficient, *m,* influences longitudinal wave generation by shear wave mixing. Therefore, the other two Murnaghan constants (ℓ and *n*) of the interphase layer will be also taken to be identical to those of the host material. In this way, the nonlinear interphase layer will be characterized by the product of its thickness, *d,* and the excess value, Δm, of its second Murnaghan coefficient over that of the host material.

The finite interfacial stiffness model assumes a vanishing interface thickness but still produces an interface opening displacement discontinuity. The thin interphase layer model assumes a thickness that is much smaller than the longitudinal and shear wavelengths in it, but also includes some of the neighboring host material within $x = \pm d/2$ distance of the interface on both sides. In general, for a thin, but not vanishingly thin, nonlinear layer, the displacement discontinuities between the opposite faces can be expressed in a form that is similar to equation A-2b, but also includes terms of σ_{yy}*:*

$$\begin{bmatrix}\Delta u_x\\ \Delta u_y\end{bmatrix}^{(layer)} = d\begin{bmatrix}s_{11} & 0 & s_{n2} & s_{n3} & s_{n4} & s_{12} & s_{n5} & s_{n6} & s_{n7}\\ 0 & s_{66} & s_{t2} & s_{t3} & s_{t4} & 0 & s_{t5} & s_{t6} & s_{t7}\end{bmatrix}\begin{bmatrix}\sigma_{xx}\\ \sigma_{xy}\\ \sigma_{xx}^2\\ \sigma_{xy}^2\\ \sigma_{xx}\sigma_{xy}\\ \sigma_{yy}\\ \sigma_{yy}^2\\ \sigma_{yy}\sigma_{xx}\\ \sigma_{yy}\sigma_{xy}\end{bmatrix} + \ldots \quad \text{(A-13)}$$

where s_{11}, s_{12}, and s_{66} are the linear compliance constants of the host material (in Voigt's abbreviated notation). In terms of Lamé constants, these linear compliance coefficients are:

$$s_{11} = \frac{\lambda + 2\mu}{4\mu(\lambda + \mu)} \quad \text{(A-14a)}$$

$$s_{12} = \frac{-\lambda}{4\mu(\lambda + \mu)} \quad \text{(A-14b)}$$

$$s_{66} = \frac{1}{\mu} \quad \text{(A-14c)}$$

In the case of pure shear stresses, equation A-13 can be reduced to the simpler form of equation A-2b by exploiting that $\sigma_{yy} = -\sigma_{xx}$ so that:

$$\begin{bmatrix}\Delta u_x\\ \Delta u_y\end{bmatrix}^{(layer)} = d\begin{bmatrix}s_{11}-s_{12} & 0 & s_{n2}+s_{n5}-s_{n6} & s_{n3} & s_{n4}-s_{n7}\\ 0 & s_{66} & s_{t2}+s_{t5}-s_{t6} & s_{t3} & s_{t4}-s_{t7}\end{bmatrix}\begin{bmatrix}\sigma_{xx}\\ \sigma_{xy}\\ \sigma_{xx}^2\\ \sigma_{xy}^2\\ \sigma_{xx}\sigma_{xy}\end{bmatrix} + \ldots \quad \text{(A-15a)}$$

or:

$$\begin{bmatrix}\Delta u_x\\ \Delta u_y\end{bmatrix}^{(layer)} = \begin{bmatrix}S_{n1} & 0 & S_{n2} & S_{n3} & 0\\ 0 & S_{t1} & 0 & 0 & S_{t4}\end{bmatrix}^{(layer)}\begin{bmatrix}\sigma_{xx}\\ \sigma_{xy}\\ \sigma_{xx}^2\\ \sigma_{xy}^2\\ \sigma_{xx}\sigma_{xy}\end{bmatrix} + \ldots \quad \text{(A-15b)}$$

Again, the elements in the last column of the compliance matrix (i.e., the elements multiplying σ_{xx} σ_{xy}) are zero by virtue of symmetry.

Equation A-15 indicates one of the two reasons why a thin but finite interphase layer is difficult to model in the interfacial compliance approximation. The interfacial compliance model assumes that the interface region has infinitesimally small thickness and produces an interface opening displacement that depends only on the normal and tangential traction components acting on the opposite surfaces of the interface. A thin interphase layer has a small but non-vanishing thickness that causes problems in the adaptation of the interfacial compliance model because it makes it necessary to account for the in-plane normal stress, $\sigma_{yy,}$ that is not a surface traction.

The total compliance of the interphase layer is then the sum of the compliance of the intact layer formed from the host material and the extra compliance of the imperfect interface inside it:

$$\begin{bmatrix} \Delta u_x \\ \Delta u_y \end{bmatrix}^{(\text{layer})} = \begin{bmatrix} \Delta u_x \\ \Delta u_y \end{bmatrix}^{(\text{intact layer})} + \begin{bmatrix} \Delta u_x \\ \Delta u_y \end{bmatrix}^{(\text{interface})} \tag{A-16}$$

Therefore, the non-vanishing effective interfacial compliance coefficients of the imperfect interface can be obtained by subtracting the compliance coefficients of the intact layer of the host material from those of the homogenized interphase layer:

$$S_{n2}^{(\text{interface})} = S_{n2}^{(\text{layer})} - S_{n2}^{(\text{intact layer})} \tag{A-17a}$$

$$S_{n3}^{(\text{interface})} = S_{n3}^{(\text{layer})} - S_{n3}^{(\text{intact layer})} \tag{A-17b}$$

Without the details of deriving the effective interfacial compliances of a homogeneous isotropic interphase layer of quadratic nonlinearity, the final result is that the two non-vanishing normal and tangential nonlinear interfacial compliances are identical and they are proportional to the product of the interphase layer thickness, d, and the excess value, Δm, of its second Murnaghan coefficient over that of the host material that represents the excess nonlinearity caused by the presence of the imperfect interface [28]:

$$S_{n2}^{mat} = S_{n3}^{mat} = -\frac{\Delta m\, d}{2\mu^2\,(\lambda + 2\mu)} \tag{A-18}$$

Here, the superscript "*mat*" indicates that only the material nonlinearity of the thin interphase layer is included in the calculation of the equivalent interfacial stiffness.

REFERENCES

A-1 Baik, J. M. and Thompson, B. R., “Ultrasonic Scattering from Imperfect Interfaces: A Quasi-Static Model,” *Journal of Nondestructive Evaluation*, Vol. 4, No. 3, December 1984, pp. 177-196.